Theory and modeling of the emergence, in rats' brainstem, of a rhythm that drives vibrissae movements

Master Thesis

Author:

Alberto Ferrara

Supervisors:

Prof.ssa Simona Olmi

Prof. Alessandro Torcini

Prof. David Angulo-Garcìa

Università degli studi di Trieste

A.A. 2020-2021

Contents

Introduction **1**

1 Neurophysiology **5**

1.1 Neurons . . . 6
1.2 Neuronal signals and the Action Potential . . . 7
1.3 Synapses . . . 8
1.4 Neural dynamics . . . 10
1.5 Neuronal cell membrane . . . 12
1.6 Ionic channels and ionic currents . . . 14
1.7 Passive electrical properties of the membrane . . . 15
1.8 Spike-Frequency adaptation . . . 17
1.9 Rat physiology: The whisker-mediated touch system . . . 19
1.10 Modeling of whisking rhythmogenesis . . . 22

2 QIF model and Firing Rate equations **25**

2.1 Type I and II neurons . . . 26
2.2 Quadratic Integrate-and-Fire model . . . 28
2.3 Analytical solutions of a QIF neuron . . . 31
2.3.1 Tonic neuron: $\eta > 0$ . . . 32
2.3.2 Excitable neuron: $\eta \leq 0$ . . . 34
2.4 QIF neuron with adaptability . . . 36
2.5 Population model of fully-coupled QIF neurons . . . 38
2.6 Exact macroscopic reduced model for a fully coupled network . . . 41

3 Single population models **48**

3.1 Instantaneous synapses . . . 48

3.2 Exponentially decaying synapses . . . 53

3.3 Adaptation and exponentially decaying synapses . . . 58

4 Two coupled Populations with exponentially decaying synapses **64**

4.1 Two populations reduced model . . . 64

4.2 Identical interacting inhibitory populations . . . 67

4.2.1 Phase plane (η, J_{cross}) . . . 70

4.2.2 Phase plane (J_{self}, J_{cross}) . . . 74

4.2.3 Phase plane (η, J_{self}) . . . 76

4.3 Effects of external current . . . 77

5 Two coupled populations with exponentially decaying synapses and adaptation **89**

5.1 System description . . . 89

5.2 Constant α . . . 92

5.2.1 Case i: (J_{cross}, J_{self}) plane . . . 92

5.2.2 Case ii: (J_{cross}, η) plane . . . 96

5.3 $\alpha - \eta$ parameter plane . . . 103

5.4 Cross-frequency coupling and nested oscillations . . . 108

Conclusions **112**

A Bifurcation theory **115**

A.1 Introduction and basic concepts . . . 115

A.1.1 Super-critical bifurcations . . . 116

A.1.2 Sub-critical bifurcations . . . 118

A.2 Codim 2 bifurcations . . . 119

A.2.1 Neimark-Sacker bifurcation and Floquet multipliers . . . 121

B Symmetry breaking in two identical populations of QIF neurons **126**

B.1 Transverse and Longitudinal symmetry . . . 126

C Numerical methods **130**

C.1 Hilbert transform and instantaneous phase of a signal 130

C.2 Power spectra with Fourier transform 131

Abstract

Questa Tesi di Laurea si colloca nell'ambito degli studi di sistemi complessi realizzati con metodologie proprie della meccanica statistica e dei sistemi nonlineari. Il cervello ed i circuiti neurali, rappresentano un esempio paradigmatico di sistemi complessi, caratterizzato da dinamiche interagenti su scale diverse. In questo contesto abbiamo analizzato dei modelli di circuiti neurali che controllano il movimento delle vibrisse nei ratti.

I sistemi complessi sono dei sistemi composti da molti elementi interagenti, il cui comportamento collettivo non si può ridurre alla semplice somma dei comportamenti individuali. Una tematica attuale di estremo interesse per la fisica teorica e la meccanica statistica, è rappresentata dalla comprensione dei meccanismi che portano all'emergere di dinamiche collettive non banali in reti composte da elementi la cui evoluzione è estremamente semplice, come ad esempio degli oscillatori periodici. In questo ambito negli ultimi anni sono emerse tecniche che permettono di riscrivere in modo esatto nel limite termodinamico la dinamica macroscopica di una rete composta da N oscillatori di fase in termini di poche variabili (due) [54]. Questa tecnica innovativa è stata recentemente estesa a reti neurali ove i singoli neuroni sono rappresentati da modelli semplificati, ma che catturano gli aspetti salienti della dinamica neurale, quali i modelli Quadratic Integrate-and-Fire (QIF)[46]. In particolare, Montbriò, Pazò e Roxin sono stati capaci di riscrivere la dinamica della rete in termini di variabili macroscopiche che hanno una rilevanza biologica per il sistema: il valor medio del potenziale di membrana dei neuroni e la frequenza media di emissione dei potenziali d'azione.

Applicheremo queste innovative tecniche di campo medio per sviluppare un modello realistico per spiegare la generazione di ritmi periodici delle vibrisse dei ratti. In particolare, ci concentreremo sullo studio della dinamica del vIRt (vibrissae intermediate reticular formation) nucleus, un circuito neurale composto prevalentemente da neuroni inibitori, che risulta fondamentale per la generazione del ritmo di oscillazione delle vibrisse [17]. Più specificatamente il circuito vIRT è controllato dal Pre-Bötzinger Complex (preBötC), un circuito neurale deputato alla generazione dei movimenti di inalazione, che tende a sincronizzare i moti delle vibrisse a quelli della respirazione inviando segnali inbitori al vIRt nucleus. A sua volta, il vIRt nucleus innerva i motoneuroni del facial nucleus (FN) che regolano l'attività della muscolatura intrinseca delle vibrisse. Seguendo un modello proposto recentemente da D. Golomb [31], in questa tesi ci poniamo l'obiettivo di modellizzare due popolazioni neurali interne al vIRt. A questo scopo

consideriamo una rete neurale composta da due popolazioni di neuroni con accoppiamento inibitorio e che presentano aspetti biologici rilevanti, quali sinapsi con tempo finito di trasmisisone e adattabilità in frequenza dovuta all'affaticamento dei neuroni [28]. Per far ciò estendiamo modelli di campo medio con adattabilità; sviluppati per una singola popolazione eccitatoria [28]. In una prima parte delle tesi abbiamo analizzato le dinamiche collettive emergenti in questa rete modello del vIRT nucleus al variare dei caratteristici del sistema, mentre successivamente abbiamo tenuto conto dell'effetto di controllo del preBötC nel generare i ritmi delle vibrisse. L'analisi delle dinamiche collettive mostrate da due rete neurali inibitorie con adattabilità e scale di tempo sinaptiche oggetto della Tesi è originale e mai riportata in letteratura. I risultati salienti da noi trovati sono i seguenti. Nonostante le due popolazioni neurali siano identiche abbiamo osservato rotture di simmetrie nella evoluzione macroscopica delle reti in questione sia nel caso di dinamiche asincrone che di oscillazioni collettive. Si osservano inoltre oscillazioni collettive in anti-fase dovute alla adattabilità ove il picco di attivita di una delle due popolazioni corrisponde al momento in cui l'altra popolazione è silente, questo in accordo con l'ipotesi che i due gruppi neuronali presenti nel vIRt sarebbero deputati rispettivamente alla ritrazione e protrazione delle vibrisse. Abbiamo inoltre identificato dei regimi dinamici in cui si manifesta il fenomeno del Cross-Frequency Coupling fra ritmi neurali ed in particolare abbiamo messo in evidenza un accoppiamento tra le frequenze $\theta - \gamma$, osservato in molte parti del cervello e fondamentale per funzioni neurali quali la percezione, la memoria e l'attenzione [7]. Questo lavoro di Tesi è parte di un percorso finalizzato a descrivere un particolare fenomeno biologico, ma le tecniche utilizzate e i modelli studiati sono di interesse generale per la modellizzazione fisica di sistemi complessi a livello di campo medio.

Introduction

The science of complexity represents a new and extremely interdisciplinary research field. Until now, many definitions have been proposed, but none of them has been univocally accepted by the researchers. However, one thing on which the scientists commonly agree is that complex systems are systems made up by many interacting elements whose collective behaviour turns out to be different from the sum of the individual behaviours [50]. At the beginning, the concept of complex systems was associated to the time evolution of systems made up by elements with highly non-linear dynamics. Typical examples of this are given by spatio-temporal chaos or pattern formation in spatially extended systems [26]. In the last decade, the interest of researchers has shifted towards an even more intriguing topic: the emergence of non-trivial collective dynamics in networks composed by elements whose evolution is extremely simple, such as periodic oscillators. Indeed the interaction of these oscillators can give rise to non trivial macroscopic dynamics ranging from periodic, to quasi-periodic and even chaotic ones [52, 53, 44, 49]. A relevant goal for applied mathematics, nonlinear dynamics and statistical mechanics is the understanding of the mechanisms that lead to the emergence of these collective behaviors in complex networks made up of simple units. An interesting example from a physical point of view is represented by networks of phase oscillators, since these models have been used in many biological frameworks in order to explain synchronization processes [66]. In particular, we are interested in exploring the synchronization between neuronal rhythms emerging in several areas of the brain. It goes without saying that network organization of the brain is complex at almost every scale, from small neuronal circuits to large scale networks, where the single neurons represent the fundamental units. In this thesis we will focus on the dynamics of complex neuronal networks, where each individual neuron is modelled as a phase oscillator. In particular we will focus on the so-called Quadratic Integrate-and-Fire (QIF) model, which is widely used in neuroscience due to its simplicity, but at the same time it is able to capture the essential elements of neuronal dynamics

[23]. In particular, networks of QIF neurons have been employed to study working memory and collective coupled oscillations emerging in the auditory cortex [20, 40, 67]. Until now, the analysis of complex neural network has been mainly addressed through numerical simulations, with limitations imposed by computing resources on the maximum number of neurons in the network. As an alternate solution, effective mean field theories for the neuronal dynamics at the level of populations have been proposed: the so-called neural mass models [16]. The neural mass models which reproduce the mean dynamics in terms of macroscopic variables, such as the average activity of the population (the so-called average firing rate) or the average value of neuronal membrane potentials, and the equations that bind these quantities are generally derived in a phenomenological way [73, 72]. Various models based on these principles have been used to find a mathematical description of visual hallucinations, motor perception and even mechanisms for short-term memory [14], and in particular for studying neural oscillations and EEG rhythms [68]. The models that we consider in this thesis belongs to a new generation of neural mass models, where the mean field equations are derived exactly starting from the microscopic evolution equation for the neural population made up by QIF neurons with instantaneous synapses [42]. This innovative approach is based on recent results of statistical physics, which have shown the possibility of deriving exact macroscopic models for coupled phase oscillator networks [54, 55, 63]. These exact reduction techniques are based on the so-called Ott-Antonsen ansatz, published in 2008, which was the starting point for hundreds of new studies of collective dynamics in complex networks [54]. The exact reduction procedure allows us to reproduce the collective evolution of a single population of QIF neurons in terms of two collective variables, which can represent the synchronization level in the population (its phase and amplitude) or, alternatively, the *firing rate* and the mean membrane potential of the neural population. In this thesis we extend the results obtained until now for QIF neural networks, to more realistic synaptic transmission and physiological effects. We therefore include two new synaptic time scales, which are related to finite time post-synaptic transmission (specifically, we assumed exponentially decaying post-synaptic potentials) and frequency adaptation, a phenomenon due to the neuronal fatigue [40]. We study in detail the collective dynamics which emerge from the coupling of two inhibitory neuronal populations with adaptation and exponentially decaying synapses, with the specific purpose to find a model that could explain the generation of the rhythms that drives the whisking activity in rodents. The idea of studying this system to investigate the whisking rhythmogenesis was given by the seminar *theory and modeling of whisking rhythm generation* proposed by Prof. D. Golomb [31]. We have extendend his findings by using the QIF model for the microscopic evo-

lution of single neurons, which allows us to perform the exact reduction in the thermodynamic limit, through the Ott-Antonsen ansatz.

Moreover, we discovered that adaptation with two interacting populations is a mechanism by which Cross-Frequency Coupling (CFC) can occur. CFCs are defined as the phenomenon of interaction between oscillations at different frequency bands, and it is particularly significant in neuroscience [10, 69] because it has been widely observed in human and animal brain (especially in cortical regions) in various tasks such as perception, memory and attention [7]. A link between adaptation and CFC has not been discussed in literature as of now.

In more detail, the thesis has the following structure. The first chapter is devoted to a short introduction to basic concepts on neurophysiology. In particular we give a schematic description of the neuron, of synapses and of the cell membrane structure. Afterwards, we discuss the phenomenology of neural dynamics, characterized by the production of action potentials (also known as *pulses* or *spikes*), in terms of the ionic currents passing through the cell membrane of neurons. Further, we will introduce the concept of *Spike-Frequency Adaptation* (SFA), a common physiological process that we include in our model, and we give a brief overview on the rat Whisker-mediated touch system, together with a circuit model at the end of the chapter.

The second chapter is focused on the description of the QIF model, which, despite its formal simplicity, is able to capture all the main elements of neuronal dynamics. The QIF model is the single neuron model employed for this thesis because it allows for fast numerical integrations and it is amenable of an exact mean-field description, thus being particularly useful for large scale simulations. We report details on the QIF neuron dynamics (with and without adaptation) and we characterize the single neuron transition from quiescent state to tonic emission of spike trains. Furthermore, we show how we can move from a microscopic description of QIF population with instantaneous synapses, corresponding to a system with N degrees of freedom, to an exact neural mass model having only two degrees of freedom by using the Ott-Antonsen ansatz [54]. After this, we will generalize the approach reported in [46] to QIF neural network with exponentially decaying synapses and adaptation.

In the third chapter we report results previously presented in literature. We study in detail the collective dynamics of single population network in the case of instantaneous synapses, exponentially decaying synapses and, finally, both exponentially decaying synapses and adaptation. We use bifurcation theory to define the parameters' range in which the system exhibits interesting behaviour such as collective oscillations, therefore indicating that stable collectively firing regimes are possible and we check whether the adaptation effects are biologically reasonable or

not.

In chapter four and five we present our original results. In chapter four we focus on a system made up by two identical population of inhibitory neurons with exponentially decaying synapses. We extensively study the dynamics of the system with numerical methods (MATCONT and symmetry analysis), discovering peculiar dynamical regimes in which the two populations have a distinct evolution despite being formally identical. Furthermore, we confirm that inhibitory self and cross coupling do not cease collective oscillating behaviours. Afterwards we introduce the effects of the pre-Bötzinger complex [1] through an external inhibitory oscillating forcing. We therefore study the phase locking between the two populations, in order to evaluate the forcing influence on both neuronal populations.

Finally, in the fifth chapter, we move to a network of two identical inhibitory populations with exponentially decaying synapses and adaptation. We see that this system show antiphase oscillations, which could represent a physical situation in which two subpopulations collectively fire in an alternating pattern. We also find various bistability regions, where two different oscillating dynamics can coexist. Finally we show how a model built up in this way is capable of exhibiting $\theta - \gamma$ Cross-Frequency Coupling, an important phenomenon in neuroscience [10, 69]. In the conclusion we will shortly summarize the main results that we obtained during the thesis and we will present ideas for subsequent projects and possible future perspectives. In appendix A we will give a short introduction to bifurcation theory, describing the main bifurcations that we met during the analysis of our system. Appendix B will be devoted to a concise explanation of the ideas underlying transverse and longitudinal symmetry breaking in a system with two identical neuron populations [58]. Finally, in appendix C, we will shortly describe the numerical methods used in order to compute the power spectra and an alternative procedure to compute the phase-locking for a narrow-banded signal, by using the Hilbert transform.

Chapter 1

Neurophysiology

Neurons are highly specialized cells that underlie the function of the Nervous System and are capable of quickly propagating electrical signals over long distances. Pulses generated from neurons upon external stimuli travel along long output poles (called axons) and allow for the transmission of information towards other neurons. In this chapter we introduce some basic concepts related to the neurophysiology of these peculiar cells, starting from their morphology.

Noteworthy components of the neuron are the dendrites, which receive input signals coming from other neurons, and the axon, whose function is the transmission of the output signal to other cells. While the branched out structure of dendrites allows a single cell to receive signals from many other neurons through synaptic connections, the axon can reach distant regions of the brain or even send a signal across the entire spinal column. The signal travels over long distances through an action potential that represents the fundamental element of exchange between neurons. Thanks to the myelinic sheets surrounding the axons, the signal can travel without significant attenuation.

In the next paragraphs we will give a short description of neuron structure and synapses and we will present some details on the cell membrane both at rest and in active conditions, with specific focus on its electrical properties. We will also present an overview on physiological aspects of the neuron and we will study the process that leads to the emission of action potentials, focusing on the dynamics of ionic currents crossing the cell membrane.

1.1. Neurons

Brain information coding occurs through the exchange of electric signals caused by potential differences associated with ionic electric currents that cross the neuronal cell membrane (the most relevant ions are Na^+, K^+, Ca^+ and Cl^-). The number of neurons is extremely high and the connectivity network can bring forth complex topologies, as we can see in Fig. 1.1.1. As an example, in mammals' cerebral cortex one can find densities as high as 10^4 neurons/mm^3. Even though a wide variety of neuronal cells exists (Fig. 1.1.1), we can identify three morphologically and functionally distinct regions: the *cellular body* or *soma*, *dendrites* and *axons*. The cellular body is a compact structure with an approximately spherical shape (its diameter is around 70 μm) whose role is to process information. Dendrites are extensions of the cellular body. They exhibit a strongly branched out structure that can extend for up to one millimeter. Their function is to collect signals coming from other neurons and sending them to the soma afterwards. Axons are long, slender projections of the nerve cells and they can reach over one meter in length (for neuromotors in some kind of animals). They transmit the signal generated in the central region of the cell to the dendrites of another cell. Borrowing the terminology of electronic circuits one can say that dendrites represent the input device, the axons the output device and the soma the center of information processing. The particular morphology of a neuron as well as its location can give us some insight on the specific function executed. As an example, the amount of branching of dendritic structure can tell us how many connections a neuron can establish with other cells.

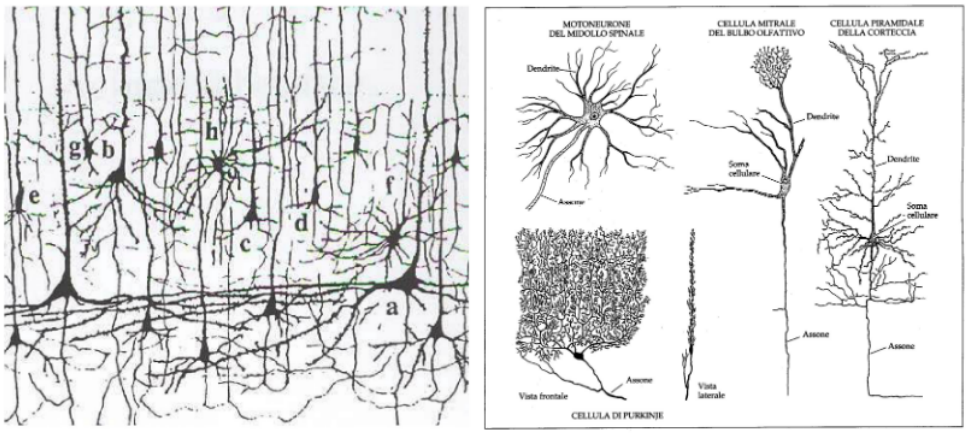

Figure 1.1.1: On the left: neurons from mammals' brain cortex as seen through a microscope. One can see that cell bodies can have triangular and circular shape. The cell labeled as "b" is a classical example of pyramidal cell with triangular body[8]. On the right: various neuron shapes and sizes[36].

1.2. Neuronal signals and the Action Potential

We define as "*membrane potential*" the potential difference measured across two electrodes, respectively located inside the neuronal cell and in the surrounding extracellular fluid. When talking about *neuronal signal* we refer to variations in time and space of the membrane potential. We say that a neuron is *at rest* when it isn't excited by some external input. In such conditions the membrane potential takes a constant value named *resting potential*, typically around -65mV. This means that the inside of the cell has a lower potential with respect to the outside.
Action potentials are pulses of large voltage variation generated during the neuronal dynamics. Their shape is stereotyped and they do not suffer from signal attenuation or distortion along the axon. In Fig. 1.2.1 we show the typical form of an action potential in time.

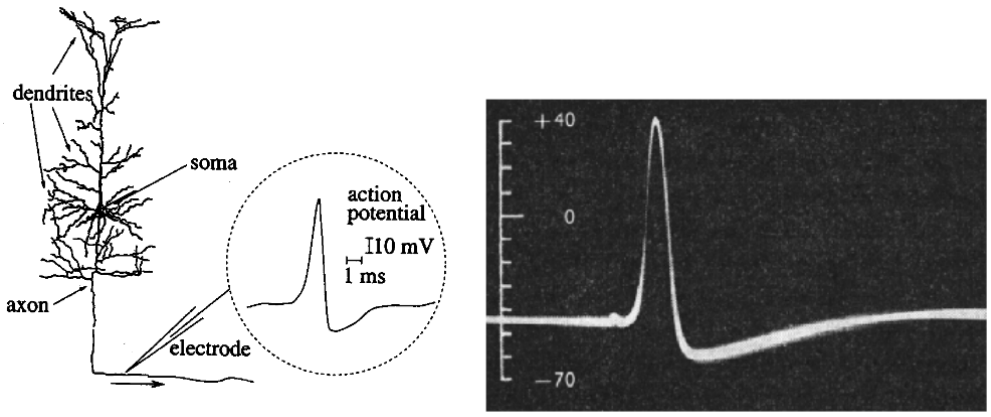

Figure 1.2.1: On the left: typical shape of an *Action potential* [30]. On the right. First measurement of an action potential across a squid giant axon, made by Hodking and Huxley in 1939 [33].

We highlight the following features:

- The voltage pulse lasts around $1 - 2$ ms and its amplitude, as measured between the maximum and the minimum potential values ΔV during this short period of time, are around $100 - 120$ mV
- At the beginning of the pulse we see a phase of rapidly increasing membrane potential that we call *depolarization*, when it reaches a positive value.
- During the decay of the pulse, before reaching its rest value, the membrane potential goes through a phase called *hyperpolarization* significatively slower than depolarization (around 10 ms). In this period the membrane potential is slightly lower than the resting potential.

Once it has been generated inside the neuronal cell, the action potential travels along the axons and the signal is transmitted to other neurons. Information is conveyed through a temporal sequence of action potentials to which we refer to as $spike - train$.

1.3. Synapses

The synapse represents the junction between two neurons, that is the structure through which information is transferred from a brain cell to another. According to such picture, we define as *presynaptic neuron* the cell that transmits the action potential and *postsynaptic neuron* the one that receives the aforementioned signal. We can therefore identify the synapses with the

regions where the axon of the presynaptic neuron interacts with the dendrites of the postsynaptic neuron. Moreover, we introduce the postsynaptic potential (PSP), which is the voltage response of the postsynaptic neuron after the arrival of the action potential coming from the presynaptic neuron.

There exist two different kinds of synapses: Chemical synapses and electrical synapses. Chemical synapses (schematically represented in Fig. 1.3.1), which account for the majority of vertebrates' synapses, work as follows: After reaching the far end of the axon, the action potential generated by the presynaptic neuron locally depolarizes the cell membrane inducing release of peculiar chemical substances called neurotransmitters. These molecules get released by specific biological structures called *synaptic vesicles* into the space located between the presynaptic and the postsynaptic cell, known as the *synaptic cleft*. Once it reaches the postsynaptic dendrites, the neurotransmitter binds to the postsynaptic cell thanks to specialized molecules (*Chemoreceptors*) located on the postsynaptic membrane. These are responsible for opening specific channels through which ionic currents flows from the extracellular fluid to the inside of the cell. The presence of these ions causes a variation of the postsynaptic membrane potential that can be processed by the cell body of the postsynaptic neuron.

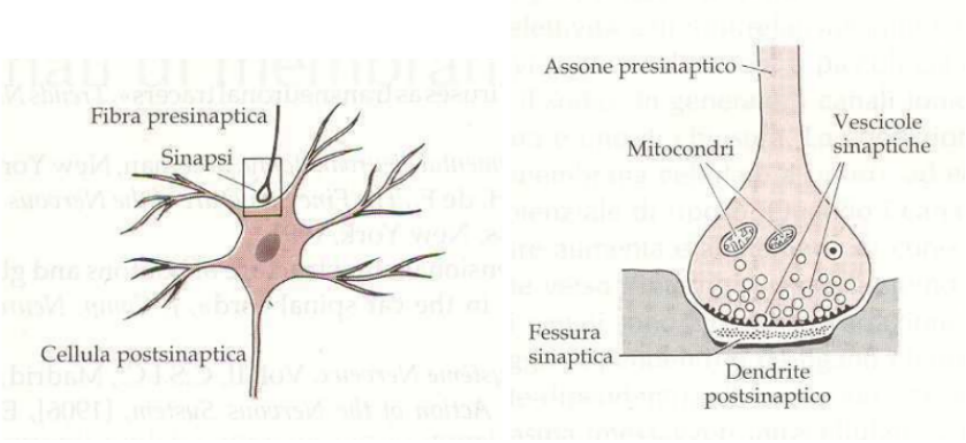

Figure 1.3.1: Typical example of chemical synapse: neurotransmitters are released by the presynaptic axonal terminal as a response to depolarization [51].

Therefore in chemical synapses the electrical signal generates a chemical signal on the presynaptic membrane. This is in turn converted into an electrical signal afterwards. Instead, in electrical synapses the coupling between two neurons occurs through highly specialized ionic

channels (known as $gap - junctions$) which connect pre- and postsynaptic membranes. Hence, electrical synapses allow for a direct current flow between neighbouring neurons. This results in a faster signal transmission.

1.4. Neural dynamics

As we pointed out before, after the action potential, emitted by the presynaptic neuron, reaches the location of the interaction between the two cells, the postsynaptic membrane potential varies. Two distinct behaviours are observable according to the effect of the incoming pulse: the rest potential of the postsynaptic neuron can increase or decrease. We refer to these two possibilities respectively as *excitatory postsynaptic potential* (EPSP) and *inhibitory postsynaptic potential* (IPSP). Analogously we make a distinction between excitatory and inhibitory synapses and between depolarizing and hyperpolarizing stimuli. The amount of synaptic connections is strictly connected to the specific function of the neuron. For instance, cortical neurons are linked to thousands of other neurons from the cortex (from $3 \cdot 10^3$ up to 10^4). Most of the cells are excitatory (85 %) while the rest are inhibitory. As an example, in Fig. 1.4.1 various EPSP amplitudes are depicted, with a mean voltage difference of 0.5 mV.

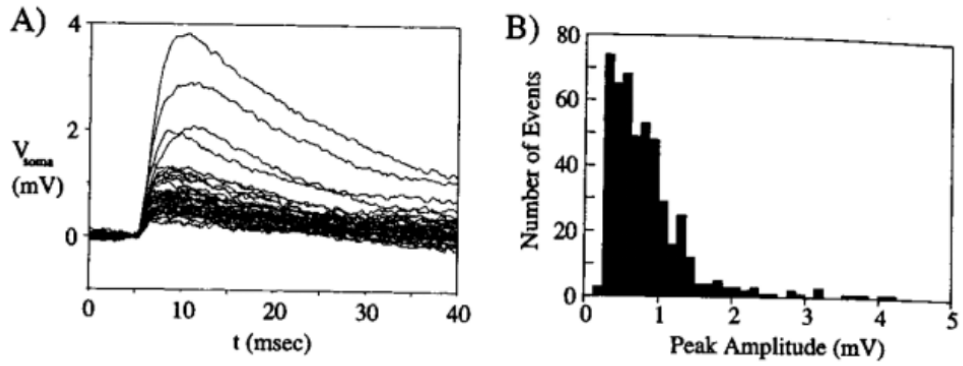

Figure 1.4.1: A) Recording of 478 EPSP from pyramidal cells' soma of rat visual cortex, in presence of spontaneous neuronal activity. B) Peak height histogram of EPSP [62].

In Fig. 1.4.2 we see a schematic representation of the neuronal response dynamics due to the arrival of pulses from presynaptic neurons.

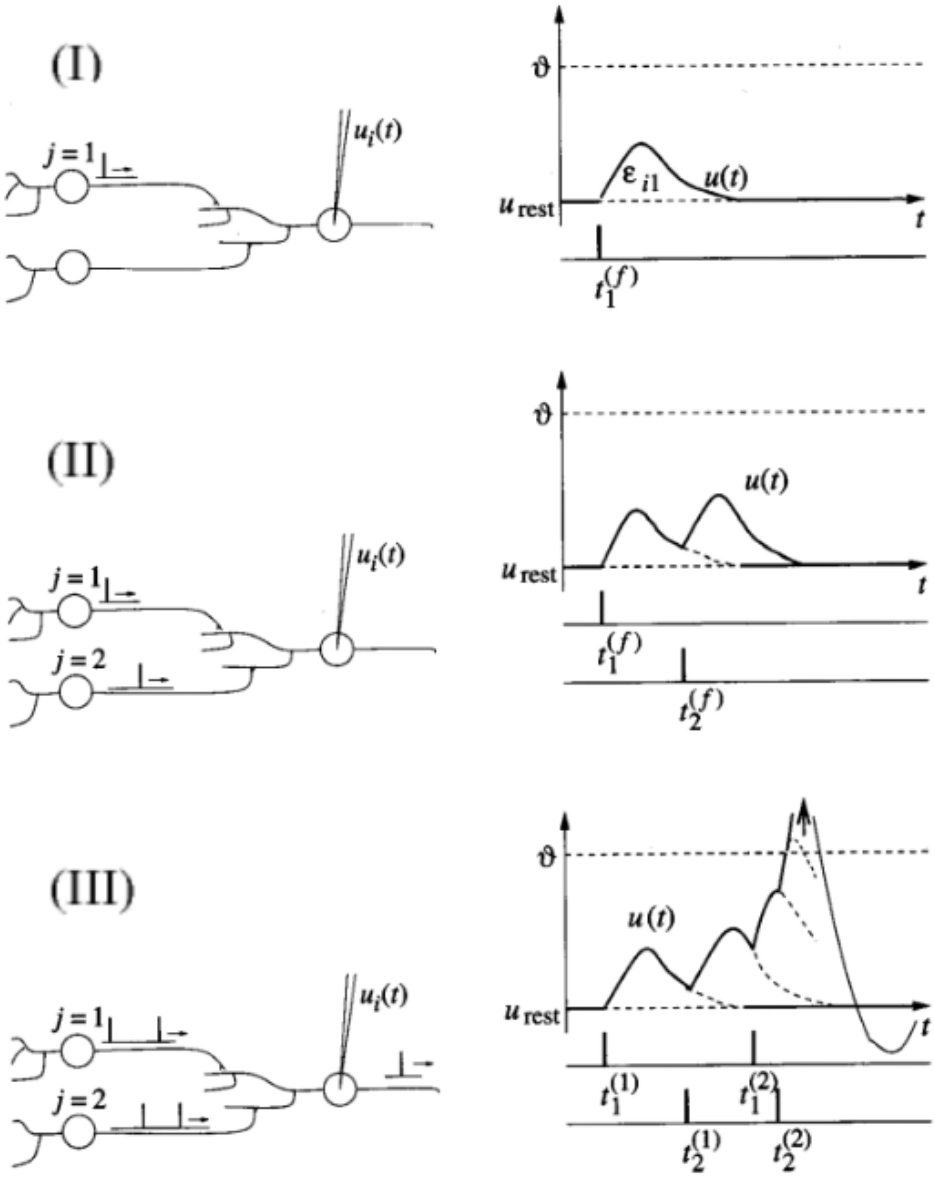

Figure 1.4.2: Schematic representation of neuronal dynamics [29].

(i) A postsynaptic neuron i receives pulses from two distinct presynaptic neurons $j = 1, 2$; $u_i(t)$ and u_{rest} represent the membrane potential and the rest potential of neuron i respectively. We define $\epsilon_{i,j}(t - t_j^{(f)})$ as the postsynaptic potential measured at $t = t_j^{(f)}$, when the signal coming from neuron j reaches neuron i.

(ii) A pulse arriving from the other presynaptic neuron $j = 2$ at $t = t_2^{(f)}$ within an adequately short amount of time, induces a second postsynaptic potential which adds up to the first. In these conditions the postsynaptic neuron has a linear response to incoming inputs.

(iii) When $u_i(t)$ exceeds a typical value θ, known as *Activation threshold*, the neuron's behaviour becomes highly non-linear. The resulting action potential has a stereotyped shape with no specific dependence on the pulses it was caused by. For the entire duration of the action potential, the neuron goes through a refractory period during which stimuli coming from other neurons do not cause a significant response.

There is a distinction between Absolute and Relative refractoriness. The first one is a short period of time (of around 2 ms) corresponding to the rise of the action potential during which a new action potential cannot be generated. The latter is the subsequent stage of hyperpolarization of the neuron during which there is a chance for the neuron to be once again excited, even though it may prove quite hard to do so. Therefore the refractory period gives us an inferior bound on the minimum time period between two distinct spikes.

1.5. Neuronal cell membrane

The cell membrane of a neuron (Fig. 1.5.1) is made up by specific biomolecules, mainly lipids and proteins. The inside of the cell is separated by extracellular fluid through a lipid bilayer which is around 6 nm thick. Some particular proteic molecules are embedded in this lipidic structure and they usually cross the entire thickness of the membrane, thus connecting the inside with the outside of the cell. These molecules have a wide variety of names such as *membrane channels* or *ionic channels*.

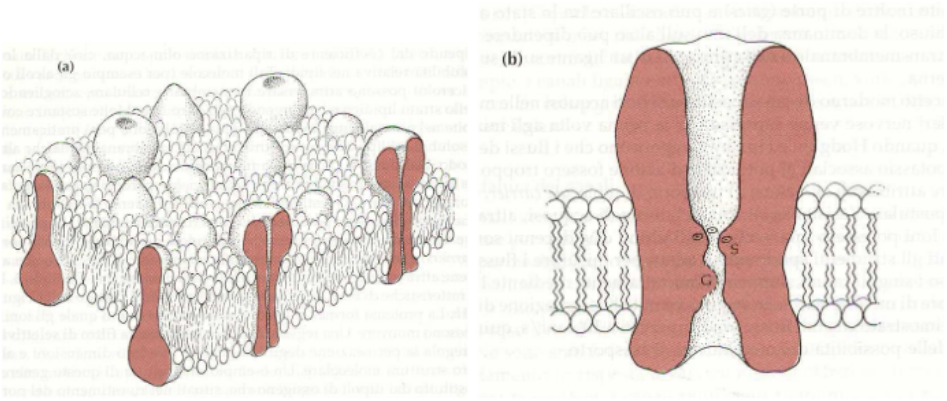

Figure 1.5.1: a) Neuron cell membrane structure; b) Ionic channel structure [51].

The cell membrane can be crossed by substances in both directions through different mechanisms. Some kind of biomolecules (alcohol and glycerol) cross the membrane by dissolving in the lipid bilayer and re-emerging from the other side. In such situations the penetration can be less or more difficult according to their level of solubility in lipids. As we said before, inorganic ions (sodium, potassium, calcium and chlorine) make up the ionic currents responsible for the neuronal electric activity. These ions move through the membrane by hooking up to specific molecules, called *transport molecules*, capable of driving them through the proteic channels. These channels are the main ionic transport system employed during the action potential generation, as the ion fluxes involved (around 10^6 ions/s) overcome the handling transport molecules. One can identify the following elements inside of the structure of proteic channels:

- A central tunnel filled up with an aqueous solution.
- A region of this tunnel acting as a selective filter that handles the access of ions according to their physical and chemical features.
- A gating system, which stochastically opens and closes, allowing the channel to oscillate between "closed" and "open" states. Most gates are closed when the membrane potential is at its resting value, but that's not a general rule as some gates are actually needed for maintaining the membrane potential at a constant value.

1.6. Ionic channels and ionic currents

Ionic channels are said to be *activated* or *deactivated* respectively when the channel is in an open or closed state. Since we are talking about a stochastic process, those two states correspond to high or low probability of finding the gate open or closed instead of a continuous and constant condition (see Fig. 1.6.1). There is a wide variety of activation (i.e. opening) mechanisms of a channel. We define "voltage activated channels" those channels whose states can be adjusted to a specific value of the membrane potential. For instance, voltage-dependant sodium channels belong to this class and they have a key role on the membrane depolarization that leads to the rise of action potentials.

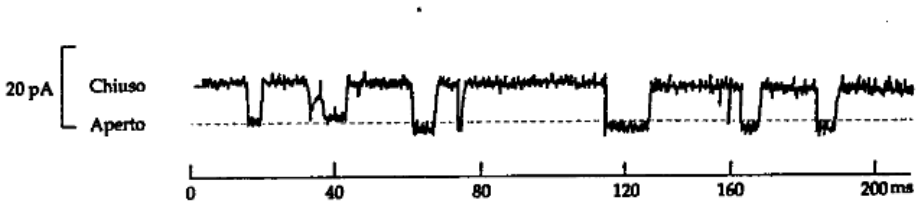

Figure 1.6.1: Example of channel current. Such current is made up by a sequence of approximately square pulses whose emission is related to the state of the channels [15].

As far as ionic selectivity is concerned, we make a distinction between Cationic and Anionic channels whether they are permeable to positive or negative ions. Permeability to a ionic species (denoted as p) is an instrinsic property of the membrane which tells us how easily the ions pass through the membrane itself. We define it through the following empirical relation [39]:

$$J = -p\Delta[C], \tag{1.6.0.1}$$

Where J is the molar flux (measured as mol/$(cm^2 \cdot s)$ and $\Delta[C]$ represents the difference in ionic concentration on both sides of the membrane (measured as mol/cm^3). p has the physical dimension of speed and it is usually given in cm/s. Membrane permeability therefore depends only on the type of ionic channels and how many of them are there. The channels can, however, be more or less specialized for a single ionic species. Chlorine channels amount for most of the anionic channels and that's not a surprise since Cl^- is the most common anion that we can find in biological solutions.

Conductance gives us a measure of the ability of a membrane to transport electrical current and is usually measured in *Siemens*, with $1S = 1\Omega^{-1}$. Since current is transported by ions, conductance of a membrane won't depend only on the membrane's properties (i.e. its permeability) but on the concentration of the ionic species inside and outside as well (which represents the number of free charge carriers). However it's not easy to find a general mathematical relation between permeability and conductance since such dependence changes according to how the ion travels across the channel. In general the current passing through an ionic channel depends on [51, 37]:

- The conductance of the channel
- The concentration gradient between inside and outside of the cell. This tends to produce a flux of ions directed towards the region where the concentration is lower according to an empirical law attributed to *Fick* [37]:

$$J_{diff} = -D\frac{d[C]}{dx}, \tag{1.6.0.2}$$

  where J_{diff} is the flux due to diffusion (measured in ions/$(cm^2 \cdot s)$), D represents the diffusion coefficient (measured in cm^2/s) and [C] is the ionic concentration.
- The difference in electrical potential across the membrane.

1.7. Passive electrical properties of the membrane

From the point of view of electrical circuitry, one can build up a simple representation of a section of the membrane at rest condition with a resistence (R_m), a capacity (C_m) and a voltage source V with the same voltage as the rest potential. (see Fig. 1.7.1 and Fig. 1.7.2) This is legitimate as the nerve membrane response to current changes in rest condition does not significatively deviate from that of simple electronic components, whose behaviour is well known both theoretically and empirically. A resistence needs to be included in this picture because of the ionic channels that connect inside and outside of the cell. In order to describe this property we usually define a *specific membrane resistence* r_m, which is the resistence per unit of the membrane surface area. (r_m varies between $10^3\ \Omega \cdot cm^2$ and $5 \cdot 10^4\ \Omega \cdot cm^2$). This depends on the number of ionic channels on the membrane. In addition to that, charges can stack up on both surfaces. This has the effect to generate the membrane resting potential, from which we define a *specific membrane capacitance* c_m, a capacitance per unit area, typically around $1\mu\text{F/cm}^2$.

One can then easily exploit the general capacitance definition $q_m = c_m V$ to find the charge per unit area on the membrane, since we know both the rest potential ($-65mV$) and the specific membrane capacitance. We get that $q_m \approx 6.51 \cdot 10^{-8}$ C/cm^2, which means that the mean value of ions on a square centimeter of nerve fiber in rest conditions is around $4 \cdot 10^{11}$. Despite these useful results, we cannot apply this circuitry picture for non-linear or active neuron behaviour (such as voltage-dependant conductance).

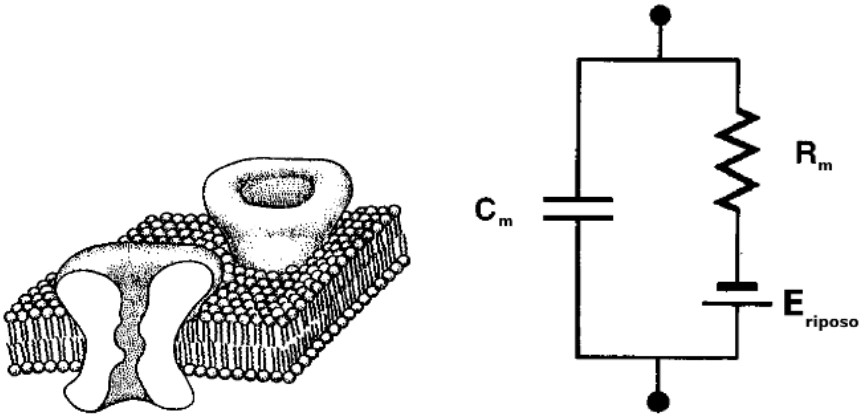

Figure 1.7.1: Electrical representation of a region of the neuron cell membrane. E_{riposo} is the resting potential [39].

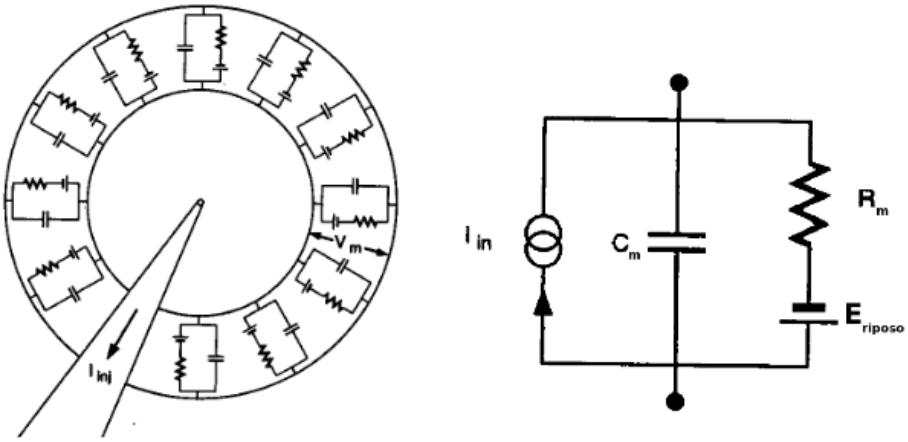

Figure 1.7.2: Equivalent circuit of the entire cell membrane. R_m and C_m respectively stand for the parallel equivalent of all the resistances and the capacitances. E_{riposo} is the rest potential while I_{in} represents a generic external current [39].

1.8. Spike-Frequency adaptation

We have explained how an action potential is generated and how information is carried through a sequence of repeated action potential known as *spike train*. We now want to introduce a widespread phenomenon, exhibited by various kind of neurons both in vertebrates and invertrebrates, called $spike - frequency\ adaptation$. This term covers a variety of physiological mechanisms by which the output frequency of spike trains in a neuron decreases upon a continuous input stimulus (see Fig. 1.8.1 for an example). This means that the period between the emission of two different action potentials does not depend only on the input stimulus itself, but on other physiological processes as well.

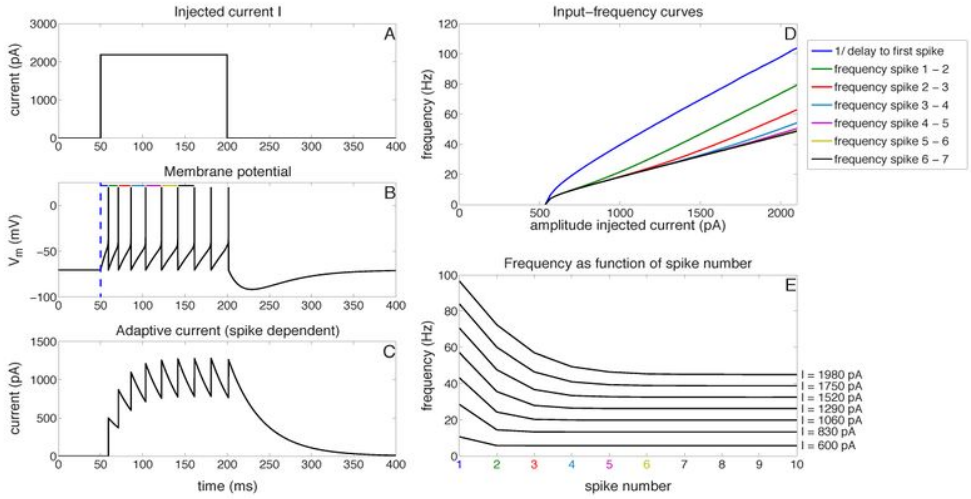

Figure 1.8.1: Simulation of an integrate-and-fire neuron with a simple spike-dependent adaptation mechanism. When stimulated with a square pulse (A), the neuron fires with a frequency that reduces over time (B, E), due to a hyperpolarizing current (C). This can be quantified by looking at the inter-spike interval (coloured lines in B) or frequency (D) as a function of the spike number (D and E).[32]

Most mechanisms leading to Spike-frequency adaptation involve some form of slow negative feedback affecting the excitability of the cell. For instance:

- Ionic channels responsible for action potential generation go through a period of inactivation after which they need to recover, which may take some time. This has the effect that after a spike, less ionic channels are available for generating a new action potential. This leads to a longer period between two consecutive spikes (lower frequency).
- An action potential can be generated even below the spike threshold by specific currents that are activated upon depolarization (e.g. potassium currents)

Spike-frequency adaptation can have noticeable effect on the spiking behaviour of the neuron, having thus various dynamical and functional consequences. In Chapter 3 and Chapter 4 we will explore the effects of this physiological process on the dynamics of systems made up by interacting neurons.

1.9. Rat physiology: The whisker-mediated touch system

In this section we explore the rodent whisker-mediated touch system as it will be the main object of study and modeling of this thesis. The whisker-mediated touch system is a structurally well-established and organized model system which gives rise to complex behaviours despite its structural simplicity.

From a functional point of view, rodents rely on their whisker-mediated touch system to collect information about their surrounding environment (localizing and tracking objects) through a rhythmic orofacial motor activity known as whisking. In particular, whisking is a rhythmic cyclic vibrissae sweeping action, consisting of repetitive forward (protraction) and backward (retraction) movement.

Figure 1.9.1: On the left: black and white snapshot of rat whisking during exploration. (a): front view, (b): vertical view. [Recorded in 2007 by the Active Touch Laboratory at Sheffield (ATL@S)]. One the right: close-up picture of rat snouts and whiskers.

Rat vibrissae, or whiskers, form a grid layout on both sides of the rat snout on the mystacial pad Fig. 1.9.1. The peculiar feature of the vibrissae is that they contain dense nerve terminals and sensory receptors. Vibrissae have the role of mechanical transducers, thus they mediate the transferring of the touch signal into the sensory receptors. In general, vibrissae are classified according to their physical shape and according to the morphologies and distributions of nerve terminals and receptors around the vibrissa shaft. Due to this physiological traits vibrissae can have various different functional roles and different sensitivity to a variety of tactile stimuli,

making them a behaviourally efficient system.

It's important to underline that the receptors are sensible to various whisking dynamical parameters such as amplitude, frequency and duration of vibrissae oscillating cycles and that all these receptors exhibit adaptation processes at different levels.

Whisking cycles have an average frequency of around 8 Hz [70] and usually a synchronization between whisking respiration and other orofacial movements is observed, suggesting some kind of coordination between these muscle groups. We can see two different pattern of whisking, known as exploratory whisking (with a frequency range of 1 to 5 Hz) which usually lasts for 1 to 10 seconds, and a small-amplitude high-frequency pattern (ranging from 15 to 25 Hz) for a period of 0.5 to 1 second.

Movements of vibrissae and follicles are controlled by facial motor nerves. On the basis of anatomical observations [21], it has been concluded that mystacial pad muscles move the whiskers forward (protraction), whereas backward motion (retraction) is a result of both the elastic properties of the facial tissue and of an active muscular control [4].

Whisking is controlled by a neuronal oscillator located in the vibrissa-related region of intermediate reticular formation of the medulla (vIRt). This region includes facial premotor neurons and another kind of neurons with a spiking activity which is either in phase or in anti-phase with whisking protraction. After various anatomical experiments [17], it's been suggested that rhythmic whisking is driven by inhibitory neuronal processes. Furthermore, the rhythms of muscles that protract individual whisker and move the mystacial pad are phase-locked during rapid rhythmic breathing cycles known as *sniffing*. An important contribution to this rhythm formation is given by pre-Bötzinger complex (pre-BötC), the inspiratory oscillator for respiration. Pre-BötC has unidirectional inhibitory connections to the vIRt, thus suggesting its role in the phase locking and in the mystacial pad control.

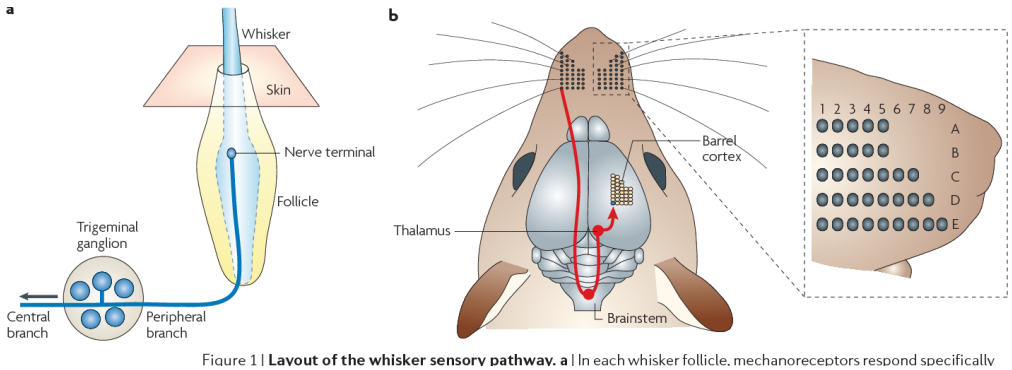

Figure 1 | **Layout of the whisker sensory pathway. a** | In each whisker follicle, mechanoreceptors respond specifically

Figure 1.9.2: Layout of the whisker sensory pathway. On the left side we see the follicle containing nerve termination of the trigeminal ganglion, thus enabling high sensibility to whisking movements. on the right we see the path from whiskers to the barrel cortex area, the somatotopical representation area of the vibrissae in the somatosensory cortex [19]

Trigeminal ganglion (also called semilunar ganglion) shown in Fig. 1.9.2 consists of the cell bodies of pseudo-unipolar neurons with their proximal axons innervating the ipsilateral brainstem trigeminal complex (BTC) and their distal axons which innervate the vibrissae follices. As we said before, different trigeminal units have various tuning properties, being sensible to amplitude, frequency, duration and direction of whisker motion. This is functionally relevant as trigeminal ganglions have the fundamental role of transmitting information coming from the outside (through vibrissae interaction with the environment) to other regions of the nervous system.

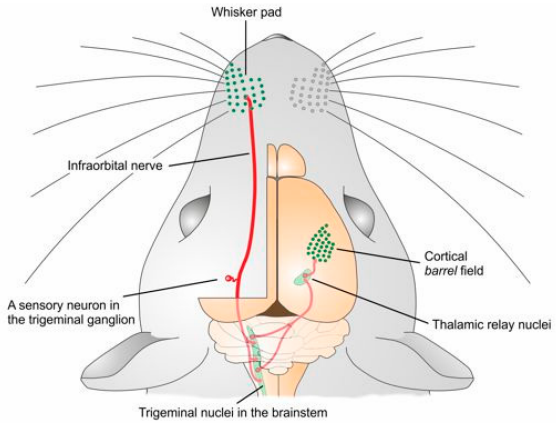

Figure 1.9.3: More detailed layout of the whisker pathway, from the mystacial pad to the cortical barrel area, passing trough trigeminal ganglions and thalamic neuron nuclei [25]

The Brainstem trigeminal complex that we mentioned above is divided into the principal sensory nucleus (PrV) and the spinal nucleus (SpV). The nuclei of trigeminal neurons receive inputs from trigeminal ganglion cells and form aggregated neuron clusters called barrellettes, which have the interesting feature to preserve the somatotopic organization of the whiskers on the mystacial pad. Furthermore, we underline the fact that adaptation is a commonly observed physiological effects among BTC units, with various time-scale for the adaptive process. Many second order-neurons of brainstem trigeminal complex send information to thalamic units such as the posterior thalamic nucleus (POm) or the intralaminar thalamic nuclei, as shown in Fig. 1.9.3, where subsequent information processing occurs. A detailed description of the entire process of information transmission from sensorial stimuli to neurons of the brain cortex and from neurons to behaviour is out of the scope of this thesis. However, we have given a short overview of important physiological and physical details of the whisking rhythm generation (in particular information on inhibition, adaptation and interaction between different phase oscillators) which will be our guiding light in subsequent modelling of this process.

1.10. Modeling of whisking rhythmogenesis

As we anticipated in the introduction, the goal of this thesis is to define the mechanism underlying whisking rhythm generation and explain how the whisking rhythm is shaped by the breathing rhythm.

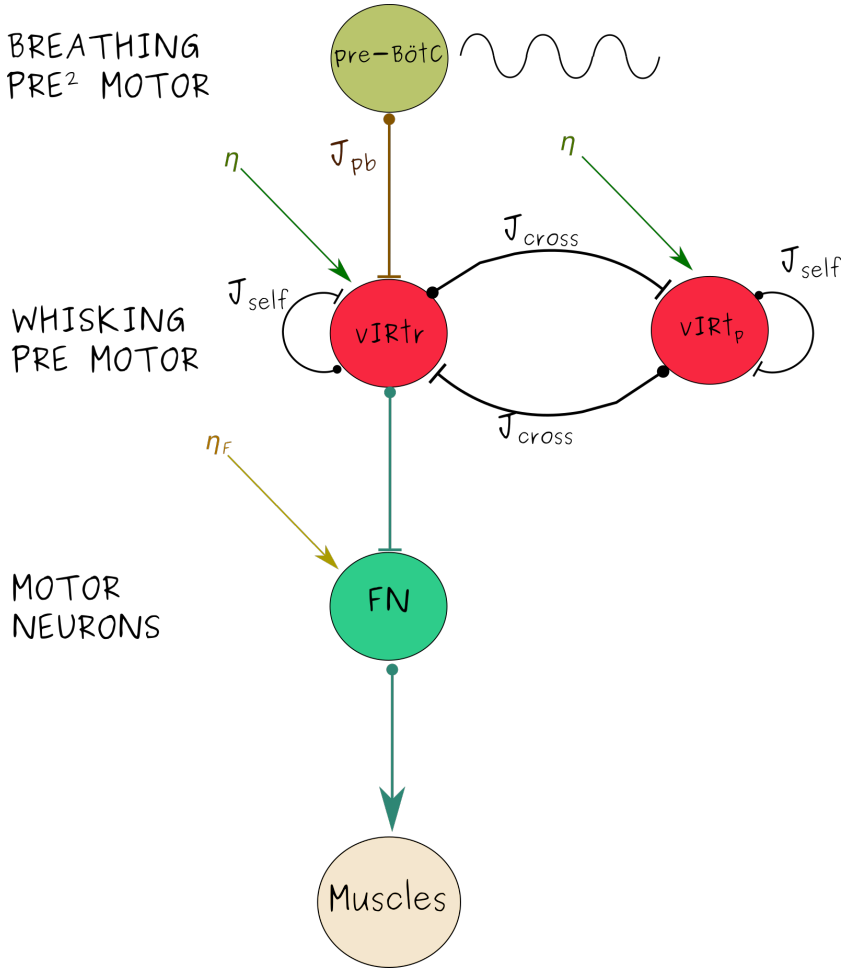

Figure 1.10.1: Circuit model of the whisking rhythmogenesis system. The two vIRt sub-populations respectively are active during retraction ($vIRt_r$) and during protraction ($vIRt_p$). Pre-BötC affects the vIRt sub-population associated with retraction with an inhibitory coupling [17]. J_{self} represents the self-interaction of the vIRT sub-populations, while J_{cross} is the mutual interaction between them. J_{PB} is the strength of the inhibition of Pre-BötC on $vIRt_r$. η is a parameter which takes into account both the internal excitability of the network and the average value of the external current and is identical for both populations. FN represent the Facial Nucleus neurons, which are the Motor neurons associated with whisking.

As we seen before, there are evidences for the vIRT role in whisking rhythmogenesis.

1. Spiking of neurons in the vIRt is tightly locked to whisking (the vIRt neurons are pre motor neurons, meaning that they are active during whisking). In addition to that, chemical or

genetic lesions of the vIRt abolish whisking.

2. Furthermore, chemical activation of the vIRt induces whisking in anesthetized rats.

For these reasons, we can assume that the vIRt is necessary for rhythmogenesis and a regular pattern can be obtained even without the Pre-BötC input. Therefore, we will focus on both cases, with and without the forcing coming from the Pre-BötC.

There are also evidences [17] [47] [57] showing that:

- Pre-BötC regulation on vIRt is inhibitory
- There exist two sub-populations of neurons: vIRt_r and vIRt_p;
- vIRt neurons are mostly inhibitory (Hence the inhibitory self- and cross-coupling between the two populations);
- Synaptic connections from vIRt to the Facial Nucleus are inhibitory

With these ideas in mind, we construct a model of the whisking rhythmogenesis circuit shown in Fig. 1.10.1 and proposed by D.Golomb [31]. We use the QIF model for the single neuron dynamics and we apply a recently developed macroscopic model [46] used to reduce the microscopic dynamics to a simpler macroscopic description which could allow us to propose a mechanism for rhythm generation in rats whisking.

Chapter 2

QIF model and Firing Rate equations

We have seen that neurons, of various types and morphologies, are connected in very complex networks through chemical and electrical synapses. As with many other physical systems, the complexity of the brain is such that one cannot simply study the brain or a portion of it with a direct approach by taking into account every possible physical and biological variable affecting the evolution of the system.

This is due to theoretical reasons as an extremely detailed description would increase the number of parameters involved that need to be calibrated, thus making the state of the network very sensible to small variations of the parameters (fine-tuning problem). Moreover, computational problems may also show up because simulation of extremely complex networks becomes excessively expensive in terms of calculations and machine power.

The practical consequence of such problem is that we need to find a description level that allows us to capture the fundamental properties of a system while neglecting non-essential processes. Since we are interested in studying collective phenomena of neural networks, it's reasonable to use a simplified model of the neuron at a microscopic level and then look for macroscopic effects emerging from the interaction between a great number of simplified single neurons.

In neuroscience, *formal spiking neuronal models* are commonly used to perform theoretical analysis and computational simulations of large scale networks [43]. We will try to justify this particular choice.

In formal spiking models we do not specifically want to reproduce the shape of the membrane

potential in time. We assume that a neuron fires a pulse towards every neuron which it is connected to when the membrane potential reaches a fixed value.
In this chapter we will introduce a specific *formal spiking* model known as the *Quadratic Integrate-and-fire* (QIF) *model* as it will be the main starting point for studying the neural populations we are interested in. We will provide a detailed study of its dynamics and we will move on to an exact neural mass macroscopic model which allows us to describe a complex infinite network with a low number of differential equations.

2.1. Type I and II neurons

Even though we can find a wide variety of neurons with different dynamics, we can still classify neurons into two general classes according to the response of the neuronal cells upon stimulation by a constant current [34, 45]:

- ***Type I:*** Action potentials can be emitted with arbitrarily small frequency, based on the intensity of the applied current.
- ***Type II:*** Action potential can only be emitted with a frequency above a certain value. The resulting frequency weakly depends on the intensity of the applied current.

Experimental data comparing the two types of neurons are shown in Fig. 2.1.1. In the left column of Fig. 2.1.1, we can see data related to a pyramidal neuron of layer 5 of the primary visual cortex of the rat, which represents a type I neuron, while in the right column, as an example of type II neurons, we find data related to a midbrain neuron of the rat. Usually, type I neurons fire with a frequency that varies continuously, ranging from 2 Hz to 100 Hz, occasionally reaching even higher values. In contrast, type II neurons' frequency range is shorter and, more importantly, the transition from quiescent state to the tonic state of periodic emission of action potential occurs through a discontinuous jump.

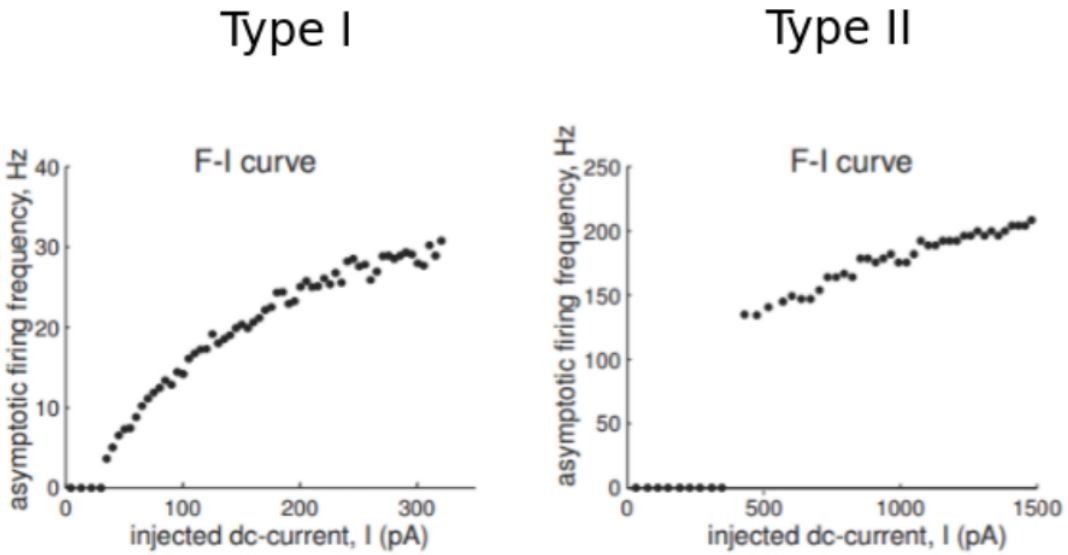

Figure 2.1.1: Comparison between a type I and a type II neurons belonging to a rat brain. Figure taken from [45] and adapted.

These biological differences are at the basis of the main criteria by which we classify single-neuron mathematical models. In general, for conductance-based models, as explained by Ermentrout and Rinzel [59], the transition from silent state to periodic oscillations typically occurs through two different kinds of bifurcation corresponding to the two types of neurons (see appendix for more information). For type II neurons, the transition occurs through a super-critical Hopf bifurcation while for type I neurons it takes place through a $Saddle - Node\, on\, invariant\, circle$ bifurcation (known ad SNIC). In the following we focus on type I neurons, thus we now present a short description of the SNIC bifurcation.

Given a dynamical system living in a phase space Γ and defined through d first-order differential equations, a SNIC bifurcation can only take place in a space with two or more dimensions, as shown in Fig. 2.1.2

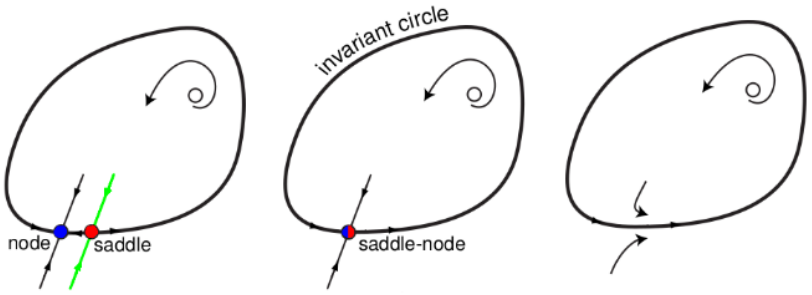

Figure 2.1.2: Illustration of the SNIC bifurcation. Figure taken from [45]

Before the bifurcation occurs, one can find three distinct equilibrium points: a stable node (blue dot), an unstable saddle point (red dot), and an unstable focus (white dot). The unstable manifold of the saddle point is formed by two heteroclinic trajectories emerging from the saddle point which tend to reach the stable node after infinite time. These two trajectories form a closed curve in the phase space that contains the unstable focus. The stable variety of the saddle point represents the "threshold-manifold". This means that given any initial condition on the left of this point, the trajectory in the phase space will be attracted to this stable point, while an initial condition to the right will be dragged around the entire loop before converging towards the stable node.

Through this peculiar behaviour we are able to define the *excitable state* of the neuron. According to this picture, the path followed by the trajectory around the repulsive focus corresponds to the mechanism of action potential generation, while the short path can describe relaxation of the neuron towards the resting state. It's interesting to observe what happens at the exact bifurcation value: the node and the saddle completely merge together so that the heteroclinic orbit becomes a homoclinic orbit (i.e. an infinite loop). The dynamical behaviour of such system is independent on the dimensionality of the system.

2.2. Quadratic Integrate-and-Fire model

In this section we will define the (QIF) model. It will be the single neuron model we are going to use to study the dynamical behaviour of neural networks. The QIF model is a prototype of type I neuron, since it reproduces its peculiar transition from quiescent state to periodic oscillations.

Ermentrout and Kopell [23] have shown how to describe the behaviour of a system undergoing a SNIC bifurcation via a single ordinary differential equation, when the bifurcation parameter is close to its critical value:

$$\dot{\theta}(t) = [1 - \cos\theta] + [1 + \cos\theta]I(t) \tag{2.2.0.1}$$

This form is particularly useful because a SNIC bifurcation can occur in an arbitrarily high-dimensional system; However, the dynamically relevant behaviour on an invariant cycle is uni-dimensional thus making subsequent calculations much easier. Moreover, this equation is independant from any other specific detail of the system.

Through Eq. (2.2.0.1) we define the so-called $\theta - model$. θ is the main dynamical coordinate which is related to membrane potential, while $I(t)$ is a time varying parameter which stands for a current being applied to the neuron. Both are non-dimensional real numbers.

In this representation neurons are seen as simple phase-oscillators described with an angular coordinate. Since $\theta(t)$ only appears as a cosine argument, we can easily represent our system on the $(\theta,\ \dot{\theta})$ two-dimensional plane, with $\theta \in [0, 2\pi]$. For simplicity, we take a constant and not too large I. This allows us to consider three qualitatively distinct cases according to the sign of I, as seen in Fig. 2.2.1. Since $\dot{\theta} = 0$ corresponds to the fixed points of the system, for $I > 0$ we have an unstable equilibrium solution (θ_{inst}) near $\theta = 0$ and a stable solution (θ_{stab}) near $\theta = 2\pi$. As discussed before, initial conditions such that $\theta_0 > \theta_{inst}$ will lead us across all the circumference until we reach the stable equilibrium point. The rate of change of θ will have its maximum at $\theta = \pi$. Conversely, having $\theta_0 < \theta_{inst}$ will slowly bring the trajectory to the stable solution moving on the opposite direction. Since θ represents a neuron's membrane potential, we can interpret θ_{stab} as the resting potential. θ_{inst} has the important role of fixing the threshold value at which the action potential generation is triggered. In the formal spiking picture, we assume that the neuron fires at a time $t = t_{fire}$ such that $\theta(t_{fire}) = \pi$. We stress that in this model, firing is an entirely formal event which we arbitrarily define with the latter condition.

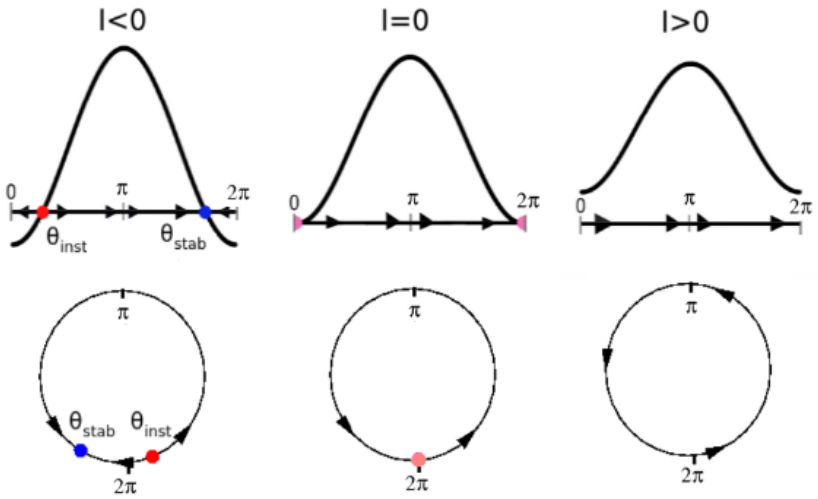

Figure 2.2.1: SNIC of the $\theta-model$. The three figures above show the curve in Eq. (2.2.0.1) for different values of I and its intersections with the horizontal axis $\dot{\theta}=0$ Figure taken from [22] and readjusted.

In Fig. 2.2.1 the three typical phases of the saddle node bifurcation are shown. For $I<0$ we see coexistence of stable and unstable equilibrium. These two distinct points merge when $I=0$, disappearing for any positive value of I.

When $I>0$ the system keeps moving along the cycle, firing a train of periodic pulses. In order to compute the frequency of such oscillating system, we can assume $\theta_0=0$ as initial condition. Defining T as the time needed to move through the entire loop, one has that $\theta(T)=2\pi$. T can be expressed through the following integral relation:

$$T=\int_0^{2\pi}\frac{d\theta}{\cos\theta(t)+[\cos\theta(t)]I(t)} \tag{2.2.0.2}$$

Such integral can be exactly solved using the following transformation:

$$V=\tan\frac{\theta}{2} \tag{2.2.0.3}$$

This transformation maps the angular variable $\theta\in[0,2\pi]$ in $V\in[-\infty,+\infty]$, thus changing the integration boundaries accordingly. From this we obtain:

$$\dot{V}(t)=V^2(t)+I \tag{2.2.0.4}$$

Solving the integral leaves us with the following expression for the period:

$$T = \frac{1}{\sqrt{I}} \left[\arctan \frac{V}{\sqrt{I}} \right] = \frac{\pi}{\sqrt{I}} \tag{2.2.0.5}$$

Therefore in the $\Theta - model$ we observe an oscillating regime $\forall I > 0$ whose frequency increases with the square root of the external current. It's interesting to compare this simple analytical expression with an empirical frequency-current relation for type I neurons. As shown in Fig. 2.1.1, the experimental behaviour is well reproduced, adding further value to the $\theta - model$ [45].

This model is often called QIF model because of the quadratic term which turns out after the transformation made in Eq. (2.2.0.4). Expressed in this coordinate system, the QIF model provides a natural interpretation in terms of membrane potential of the neuron. We will now explain this in further details.

Some solutions of Eq. (2.2.0.4) reach an infinite value in a finite time. From a mathematical point of view, this is a geometric consequence of the coordinate transformation as seen through a local point of view. Despite this, the equation is equivalent to Eq. (2.2.0.1), thus describing the behaviour of a generic dynamical system near a SNIC bifurcation. To capture the essence of the formal spiking picture, which occurs when the SNIC bifurcation takes place on an invariant cycle, we include a peculiar boundary condition in the form of a reset rule: whenever the membrane potential V reaches a threshold value V_{th}, the potential is reset to a specific V_{reset} value such that $V_{reset} < V_{th}$. In the following we set $V_{th} = +\infty$ and $V_{reset} = -\infty$, so that the $\theta - model$ and $QIF - model$ are equivalent.

In the following section we will analytically compute the explicit solutions for $V(t)$ at different values of the external current. Due to the presence of the SNIC bifurcation, the three different dynamical behaviours need to be treated separately as they will result in different solutions.

2.3. Analytical solutions of a QIF neuron

The system we are going to study is defined by the following equation:

$$\dot{V}(t) = V^2(t) + \eta. \tag{2.3.0.1}$$

Note that we have renamed I with η for later convenience and we will stick to this notation from now on. The behaviour of $\dot{V}$ at different V for fixed I is shown in the phase plane $(V, \dot{V})$ in Fig. 2.3.1.

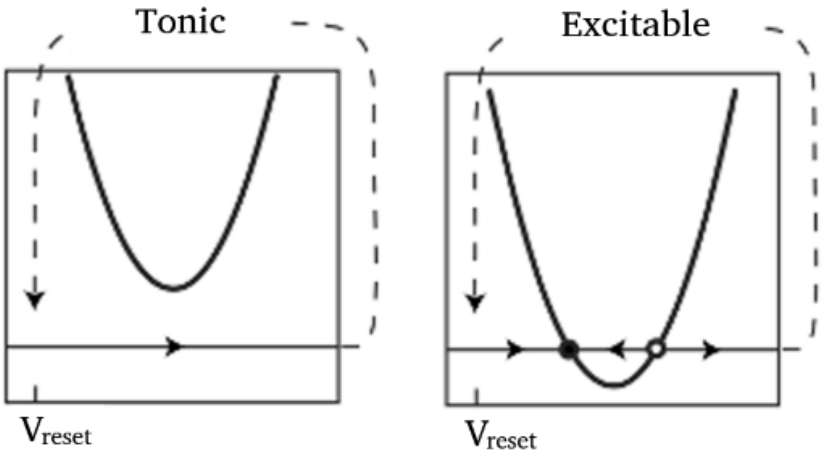

Figure 2.3.1: Phase plan $(V, \dot{V})$ of the QIF model. On the left $\eta > 0$, on the right $\eta < 0$. Figure taken from [45].

2.3.1. Tonic neuron: $\eta > 0$

When $\eta > 0$ we have that $\dot{V} > 0, \forall t$. Thus, given an initial condition $(t_0, V(t_0))$ we can obtain a solution for $t > t_0$ by solving the following integral:

$$\int_{t_0}^{t} \frac{\dot{V}}{V^2(t) + \eta} dt = \int_{t_0}^{t} dt \tag{2.3.1.1}$$

This leaves us with the following solution:

$$V(t) = \sqrt{\eta} \tan\left(\sqrt{\eta}(t - t_0) + \arctan \frac{V(t_0)}{\sqrt{\eta}}\right) \tag{2.3.1.2}$$

A plot of this solution is shown in Fig. 2.3.2.

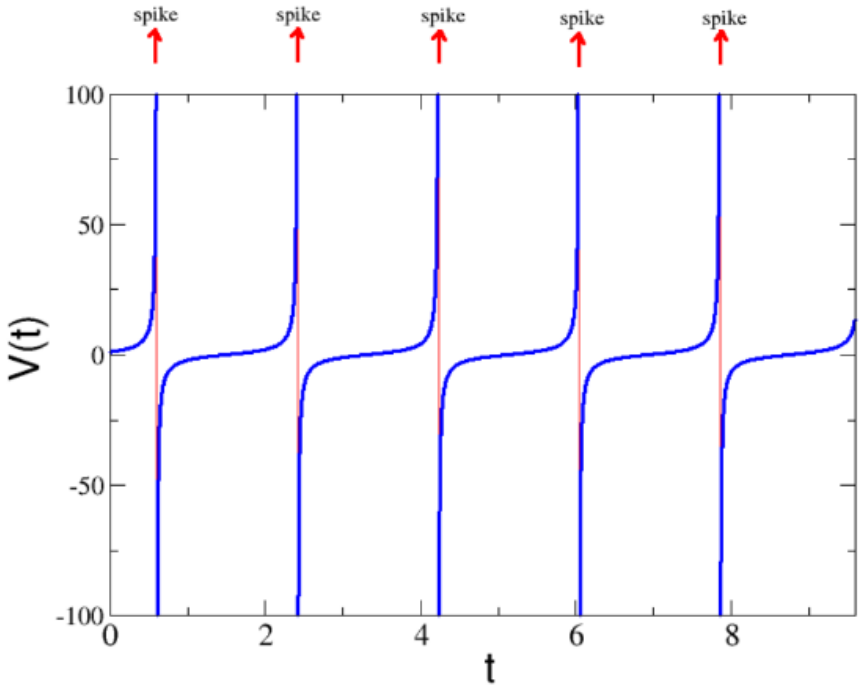

Figure 2.3.2: Dynamics of a tonic neuron. In red, the vertical asymptotes represent the firing times t_{fire} in which the neuron emits an action potential. Function graph of Eq. (2.3.1.2)

This expression makes sense as long as the argument of the tangent is less than $\frac{\pi}{2}$ since the function is not continuous for such value. By making use of the reset rule we can analitically extend the solution of Eq. (2.3.0.1) up to the time t_{fire} such that the argument of the tangent is exactly $\frac{\pi}{2}$. t_{fire} is given by:

$$t_{fire} = t_0 + \frac{1}{\sqrt{\eta}} \left(\frac{\pi}{2} + \arctan \frac{V(t_0)}{\sqrt{\eta}} \right) \tag{2.3.1.3}$$

We assume that the neuron spikes at this precise moment, after which the value of its membrane potential is instantly reset to V_{reset}:

- $\mathrm{V}(t^-_{fire}) = + \infty \longrightarrow$ Emission of the action potential;
- $\mathrm{V}(t^+_{fire}) = - \infty \longrightarrow$ Reset of membrane potential.

According to this rule, the subsequent dynamical behaviour will be determined by the following initial condition: $t_0 = t^+_{fire}$. We can now repeat the same procedure as before and integrate for a time interval equal to $\frac{\pi}{\sqrt{\eta}}$ until a new singularity is encountered, thus marking the emission of

a new action potential. We can conclude that a QIF neuron with $\eta > 0$ periodically fires a pulse at times t_{fires} expressed as:

$$t_{fire} = \frac{1}{\sqrt{\eta}} \left(\frac{\pi}{2} + \arctan \frac{V(t_0)}{\sqrt{\eta}} \right) \pm k \frac{\pi}{\sqrt{\eta}} \quad k \in \mathbb{Z} \tag{2.3.1.4}$$

Once again, the frequency ν is proportional to the square root of the injected current:

$$\nu = \frac{\sqrt{\eta}}{\pi} \tag{2.3.1.5}$$

2.3.2. Excitable neuron: $\eta \leq 0$

When $\eta \leq 0$ we proceed by separation of variables obtaining once again Eq. (2.3.1.1). However, with a negative current there exist specific times at which $V(t) = V_{stab}$ or $V(t) = V_{instab}$ because the time derivative of the membrane potential vanishes. Therefore, we choose our initial condition and integral boundaries such that the interval (t_0, t_1) does not include such constant solutions. With this, we can proceed to study two distinct cases.

Sub-threshold dynamics: $|V(t_0)| \leq \sqrt{\eta}$.

In this case $V(t_0)$ is such that $\dot{V}$ is negative, so the solution $V(t)$ will be strictly monotonically decreasing and will tend asymptotically towards the resting membrane potential value V_{reset}. Solving the integral and keeping in mind that $V(t_0) > V(t)$, we obtain:

$$V(t) = -\sqrt{|\eta|} \tanh \left(\sqrt{|\eta|}(t - t_0) + \operatorname{arctanh} \frac{V(t_0)}{\sqrt{|\eta|}} \right) \tag{2.3.2.1}$$

The solution is plotted in Fig. 2.3.3

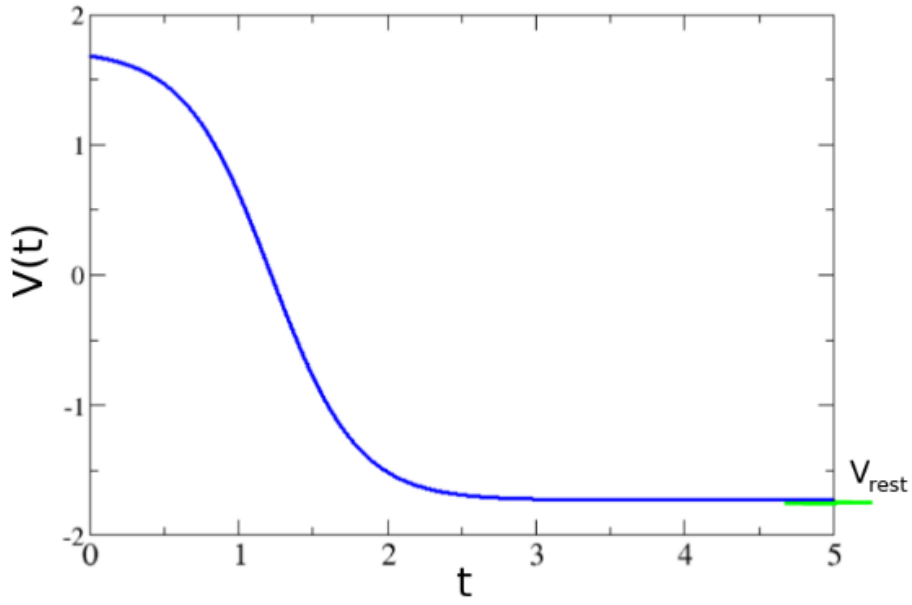

Figure 2.3.3: Dynamics of an excitable neuron, sub-threshold dynamics. Trend of $V(t)$ in Eq. (2.3.2.1). In green, the value of the resting membrane potential $V_{rest} = -\sqrt{\eta}$.

We interpret this solution as a neuron that won't emit any action potential.

Supra-threshold dynamics: $|V(t_0)| > \sqrt{\eta}$:

We assume that $|V(t_0)| > \sqrt{\eta}$, $V(t_0)$ lies in the right half of the positive values of the parabola shown in Fig. 2.3.1. Starting once again from the integral, one can show that there exists a finite time t_f such that $V(t_f) = +\infty$ expressed as:

$$t_f = t_0 + \frac{1}{\sqrt{\eta}} \operatorname{arctanh} \frac{\sqrt{\eta}}{V(t_0)} \tag{2.3.2.2}$$

This means that, given the chosen initial conditions, the neuron will emit a single action potential and then the membrane potential will be reset to $-\infty$. Since this value is obviously lower than $\sqrt{|\eta|}$, an isolated neuron won't be able to emit a second action potential. The analytical solution in this case, shown in Fig. 2.3.4, is:

$$V(t) = -\sqrt{|\eta|} \operatorname{cotanh} \left(\sqrt{|\eta|}(t - t_0) - \operatorname{arctanh} \frac{V(t_0)}{\sqrt{|\eta|}} \right) \tag{2.3.2.3}$$

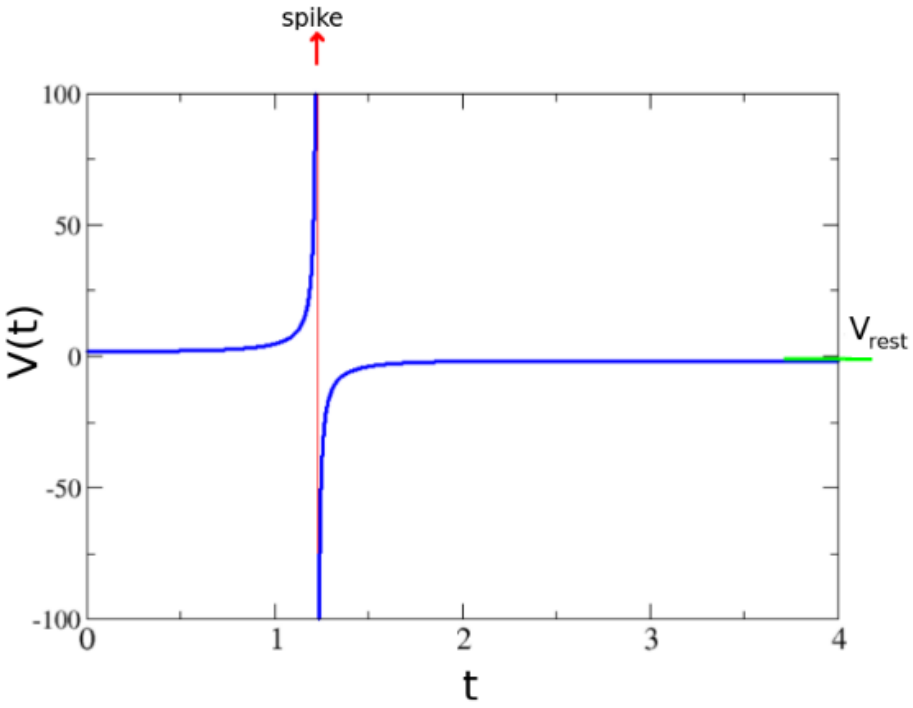

Figure 2.3.4: Dynamics of a supra-threshold neuron. In red, the vertical asymptotes represent the firing time t_{fire} in which the neuron emits a single action potential before the membrane potential tends to V_{rest}. Function graph of Eq. (2.3.2.3)

2.4. QIF neuron with adaptability

We have seen that the QIF model is capable of reproducing the properties of a type I neuron with an appropriate reset rule and an initial condition. However there are many other physiological processes which affect the resulting neuronal dynamics. As we discussed in previous paragraphs, Section 1.10, we want to include the effects of adaptation by introducing a new variable through the addition of a second equation that, together with Eq. (2.3.0.1), describes the dynamics of a type I neuron with adaptation. Such system can be defined through the following system of

differential equations:

$$\begin{aligned} \dot{V} &= V^2 + \eta - A \\ \dot{A} &= \frac{\alpha - V}{\tau(V)} \end{aligned} \tag{2.4.0.1}$$

Along with the reset rule, which takes the following form:

$$\begin{aligned} V(t^+_{fire}) &= V_{reset} \quad if\ V(t^-_{fire}) = V_{th} \\ A(t^+_{fire}) &= k' A(t^-_{fire}) + k'' \quad if\ V(t^-_{fire}) = V_{th} \end{aligned} \tag{2.4.0.2}$$

The first equation is similar to Eq. (2.3.0.1) with a new additive term which tends to reduce the derivative of the membrane potential, thus increasing the time needed to reach V_{th}. We have introduced a new parameter α which defines the strength of the adaptation coupling to the membrane potential. Furthermore, adaptation is described by a variable characteristic time $\tau(V)$ which depends on the voltage value $V(t)$. In the following we assume $\tau(V) = \tau/V$ as it is found to be a good approximation to the observed behaviour: for large value of the membrane potential, the integration time of adaptation is progressively shorter and viceversa.
We then obtain:

$$\dot{A} = \frac{V(\alpha - V)}{\tau} \tag{2.4.0.3}$$

From a dynamical point of view, after the neuron fires according to our formal spiking picture, the membrane potential is immediately reset to V_{rest} while the adaptability A is multiplied by a constant k' and increased by an amount k'', thus allowing for cumulative adaptive effects in case of a spike train. A time evolution simulation is shown in Fig. 2.4.1 in a regular spiking regime.

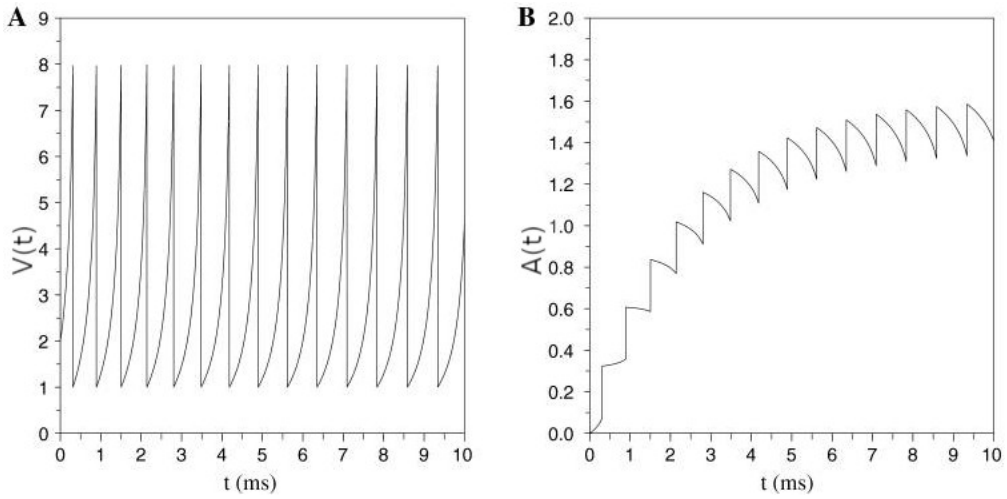

Figure 2.4.1: Time evolution of the membrane potential (A) and the adaptive variable (B) in a regular spiking regime. Chosen parameters are: $\eta = 2, \tau = 15, \alpha = 1, V_{rest} = 1, V_{th} = 8$ Figure taken from [74] and adapted

2.5. Population model of fully-coupled QIF neurons

In this section we will discuss the fully coupled network model of QIF neurons with instantaneous synapses. This means a physical system made up by N neurons where each component interacts instantaneously and with all the other neurons. In order to define a neural network we need to describe the coupling between single QIF neurons. We report a recently developed macroscopic model [54] [46] used for reducing, under certain hypotheses, the detailed microscopic dynamics described by a huge number of differential equations to a few equations for a macroscopic description of the system.

A neural network is a graph whose nodes are made up of neurons and whose connections are represented by synaptic processes of interaction between them. The coupling is described through synaptic weights [39], which can be fixed or can change over time (this phenomenon is known as synaptic plasticity and it depends on past conditions of both interacting neurons [38]. In the following, we will assume that the synaptic weights remains unchanged over time.)
The evolution equation for each node (neuron) in a neural network of N QIF neurons has the following form:

$$\dot{V}_i(t) = V_i^2(t) + \eta_i + JS(t) + I_e(t), \quad i = 1, ..., N. \tag{2.5.0.1}$$

We can interpret the terms of Eq. (2.5.0.1) as follows:

- The *excitability* η_i of the i-th QIF neuron is a constant parameter which takes into account everything that characterizes a specific neuron, including both internal and external physiological features such as surface properties, gating processes, electrical activity of surrounding neurons, chemical composition of extracellular liquid near the neuron, etc.

- The parameter J represents the *synaptic weight*, which we assume identical for all synapses of the network. According to the sign of J we define excitatory ($J > 0$) or inhibitory ($J < 0$) We can define a completely excitatory or inhibitory network pulses if J is a global variable.

- $S(t)$ is a variable that expresses the mean synaptic activation, i.e. a global function taking into account the effective coupling between all the neurons in the network at a certain time t. This field must be related to the past firing activity of the neurons. Considering that t_1, t_2, ..., t_M are the *past* instants of time when a neuron within the network emitted a pulse, we can define a differential equation for the average synaptic field as follows:

$$\tau_d \dot{S}(t) + S(t) = \frac{1}{N} \sum_{k=1}^{M} \delta(t - t_k), \tag{2.5.0.2}$$

  τ_d is the decay time of the synaptic field. Positive values of such constant mean an exponential decay, while $\tau_d = 0$ stands for an instantaneous decay (impulsive synapse).
  According to this picture, every time a neuron emits a pulse, all the neurons in the network immediately receive it. Moreover, this model includes self stimulation, meaning that a neuron is influenced by its own pulses.

- $I_e(t)$ is a time dependant function which stands for a possible external current applied simultaneously to all neurons of the network. In the following section of the thesis we will include the effect of the external current into the excitability term.

The dynamics of the network model with N nodes is then described by $N + 1$ initial conditions $[V_1(t_0), ..., V_N(t_0), S(t_0)]$ along with the following $N + 1$ differential equations:

$$\begin{aligned} \dot{V}_i(t) &= V_i^2(t) + \eta_i + JS(t) + I_e(t), \quad i = 1, ..., N. \\ \tau_d \dot{S}(t) + S(t) &= \frac{1}{N} \sum_{k=1}^{M} \delta(t - t_k), \end{aligned} \tag{2.5.0.3}$$

Together with the reset rule $V_i(t_k^-) = +\infty \implies V_i(t_k^+) = -\infty \; \forall k = 1, ..., M$ and $\forall i = 1, ..., N$. $\{t_k\}$ are implicitly defined by $V_j(t_k^-) = +\infty$ for some $j \in 1, ..., N$.

For practical purposes, we are interested in having multiple distinct interacting populations. Each population is made up by formally identical QIF neurons evolving according to Eq. (2.5.0.3). We now denote with A and B two populations with, respectively, N_A and N_B single QIF neurons. This system is described by $N_A + N_B + 2$ differential equations along with the same number of initial conditions:

$$\begin{aligned}
&\dot{V}_i^A(t) = V_i^2(t)^A + \eta_i + J_{AA}S^A(t) + J_{BA}S^B(t) + I_e^A(t), \quad i = 1, ..., N_A. \\
&\tau_d^A \dot{S}^A(t) + S^A(t) = \frac{1}{N_A}\sum_{k=1}^{M}\delta(t - t_k^A), \\
&\dot{V}_i^B(t) = V_i^2(t)^B + \eta_i^B + J_{BB}S^B(t) + J_{AB}S^B(t) + I_e^B(t), \quad i = 1, ..., N_B. \\
&\tau_d^B \dot{S}^B(t) + S^B(t) = \frac{1}{N_B}\sum_{k=1}^{M}\delta(t - t_k^B),
\end{aligned} \tag{2.5.0.4}$$

In this system we have introduce J_{BA} and J_{AB} which define, respectively, how strong is the synaptic influence of network B on network A and viceversa. J_{AA} and J_{BB} represent the weight of internal connections (thus defining a self interaction).

Since we are studying a system made up by a great number of components, we are interested in finding some distinctive physical quantity which could represent the overall spiking activity of the neural network. We can proceed as follows: We divide the time interval $[t_0, t]$ in which we observe the evolution of the network in L equispaced subintervals $I_1, ..., I_L$, each one of these having length $W = \frac{t-t_0}{L}$. For each of these subintervals I_L we count the number K_l of spikes emitted by any neuron belonging to the network in that specific time interval. We can thus define the following quantity:

$$R_l = \frac{1}{N}\frac{K_l}{W} \tag{2.5.0.5}$$

Here, R_l represents the average activity of a single neuron (since we divided by N) of the network. For $L \longrightarrow +\infty$, we measure the number of spikes over increasingly shorter time intervals $W \longrightarrow 0$ and therefore we can express Eq. (2.5.0.5) as a linear superposition of delta functions centered on specific firing times $t_1, ..., t_M \in [t_0, t]$.

$$r(t) = \frac{1}{N}\sum_{k=1}^{M}\delta(t - t_k) \tag{2.5.0.6}$$

We call this quantity *instantaneous population rate* or *population firing rate* i.e. the average instantaneous rate of pulse emission by neurons in the network. This definition allows us to

rewrite the expression for the synaptic field in Eq. (2.5.0.2):

$$\tau_d \dot{s}(t) + s(t) = r(t) \tag{2.5.0.7}$$

Notice that we renamed $S(t)$ as $s(t)$ to stress the fact that $s(t)$ is now a macroscopic variable. We can introduce another macroscopic quantity related to our network, which is the *average membrane potential*, defined as:

$$v(t) = \frac{1}{N} \sum_{j=1}^{N} V_j(t), \tag{2.5.0.8}$$

i.e. the simple arithmetic average of the membrane potential of each neuron in the network.

2.6. Exact macroscopic reduced model for a fully coupled network

In this section we show how to reduce *exactly*, in the termodynamic limit $N \longrightarrow \infty$ the infinite system expressed in Eq. (2.5.0.3) to a system defined by a few differential equations which express the evolution of fundamental average macroscopic quantities that describe the network activity: the instantaneous firing rate $r(t)$ Eq. (2.5.0.6), the mean membrane potential $v(t)$ Eq. (2.5.0.8) and the synaptic activation field $s(t)$ Eq. (2.5.0.2).

The results shown in this section are taken from a paper by Montbrió-Pazò-Roxin [46], where previously derived results for a phase oscillator network are extended to a network of QIF neurons [54]. In the limit of an infinite number of neurons, we can study the network as a continuum, known as *neural mass*, described through a probability density function $\rho(V|\eta, t)$ according to the following interpretation: the finite number of parameters η_i become a continuous random variable distributed according to a constant probability density function $g(\eta)$. $\rho(V|\eta, t)$, if normalized, represents the fraction of neurons having a given excitability η and a membrane potential $V \in [V, V + dV]$ at a certain time t. Therefore we have that $\int_{-\infty}^{+\infty} \rho(V|\eta, t)dV = g(\eta)$ represents the fraction of neurons having any value of the membrane potential and a given excitability η. Let

$$[a, b] = V \in \mathbb{R} : \;\; V = V(t, V_0) \;\; for \;\; V_0 \in [a_0, b_0] \tag{2.6.0.1}$$

be the set of points (membrane potentials) reached at the instant t by the paths that originate from initial conditions belonging to the interval $[a_0, b_0]$ at the initial time t_0. We know that each trajectory corresponds to the time evolution of a neuron membrane potential, thus we can exploit the fact that the number of neurons is conserved:

$$\int_{a_0}^{b_0} \rho(V_0, t_0) dV_0 = \int_a^b \rho(V, t) dV \tag{2.6.0.2}$$

Through a change of variable $V = V(t, V_0)$ in the r.h.s. integral we obtain:

$$\int_{a_0}^{b_0} \rho(V_0, t_0) dV_0 = \int_{a_0}^{b_0} \rho(V(t, V_0)) \frac{\partial V}{\partial V_0} dV_0 \tag{2.6.0.3}$$

Since this equality must hold for an arbitrary choice of a_0, b_0, we get the following expression:

$$\rho(V_0, t_0) = \rho(V(t, V_0), t) \frac{\partial V}{\partial V_0} \tag{2.6.0.4}$$

The first term is constant, thus we can derive with respect to t, by explicitly expressing the velocity field $\dot{V} = V^2 + \eta + JS + I_e$ (as described in Eq. (2.5.0.1)). This leads to a continuity equation for the probability density function:

$$\frac{\partial}{\partial t}\rho + \frac{\partial}{\partial V}\left[\rho(V^2 + \eta + JS + I_e)\right] = 0 \tag{2.6.0.5}$$

The continuity equation and the synaptic field equation Eq. (2.5.0.2) describe the continuous formulation of the neuronal network in the thermodynamic limit.

We now want to explore what kind of probability density functions satisfy Eq. (2.6.0.5). In particular, such equations admits a trivial stationary solution in the case of a constant external current. In fact, being $\frac{\partial}{\partial t}\rho = 0$, we need that $\frac{\partial}{\partial V}\left[\rho(V^2 + \eta + JS + I_e)\right] = 0$. This is trivially true for density functions having the following form:

$$\rho_0(V|\eta) \propto \frac{1}{V^2 + \eta + JS + I_e} \tag{2.6.0.6}$$

This corresponds to a Lorentzian distribution with respect to the membrane potential. This means that for neurons characterized by a given η, their membrane potential will be distributed on the V axis with a density inversely proportional to their speed $\dot{V}$ according to Eq. (2.5.0.1). We now assume that even in non-stationary cases, regardless of the initial conditions, the membrane potential are distributed according to a Lorentzian expression. This is expressed by the *Lorentzian ansatz*:

Regardless of the initial form of the distribution $\rho(V|\eta,0)$, the solution of Eq. (2.6.0.5) converge to a Lorentzian density function with respect to the membrane potential:

$$\rho(V|\eta,t) = \frac{1}{\pi}\frac{x(\eta,t)}{[V-y(\eta,t)]^2 + x(\eta,t)^2} \tag{2.6.0.7}$$

where $x(\eta,t) \geq 0$ is the half width at half maximum (HWHM) and $y(\eta,t)$ is the median

The Lorentzian ansatz (LA) consists of an assumption on the form of the attractor of the system. This attractor is a sub-variety of all possible density functions. Assuming this hypothesis is valid, we can therefore study the evolution of $x(\eta,t)$ and $y(\eta,t)$ in order to describe $\rho(V,t)$. Applying the LA, we can express $r(t)$ and $v(t)$ as follows. Since the Lorentzian distribution of the membrane potentials is symmetric and centered on $y(\eta,t)$, for each fixed η and t, then the following equation holds:

$$v(\eta,t) = y(\eta,t) = P.V. \int_{-\infty}^{+\infty} \rho(V|\eta,t) V dV \tag{2.6.0.8}$$

here, P.V. stands for the Cauchy principal value of the integral. Thus leaving us with the following expression:

$$v(t) = \int_{-\infty}^{+\infty} y(\eta,t) g(\eta) d\eta \tag{2.6.0.9}$$

We have seen that a QIF neuron spikes when its membrane potential reaches infinite value. We can therefore obtain the firing rate at a given value η and at a certain time t as the neural mass flux when V tends to infinity.

$$r(\eta,t) = \rho(V \to +\infty|\eta,t)\dot{V}(V \to +\infty|\eta,t) \tag{2.6.0.10}$$

This can be written as:

$$r(\eta,t) = \lim_{V\to+\infty}\left[\frac{1}{\pi}\frac{x(\eta,t)}{[V-y(\eta,t)]^2 + x(\eta,t)^2}(V^2 + \eta + JS + I_e)\right] \tag{2.6.0.11}$$

Due to the compensation of the quadratic term of the membrane potential, we finally get:

$$r(\eta,t) = \frac{x(\eta,t)}{\pi} \tag{2.6.0.12}$$

The instantaneous firing rate then becomes:

$$r(t) = \frac{1}{\pi}\int_{-\infty}^{+\infty} x(\eta, t)g(\eta)d\eta. \tag{2.6.0.13}$$

Now that we have given physical meaning to the main parameters, we can replace the LA relationship expressed in Eq. (2.6.0.7) in the continuity equation, which we can thus rewrite as:

$$-\frac{\partial}{\partial}\rho = \frac{\partial}{\partial V}\left[\rho(V^2 + \Lambda)\right] \tag{2.6.0.14}$$

where $\Lambda = \eta + JS + I_e$, does not depend on V. Given a Lorentzian probability density function we can explicitly derive with respect to time and membrane potential, thus obtaining, after a few calculations:

$$\begin{aligned} &-\dot{x}[(V-y)^2 + x^2] + 2x[x\dot{x} - \dot{y}(V-y)] = \\ &= -2(V-y)x(V^2+\Lambda) + 2Vx[(V-y)^2 + x^2] \end{aligned} \tag{2.6.0.15}$$

This useful relations must be satisfied $\forall V \in]-\infty, +\infty[$.
By comparing the second order terms of the membrane potential we get;

$$\dot{x} = 2xy \tag{2.6.0.16}$$

We can use this relation for the equation we obtain by comparing the first order terms of Eq. (2.6.0.15), thus assuming $x \neq 0$

$$\dot{y} = y^2 - x^2 + \Lambda \tag{2.6.0.17}$$

No new information is obtained by studying the zero-order term and the cubic term. Introducing a complex variable $w = x + iy$ we can write in a more compact form Eq. (2.6.0.17) and Eq. (2.6.0.16).

$$\dot{w} = i(\lambda - w^2) \tag{2.6.0.18}$$

Summarizing, we have seen that our continuous network system can be described by Eq. (2.6.0.5) and Eq. (2.5.0.7). In addition to that, if we assume that the membrane potential of each neuron is distributed according to a Lorentzian distribution as in Eq. (2.6.0.7), then the macroscopic system can be exactly defined by the following reduced system:

$$\begin{aligned} &\frac{\partial}{\partial t}w(\eta, t) = i[\eta + Js(t) + I_e(t) - w(\eta, t)^2], \\ &\tau_d\frac{\partial}{\partial t}s(t) + s(t) = \frac{1}{\pi}\int_{-\infty}^{+\infty} x(\eta, t)g(\eta)d\eta. \end{aligned} \tag{2.6.0.19}$$

The system is thus described by the average macroscopic quantities $w(\eta,t) = x(\eta,t) + iy(\eta,t)$ and $s(t)$.

We note that, for a correct derivation of the macroscopic model, we need to assume that $x(\eta,t) \neq 0 \,\forall\, \eta \in \mathbb{R}, t > 0$. To ensure that $w(\eta,0)$ really represents a physical solution to our problem at any time $t > 0$, we must impose that $Re(w(\eta,t)) \geq 0 \,\forall\, t > 0$, as it defines the distribution width through the firing rate. It can be shown that, if the real functions $x(\eta,0)$, $y(\eta,0)$ depending on the real variable η, satisfy the following relations:

(i) $x(\eta,0) \neq 0 \quad \forall \eta \in \mathbb{R}$;

(ii) $x(\eta,0)$ and $y(\eta,0)$ are analitically continued from $\eta \in \mathbb{R}$ to $\eta \in \mathbb{I}^- = z \in \mathbb{C} : Im(z) \leq 0$ without singularities and these extensions satisfy

$$\lim_{Im(\eta \longrightarrow -\infty)} x(\eta,0) = \lim_{Im(\eta \longrightarrow -\infty)} y(\eta,0) = 0 \tag{2.6.0.20}$$

then $w(\eta,t)$, evolving through Eq. (2.6.0.19) satisfies both conditions at all times $t > 0$. This evolution law prevents w from crossing the imaginary axis and thus it ensures to remain confined in $Re(w) \geq 0$. We can therefore precisely define the shape of the LA attractor as

$$M = \left[\rho(V|\eta,0) = \frac{1}{\pi} \frac{x(\eta,0)}{[V - y(\eta,0)]^2 + x(\eta,0)^2} : w = x + iy \; satisfy \, (I), (II) \right] \tag{2.6.0.21}$$

As a further step, we assume that η is a random parameter distributed according to a Lorentzian density

$$g(\eta) = \frac{1}{\pi} \frac{\Delta}{(\eta - H)^2 + \Delta^2}. \tag{2.6.0.22}$$

Here H is the position of the peak on the η axis while $\Delta \geq 0$ is the amplitude parameter.

This assumption is not correlated with the aforementioned LA. However, it allows us to explicitly obtain an analytical expression for $r(t)$ and $v(t)$.

We extend the real variable η to a complex variable $\eta = \eta_r + i\eta_i$ and we extend analytically $w(\eta,t)$ and $g(\eta)$ from $\eta \in \mathbb{R}$ to the complex half-plane with negative imaginary part, $\eta\mathbb{I}^-$. The function $g(\eta) : \mathbb{I}^- \longrightarrow \mathbb{C}$ admits a single pole of order 1 in $\eta = H - i\Delta$

$$g(\eta) = \frac{1}{\pi} \frac{\Delta}{[\eta - (H + i\Delta)][\eta - (H - i\Delta)]}. \tag{2.6.0.23}$$

We can proceed by calculating the two integrals Eq. (2.6.0.13) and Eq. (2.6.0.9) through the residue theorem, from which it follows that:

$$w(H - i\Delta, t) = \pi r(t) + iv(t), \tag{2.6.0.24}$$

and therefore the firing rate and the average membrane potential $v(t)$ depend only on the value of w on the pole of $g(\eta)$ located in the lower half-plane. To obtain an explicit time-dependant solution we evaluate Eq. (2.6.0.19) in $\eta = H - i\Delta$

$$\begin{aligned} &\frac{\partial}{\partial t}[\pi r(t) + iv(t)] = iH - i\Delta + Js(t) + I_e(t) - [\pi^2 r^2(t) - v^2(t)] + i2\pi r(t)v(t), \\ &\tau_d \frac{\partial}{\partial t} s(t) + s(t) = \frac{1}{\pi} \int_{-\infty}^{+\infty} x(\eta, t) g(\eta) d\eta. \end{aligned} \tag{2.6.0.25}$$

At this point, according to which assumptions we make on the synaptic dynamics and other physiological phenomena (such as adaptation) we get different reduced models for the populations of QIF neurons.

Instantaneous synapses. $\tau_d = 0$:

We assume that the interaction between two neurons is a completely impulsive, instantaneous event. In this case we immediately get $s(t) = r(t)$. Thus breaking down equations Eq. (2.6.0.25) into real and imaginary part we obtain the following real two-dimensional system

$$\begin{aligned} \tau \dot{r} &= \frac{\Delta}{\tau\pi} + 2rv \\ \tau \dot{v} &= v^2 + \eta - (\pi\tau r)^2 - Jr\tau + I_e \end{aligned} \tag{2.6.0.26}$$

This nonlinear system describes exactly, from a macroscopic point of view, a population of QIF neurons within the limit of an infinite number of neurons. It's interesting to observe that the nonlinear term $\pi^2 r^2$, acting as a negative correction to $\dot{v}$, prevents an uncontrolled growth of $v(t)$ by decreasing the membrane potential when the firing rate increases.

Exponentially decaying synapses. $\tau_d > 0$:

We now assume that the interaction between neurons is an impulsive event with an exponential decay, i.e. $\tau_d > 0$. In the thermodynamic limit of infinite QIF neurons we obtain the following system of ordinary differential equations:

$$\begin{aligned}
\tau\dot{r} &= \frac{\Delta}{\tau\pi} + 2rv \\
\tau\dot{v} &= v^2 + \eta - (\pi\tau r)^2 - Js\tau + I_e \\
\tau_d\dot{s} &= -s + r
\end{aligned} \tag{2.6.0.27}$$

The coordinate $s(t)$ defines the average dynamics of synapses, which, in this case, results in an exponential decay with decay constant τ_d, driven by the positive action of the firing rate r. Furthermore, the synaptic field affects the average membrane potential according to the specific type of synapses. We note, however, that the fixed points are the same in both systems, as for stationary solution we get once again that $s(t) = r(t)$. Despite this, as we will se in subsequent sections, exponentially decaying synapses can change stability and bifurcation processes.

Decaying synapses and adaptability

$$\begin{aligned}
\tau\dot{r} &= \frac{\Delta}{\tau\pi} + 2rv \\
\tau\dot{v} &= v^2 + \eta - (\pi\tau r)^2 + Jr\tau + I_e \\
\tau_d\dot{s} &= -s + r \\
\tau_A\dot{A} &= -A + \alpha\tau r
\end{aligned} \tag{2.6.0.28}$$

Here we have an additional equation for the time evolution of the new coordinate A which represents the adaptation dynamics, which has inhibitory effect on the membrane potential through a negative additive term. We assume τ_A to be the time scale for adaptation processes while α describes the strength of the perturbative effects of the firing rate on the evolution of A. In the following section we will study in detail the dynamics of this system.

Chapter 3

Single population models

In this chapter we explore in further detail the neural mass models in a single population configuration that we presented at the end of Chapter 2.

3.1. Instantaneous synapses

$$\tau \dot{r} = \frac{\Delta}{\tau\pi} + 2rv \tag{3.1.0.1}$$

$$\tau \dot{v} = v^2 + \eta - (\pi\tau r)^2 - Jr\tau + I_e \tag{3.1.0.2}$$

As previously stated, this nonlinear system describes exactly a population of QIF neurons in the limit of infinite neurons.

We proceed by studying the fixed points of the system, which are those solutions with firing rate and the membrane potential constant in time (i.e. $\dot{r} = \dot{v} = 0$). We immediately see that, if $v = 0$, then Eq. (3.1.0.1) becomes $\dot{r} = \frac{\Delta}{\tau^2\pi}$ thus meaning that we cannot have a fixed point with $v = 0$. With this assumption we look for solutions with $\dot{r} = 0$ and we obtain:

$$r = -\frac{\Delta}{2\tau\pi v} \tag{3.1.0.3}$$

Since $\tau\dot{v} = v^2 + \eta + Jr\tau - (\pi r\tau)^2 + I_e(t)$, then $\dot{v}$ can be equal to zero (when r is constant) only if $I_e(t)$ is constant as well.

By replacing r in Eq. (3.1.0.2) with the expression we found in Eq. (3.1.0.3) and assuming $\dot{v} = 0$, we get:

$$v^2 + \eta - \frac{\Delta J}{2\pi} \cdot \frac{1}{v} + I_e - \frac{\Delta^2}{4} \cdot \frac{1}{v^2} = 0. \tag{3.1.0.4}$$

The roots of this equation will give us the projections on the membrane potential coordinate for fixed points of our system.

We want to study qualitatively Eq. (3.1.0.4) in order to gain more insights about the stability of our system. We begin by rearranging Eq. (3.1.0.2) with the aid of Eq. (3.1.0.3), thus obtaining:

$$\dot{v} = \frac{\Delta^2}{4}[A_\alpha(v) - B_\beta(v)], \tag{3.1.0.5}$$

where $A_\alpha(v) = \frac{4}{\Delta}[v^2 + \alpha]$ and $B_\beta(v) = \frac{1}{v^2} + \frac{2}{\pi}\beta\frac{1}{v}$, with $\alpha = \eta + I_e$ and $\beta = \frac{J}{\Delta}$. These two parameters will prove themselves qualitatively relevant in defining the dynamical behaviour of the system. α represents an effective excitability taking into account both the mean excitability η and the external current (which we assume to be constant for now).

By overlapping the two functions $A_\alpha(v)$ and $B_{\beta(v)}$ in the same plane we can easily study the fixed points as $\dot{v} = 0 \iff A_\alpha(v) = B_\beta(v)$. In addition to that, we note that $sgn(\dot{v}) = sgn(A_\alpha(v) - B_\beta(v))$.

Due to the symmetry $B_\beta(-v) = B_{-\beta}(v)$ we only need to study the excitatory case (i.e. $J > 0$). In order to draw a qualitative plot of $B_\beta(v)$ we can study the boundary limits of the function, thus obtaining $(v_{min}, B_\beta(v_{min})) = (-\frac{-\pi}{\beta}, -\frac{\beta^2}{\pi^2})$ as shown in Fig. 3.1.1 through a dashed line. This implies that as β increases, the minimum point of the function moves down and approaches the $x = 0$ axis according to a behaviour described by $h(v) = -\frac{1}{v^2}$. $A_\alpha(v)$ has the shape of a parabola; increasing α has the effect of translating the function upwards.

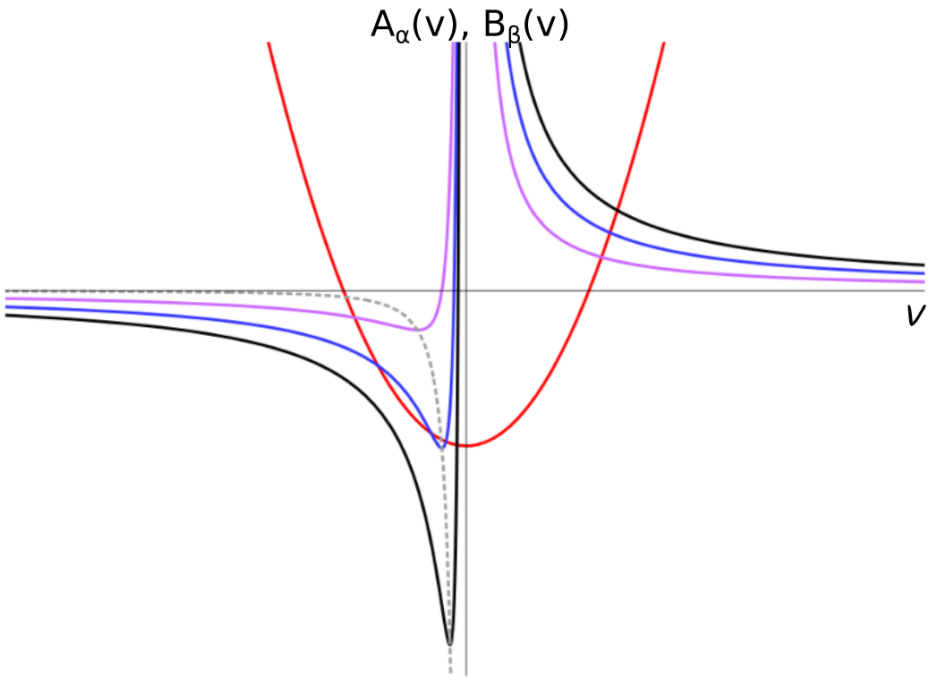

Figure 3.1.1: In red the function $A_\alpha(v)$ with $\alpha = -2.5$ and $\Delta = 1$. In black, blue and purple the function $B_\beta(v)$ with, respectively $\beta = 5, 10, 15$. The dashed line represents the minima of $B_\beta(v)$ with respect to v for different β values.

At most, we can have four distinct intersections between the two functions, that is four distinct equilibrium points, arranged according to their projection on the v axis as $v_1 \leq v_2 \leq v_3 < 0 < v_4$. The stability of these solutions is given by the relative position of the two functions and can thus be determined graphically. We obtain that v_4 is always unstable, while for those solutions such that $v < 0$ we see that v_1 and v_3 are stable and v_2 is unstable.
We need to highlight the fact that only solutions with $v < 0$ have physical sense, since we require that the firing rate is positive. The firing rate is in fact an average quantity of the pulses emitted by the neurons in the network and it cannot be negative. Luckily, we see that for any choice of the parameters α and β there always exists at least a stable fixed point with $v < 0$ and $r > 0$.

Distinct equilibrium points related to negative membrane potential values might merge according to the values of α and β (which directly determine how the intersection between the two functions occurs). This gives rise to bifurcation phenomena, which are drastic changes in the dynamical behaviour of a system due to variation of one or more of its parameters (see Appendix A for

more details). We are able to express analytically the parametric curves in the (α, β) plane where these bifurcations occur through the geometric intersection condition $A'_\alpha = B'_\beta$. We thus obtain the following system:

$$\begin{aligned} A_\alpha(v) &= B_\beta(v) \\ A'_\alpha(v) &= B'_\beta(v) \end{aligned} \tag{3.1.0.6}$$

We can express α and β as functions of v and Δ and we plot the smooth curve in Fig. 3.1.2 (a). Since those tangency points can be locally approximated as a straight line (A_α) intersecting a second-order curve (B_β), then the bifurcations occurring can be classified as a $saddle - node$. In a particular case we can also observe a pitchfork bifurcation (see appendix).

The dynamical behaviour by varying J, Δ, η is shown in Fig. 3.1.2 (a). In the excitatory case, according to the parameters values, we can have a single stable equilibrium solution or a coexistence between two stable points (bistability) and an unstable point.

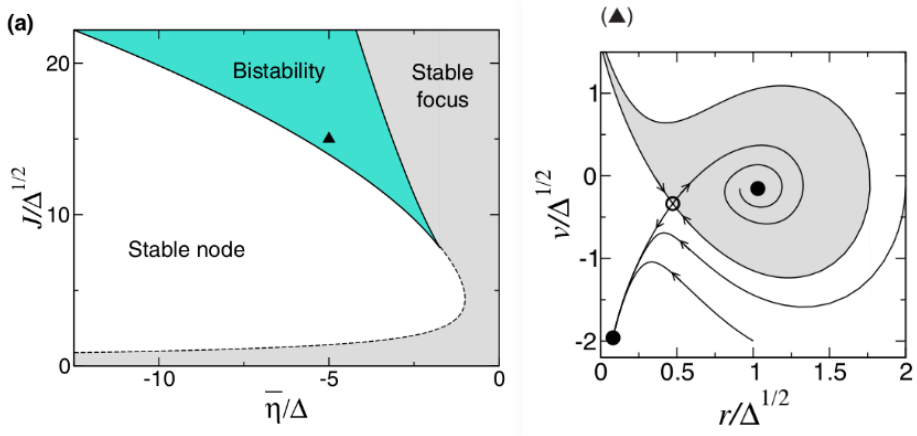

Figure 3.1.2: The two diagrams are obtained with a vanishing external current $I_e = 0$. On the left: in white we see the parameter plane region where the system trajectory is attracted by a stable node, in gray the region where the system is attracted by a stable focus. In turquoise the region of the parameter plane where bistability exists. On the right: representation of the dynamics of the system in the renormalized phase plane $(r/\sqrt{\Delta}, v/\sqrt{\Delta},)$ for a specific point of phase plane on the left denoted by the triangle. Figure taken from [46]

In Fig. 3.1.2 (a), crossing the smooth curve (leaving the turquoise region) corresponds to a saddle-node bifurcation where the equilibrium points v_1 and v_2 or v_2 and v_3 merge and then dis-

appear. Instead, crossing the dashed curve represents the transformation of the single attractive equilibrium point from node to focus or viceversa.

Fixed points linear stabilty analysis

The linear stability of fixed points can be studied by looking at the eigenvalues of the system's Jacobian matrix calculated at the equilibrium point (r_0, v_0) which, according to Eq. (3.1.0.2), is given by:

$$J_F(r_0, v_0) = \begin{bmatrix} 2v_0 & 2r_0 \\ J - 2\pi^2 r_0 & 2v_0 \end{bmatrix} \tag{3.1.0.7}$$

The matrix shown in Eq. (3.1.0.7) represents the linearized system around the equilibrium point. The eigenvalues are obtained as the roots of the characteristic polynomial:

$$p(\lambda) = det \begin{bmatrix} 2v_0 - \lambda & 2r_0 \\ J - 2\pi^2 r_0 & 2v_0 - \lambda \end{bmatrix} = \lambda^2 - 4v_0\lambda + (4v_0^2 + 4\pi^2 r_0^2 - 2r_0 J). \tag{3.1.0.8}$$

This means that the eigenvalues are:

$$\lambda_\pm = 2v_0 \pm \frac{\sqrt{D}}{2}, \tag{3.1.0.9}$$

where $D = 8r_0 J - (4\pi r_0)^2$. In particular, the synaptic weight J plays a fundamental role in the fixed point stability. Referring only to the fixed points with physical meaning (i.e. $r_0 > 0$), we get the following picture:

- $J < 2\pi^2 r_0 \longrightarrow (r_0, v_0)$ stable focus.
  This condition is equal to $D < 0$, thus the eigenvalues always have non-zero imaginary part (focus). Furthermore, $\mathrm{Re}(\lambda_\pm) = v_0$ are always negative (stability condition).

- $2\pi^2 r_0 < J < 2\pi^2 r_0 + 2v_0^2/r_0 \longrightarrow (r_0, v_0)$ stable node.
  The first condition implies that $D > 0$, thus both eigenvalues are purely real. The second condition tells us that $\lambda_+ = 2v_0 + \frac{\sqrt{D}}{2} < 0$, thus both fixed points are stable as well.

- $J > 2\pi^2 r_0 + 2v_0^2/r_0 \longrightarrow (r_0, v_0)$ unstable saddle-node.
  In such cases we have $\lambda_+ > 0$ thus the fixed point is unstable, while the other eigenvalue $\lambda_- = 2v_0 - \frac{\sqrt{D}}{2}$ is negative, thus giving birth to an unstable saddle-node.

When passing from $D > 0$ to $D < 0$ the fixed point eigenvalues get closer, moving along the real negative semi-axis, until they merge for $D = 0$. For furtherly decreasing D values, they separate into a couple of complex conjugate eigenvalues. When this happens the stable node turns into a stable focus. In order to obtain analitically the curve in the (α, β) where this phenomenon

occurs, we can just set $D = 0$, that is $J = 2\pi^2 r_0$. From this and from Eq. (3.1.0.3), we get v_0 as a function of J, which, replaced into Eq. (3.1.0.4) gives us an equation in the coefficients α and β thus allowing us to obtain the expression for the dashed line in Fig. 3.1.2 (a).
Looking at Eq. (3.1.0.9) we see that the real part of the eigenvalues can't be equal to zero. This means that Hopf bifurcations are not allowed, thus self-sustained oscillations cannot be generated for this kind of system.

Inhibitory case:
In the inhibitory case we have $J < 0$ and thus $\beta < 0$. Plots for A_α and B_β are obtained from those in Fig. 3.1.1 through a reflection with respect to the ordinate axis. Therefore there always exists a single stable equilibrium solution with physical significance. What we discussed previously on the stability of this solution can be applied in the inhibitory case as well.

3.2. Exponentially decaying synapses

In this section we study the reduced QIF model assuming that the interaction between two neurons is a completely impulsive event that decays exponentially. As discussed before, this assumption translates into making $\tau_d > 0$ in the synaptic field equation. From this choice we get the following system:

$$\begin{aligned} \tau \dot{r} &= \frac{\Delta}{\tau\pi} + 2rv \\ \tau \dot{v} &= v^2 + \eta - (\pi\tau r)^2 + Js\tau + I_e \\ \tau_d \dot{s} &= -s + r \end{aligned} \tag{3.2.0.1}$$

The s coordinate is an average of the synaptic activity, which in this case has the shape of an exponential decay, with τ_d decay constant, (driven) by the positive action of the firing rate r. Furthermore, the s field affects the mean membrane potential of the network by acting positively or negatively according to the type of synapses, respectively excitatory ($J > 0$) or inhibitory ($J < 0$).
The fixed points of the system are exactly the same as for the case of instantaneous synapses; in fact, from $\dot{s} = 0$ it follows that $s = r$ and thus we find once again the same algebric equations (Eq. (3.1.0.4) and Eq. (3.1.0.3)) of the previously studied system.

This means that introducing exponentially decaying synapses does not change the value of fixed points but, as we will see, it changes their stability and bring forth new bifurcation processes. In particular, the attractive focus can lose stability through a Hopf bifurcation, which gives raise to self-sustained oscillations (in the form of a limit cycle).

Given a fixed point with physical meaning:

$$\begin{aligned} r_0 &> 0 \\ v_0 &< 0 \\ s_0 &> 0, \end{aligned} \tag{3.2.0.2}$$

we study its stability through the explicit calculation of the linearized system in that phase space point.

The characteristic polynomial is given by:

$$det \begin{bmatrix} 2v_0 - \lambda & 2r_0 & 0 \\ -2\pi^2 r_0 & 2v_0 - \lambda & J \\ -\frac{1}{\tau_d} & 0 & -\frac{1}{\tau_d} - \lambda \end{bmatrix} = -\frac{1}{\tau_d}(1 + \lambda\tau_d)[(2\pi r_0)^2 - (2v_0 - \lambda)^2] + 2r_0 J. \tag{3.2.0.3}$$

Thus we need to find the roots of the following polynomial:

$$p(\lambda) = \tau_d\lambda^3 + A\lambda^2 + (\tau_d B + 4v_0)\lambda + (B + 2r_0 J), \tag{3.2.0.4}$$

where $A = (1 - 4v_0\tau_d)$ and $B = (2\pi r_0)^2 - (2v_0)^2$. Such polynomial, as opposed to the one with instantaneous synapses, can have imaginary roots with vanishing real part. By imposing $\lambda = i\Omega$ (with $\Omega \in \mathbb{R}/0$), after some calculations we find that $p(i\Omega) = 0$ if and only if Ω satisfies:

$$\begin{aligned} Re(p(i\Omega)) = 0 \qquad & A\Omega^2 + (B + 2r_0 J) = 0; \\ Im(p(i\Omega)) = 0 \qquad & \tau_d\Omega^2 + (4v_0 + \tau_d B) = 0. \end{aligned} \tag{3.2.0.5}$$

Assuming that $B + 2r_0 J < 0$ and $4v_0 + \tau_d B < 0$ both equations in Eq. (3.2.0.5) have real solutions given by:

$$\Omega_{Re,\pm} = \pm\frac{\sqrt{-A(B + 2r_0 J)}}{A} \tag{3.2.0.6}$$

$$\Omega_{Im,\pm} = \pm\frac{\sqrt{-\tau_d(4v_0 + \tau_d B)}}{\tau_d} \tag{3.2.0.7}$$

Now we want to find an equation for the system parameters such that the two equations in Eq. (3.2.0.5) have the same solutions, i.e. $\Omega_{Re,\pm} = \Omega_{Im,\pm}$. An explicit expression of J as a function of τ_d, r_0, v_0 can thus be found as follows:

$$J_H = \frac{2v_0}{r_0\tau_d}[(1-2v_0\tau_d)^2 + (2\pi r_0\tau_d)^2]. \tag{3.2.0.8}$$

J_H, as derived, is negative. This implies that the equilibrium state which goes through the bifurcation is a stable focus, as we expected. J_H represents the critical value for the synaptic weight at which the focus (r_0, v_0) loses stability through a Hopf bifurcation, giving raise to a stable limit cycle. Moreover, substituting J_H in Eq. (3.2.0.6) provides us with the oscillations' frequency Ω_H as a function of τ_d, r_0, v_0.

From Eq. (3.2.0.8) and Eq. (3.2.0.2) it follows that the Hopf bifurcation occurs only for negative values of the synaptic weight $J_H < 0$, that is for inhibitory networks. Due to this evidence, in order to counterbalance the inhibitory effects of the pulses, neurons have to be distributed around a positive average excitability value. Thus, from now on, we assume for simplicity that $I_e = 0$ and that $\eta = 1$. The algebric equations of fixed points will be:

$$\begin{aligned} v_0 &= -\frac{\Delta}{2\tau\pi r_0} \\ v_0^2 &+ \eta + Jr_0 - \pi^2 r_0^2 = 0 \end{aligned} \tag{3.2.0.9}$$

We now look for a set of parameters J, Δ, τ_d that allows the system to oscillate. Replacing the expression for J_H in Eq. (3.2.0.9), we obtain an expression for τ_d as a function of the fixed point coordinates. We get two distinct solutions:

$$\tau_{d,H}^{\pm} = \frac{1}{16v_0(\pi^2 r_0^2 + v_0^2)}\left[\pi^2 r_0^2 - 1 + 7v_0^2 \pm \sqrt{(\pi^2 r_0^2 - 1)^2 - (14 + 50\pi^2 r_0^2)v_0^2 - 15v_0^4}\right]. \tag{3.2.0.10}$$

Clearly, thanks to Eq. (3.2.0.9) we can express $\tau_{d,H}^{\pm} = \tau_{d,H}^{\pm}(r_0; \Delta)$ as a function of the coordinate r_0 and of the parameter Δ. In Fig. 3.2.1 the two functions $\tau_{d,H}^{+}$ and $\tau_{d,H}^{-}$ of the variable r_0 are shown for a few different values of Δ. These two functions are joint at their respective ends thus defining a closed curve which encloses the region where the system oscillates. As we can see in Fig. 3.2.1, the oscillations region gets smaller and smaller as Δ (the heterogeneity) increases, until it collapses to a point and disappears. In order to find the exact Δ value at which the oscillations disappear we proceed as follows: First of all we see that the two functions in Eq. (3.2.0.10) join when the radicand vanishes. By imposing this condition we find the following solution:

$$\Delta_H(r_0) = \frac{2\pi r_0}{15}\sqrt{-7 - 25\pi^2 r_0^2 + 8\sqrt{1 + 5\pi^2 r_0^2 + 10\pi^4 r_0^4}}, \tag{3.2.0.11}$$

which is shown in Fig. 3.2.1 on the right.

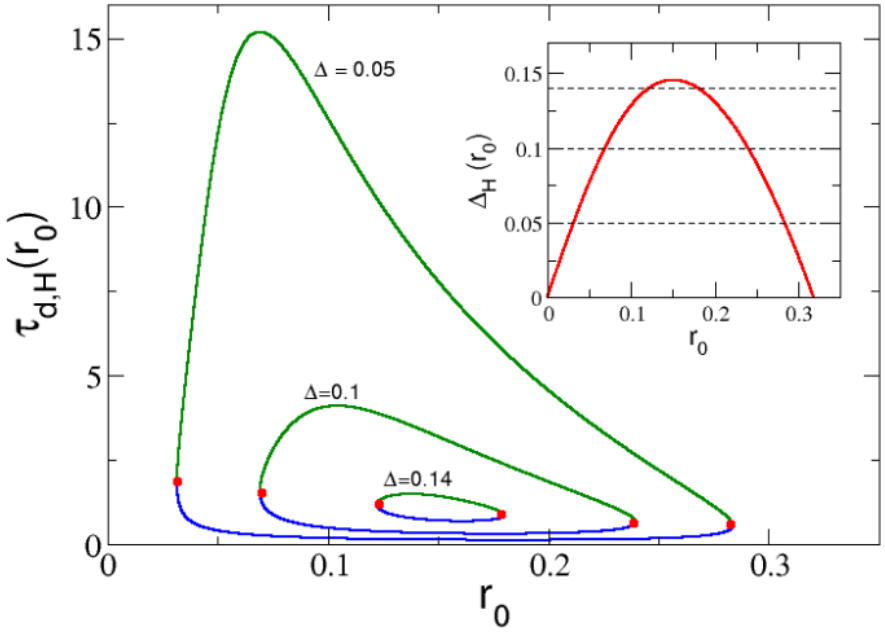

Figure 3.2.1: Plot of $\tau^{\pm}_{d,H}$ as functions of r_0 from Eq. (3.2.0.10), at three different Δ values. The red points denote where the two curves have a common point. These values are given from the function $\Delta_H(r_0)$ in Eq. (3.2.0.11) which is shown in the inset as a red curve. The horizontal dashed lines correspond to the chosen Δ for the three plots.

Thus the aforementioned critical value where the oscillations vanish can be calculated as the maximum value of the function in Eq. (3.2.0.11). The firing rate value for which we have a maximum is $r_0 = \frac{1}{\pi\sqrt{2\sqrt{5}}} \approx 0.1505$ to which the following critical value corresponds:

$$\Delta_c = \frac{1}{5}\sqrt{5 - 2\sqrt{5}} \approx 0.1453 \tag{3.2.0.12}$$

In a network with a heterogeneity value greater than Δ_c, the reduced system does not oscillate. Finally, we show the region in the parameter plane (J, τ_d) where oscillations occur for some values of Δ (see Fig. 3.2.2). Such curves can be expressed analitically as functions of r_0 and Δ with the following form:

$$(J, \tau_d)^{\pm}_H = \left(\frac{v_0^2}{r_0} + \frac{1}{r_0} - \pi^2 r_0, \tau_{dH}^{\pm}(r_0; \Delta)\right) = \left(\frac{\Delta^2}{4\pi^2 r_0^3} + \frac{1}{r_0} - \pi^2 r_0, \tau^{\pm}_{d,H}(r_0; \Delta)\right). \tag{3.2.0.13}$$

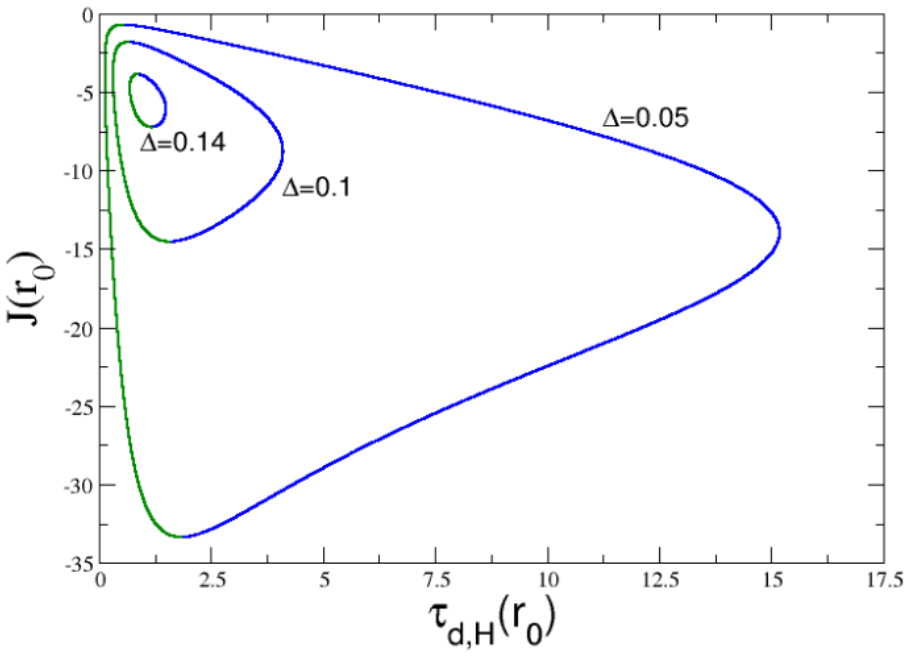

Figure 3.2.2: Plot of the curves defined in Eq. (3.2.0.13) for three different values of Δ. The region inside such curves defines the parameter set where oscillations occur.

As an example of the dynamical behaviour that our system can express, in Fig. 3.2.3 we observe the oscillating regime of a reduced network of QIF neurons with exponentially decaying synapses, i.e. the time evolution of the coordinates for the limit cycle.

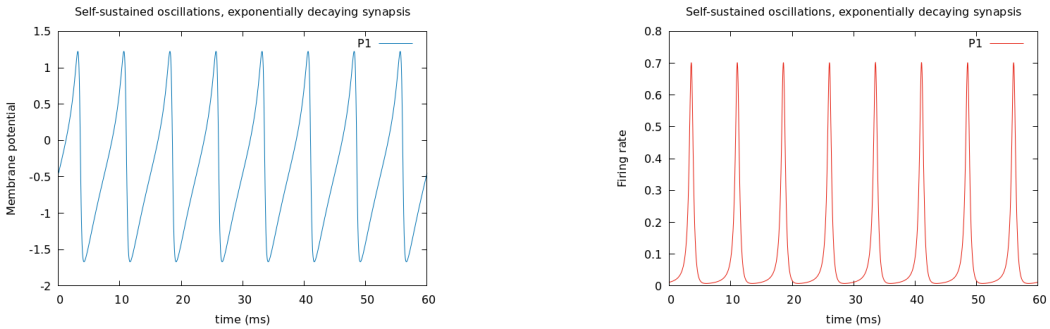

Figure 3.2.3: Dynamical simulation inside the oscillating region. Time evolution of Eq. (3.2.0.1) with $J = -15$, $\Delta = 0.05$, $\eta = 1$, $\tau = 1ms$, $\tau_a = 2ms$.

In conclusion, we have seen that for a certain range of τ_d the system can express oscillating behaviour. However, this phenomenon is shut down for extremely low τ_d, when the system becomes very similar to the one with impulsive synapses, and for τ_d values that are much larger than the time constant of membrane potential evolution.

Single population neural mass models usually do not express self-sustained oscillations without the effect of another interacting population or a time-dependant external current; the exponentially decaying synapses coupled with an inhibitory self-interaction is an exception (not the only one, though) to this rule. This is due to the fact that in order to observe collective oscillations we need the interaction between two physical processes with two different time scales, which in this specific case are τ and τ_d.
In the following, we will see that introducing the effect of neuron adaptation will allow the system to retain this behaviour under certain conditions.

3.3. Adaptation and exponentially decaying synapses

In this section we study the behaviour of a network of QIF neurons with exponentially decaying synapses and adaptation. As we introduced in the previous chapter the system is described by the following system of ordinary differential equations:

$$\begin{aligned}
\tau\dot{r} &= \frac{\Delta}{\tau\pi} + 2rv \\
\tau\dot{v} &= v^2 + \eta - (\pi\tau r)^2 + Js\tau + I_e - A \\
\tau_d\dot{s} &= -s + r \\
\tau_A\dot{A} &= -A + \alpha\tau r
\end{aligned} \tag{3.3.0.1}$$

The new variable A represents the effect of the short-term spike-frequency adaptation (SFA) mechanism we want to introduce in our system. SFA is a homeostatic mechanism that acts via spike-triggered balancing currents [3]. In our system, the evolution of A is given by an exponentially decaying process with time constant τ_a affected by the firing rate through an additive term $\alpha\tau r$. τ is the membrane's time constant and α denotes the strength of the perturbation effect. The adaptive variable A affects the evolution of the network through a negative additive term in the evolution of the membrane potential. Since we require A to be positive for having a physically reasonable solution, this implies that the adaptation has an overall inhibitory effect.

Furthermore, we focus only on inhibitory self-interactions $J < 0$ as the biological processes to which we want to apply this network only involve inhibitory neuron populations. For these two reasons we decide to focus only on positive neuronal excitability $\eta > 0$ (i.e. we consider a network of tonic neurons), as having only inhibitory effects on the network evolution could shut down any interesting bursting activity.

Our aim is to investigate whether a stable collective bursting behaviour can arise even though the adaptation has an inhibitory effect on the membrane potential. In order to do that, we start by studying a generic fixed point. We immediately see that for ($\dot{s} = \dot{A} = \dot{r} = \dot{v} = 0$) we have $s = r$ and $A = \alpha\tau r$. This implies that the algebric equations for fixed points are given by:

$$\begin{aligned} v_0 &= -\frac{\Delta}{2\pi r_0} \\ v_0^2 + \eta + Jr_0 - \pi^2 r_0^2 - \alpha r_0 &= 0 \end{aligned} \tag{3.3.0.2}$$

This equation system looks very similar to the one defined in Eq. (3.2.0.9). However, due to the effect of the new additive term, the coordinates for the fixed points now change as opposed to the previously studied system without adaptation. For low values of the α parameter this effect might be negligible as r is usually lower than the other additive terms.
In order to study the linear stability of a fixed point, we can extract the eigenvalues as the roots of the characteristic polynomial:

$$det \begin{bmatrix} 2v_0 - \lambda & 2r_0 & 0 & 0 \\ -2\pi^2 r_0 & 2v_0 - \lambda & J & -\frac{1}{\tau} \\ \frac{1}{\tau_d} & 0 & -\frac{1}{\tau_d} - \lambda & 0 \\ \frac{\tau\alpha}{\tau_d} & 0 & 0 & -\frac{1}{\tau_a} - \lambda \end{bmatrix} \tag{3.3.0.3}$$

Since an analytical discussion of this system might prove quite demanding, we decide to use the software MATCONT [18]. MATCONT is a well known Matlab package which allows numerical continuation of stable equilibrium points and linear stability analysis of such solutions. Moreover, MATCONT identifies the kind of bifurcations which give birth to new dynamical solutions.
The starting point is choosing a set of parameters for which we expect to have a fixed point. We choose:

$$\alpha = 5;\ \eta = 1;\ J = -8;\ \Delta = 0.12;\ \tau = 10ms;\ \tau_d = 20ms;\ \tau_a = 100ms. \tag{3.3.0.4}$$

The values for J, Δ, η and τ_d have been chosen as they were close to the Hopf bifurcation in the

previous system. According to biological reasons the decay time constant of adaptation should be greater than both the membrane time and the synaptic decay time [28], thus we chose an explorative value of $\tau_a = 100ms$. $\tau = 10ms$ is a biologically reasonable membrane time constant. By exploring the various parameter planes, we see that once again there exists a Hopf bifurcation, so we can have self sustained oscillations (i.e. a constant firing regime).
To explore the effect of the adaptation on the limit cycle, we follow the stability of the hopf bifurcation in the (α, J) plane, as shown in Fig. 3.3.1.

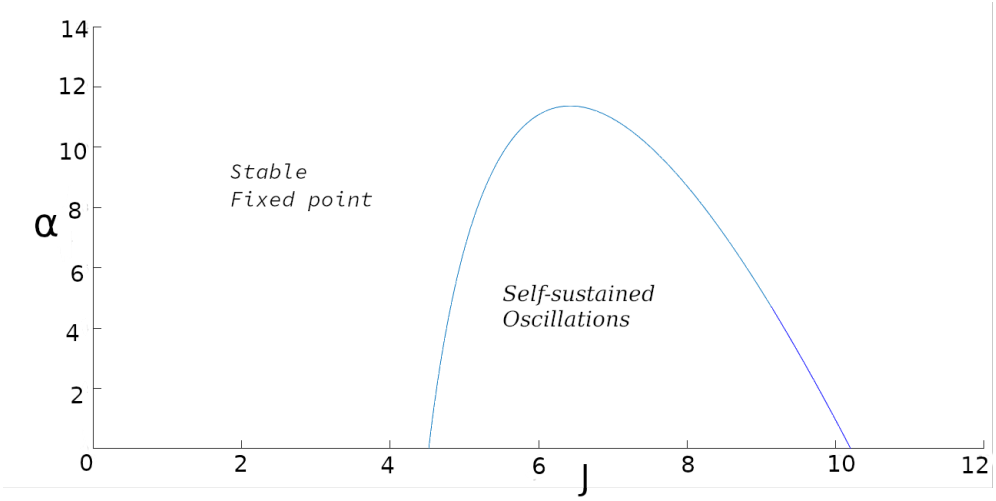

Figure 3.3.1: Phase plane (α, J). We see that for large values of α the oscillation region gets smaller and eventually disappears. Other parameters are $\eta = 1; \Delta = 0.12; \tau = 10\,ms; \tau_d = 20\,ms; \tau_a = 100\,ms$

We see that for high value of α (thus with high adaptive effects) the oscillation region disappears. With the aim of understanding this effect, we observe the parameter plane (J, τ_d), shown in Fig. 3.3.2

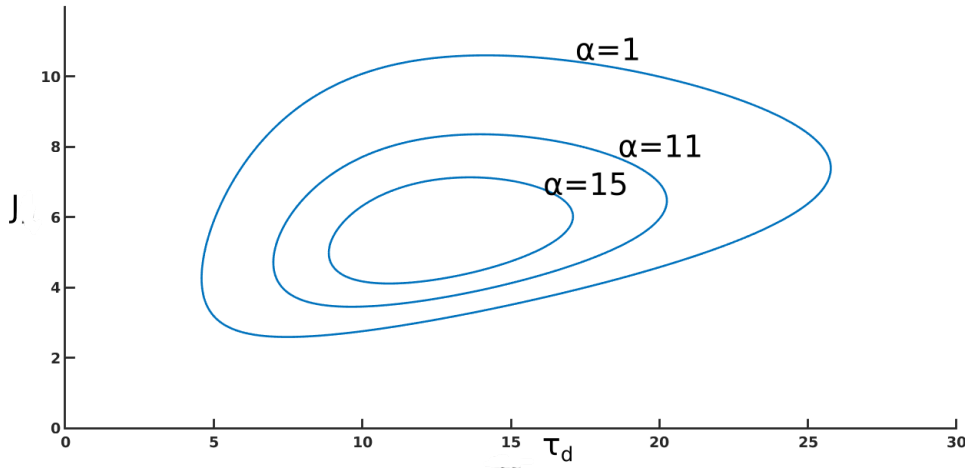

Figure 3.3.2: Hopf bifurcation curve in the parameter plane (J, τ_d). We see that for increasing values of α the closed curve tends to shrink until eventually it disappeard for a high enough α. Other parameters are $\eta = 1$; $\Delta = 0.12$; $\tau = 10\,ms$; $\tau_a = 100\,ms$

Here it's evident that having high adaptation tends to reduce the extension of the oscillating region. This is similar to the effect of increasing Δ for the Hopf bifurcation as seen in Fig. 3.2.2. Therefore, given a fixed value τ_d, for which the system without adaptation expresses oscillations, there exists a positive α_0 such that for $\alpha > \alpha_0$, self sustained oscillations are shut down. As an example, for $\tau_d = 20\,ms$, we get that $\alpha_0 \approx 11.7$, as can bee seen in Fig. 3.3.1.

It's interesting to investigate whether the time constant τ_d has a decisive influence on the Hopf bifurcation. By following the bifurcation stability on the (J, τ_a) plane we see that for increasing decaying adaptation times, the synaptic weight at which the bifurcation occurs does not vary significatively unless $\tau \approx \tau_a$. Since we assumed that for biologically relevant situation $\tau_a > \tau$, we are not interested in that region of the phase plane.

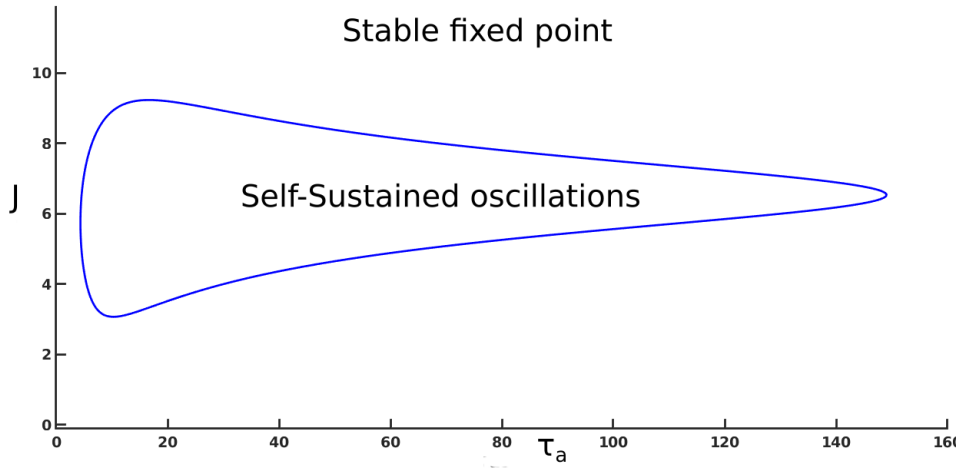

Figure 3.3.3: Hopf bifurcation stability in the plane (J, τ_a). The curve defines two distinct regions where oscillations can or cannot occur. Chosen parameters are $\eta = 1$; $\Delta = 0.12$; $\tau = 10ms$; $\tau_d = 20ms$;

In Fig. 3.3.4 we see some examples of the dynamical behaviour of the system inside the Hopf region. It's interesting to make a comparison between the dynamics with or without adaptation; we see that the frequency of oscillations slightly decreases due to adaptation effects ($\nu \approx 17Hz$ for $\alpha = 0$ and $\nu \approx 16Hz$ for $\alpha = 10$.) This means, as expected, that adaptation increases the time needed to fire an action potential. In fact, the overall inhibition effect of adaptation can be seen in the slightly different shape of the firing rate and membrane potential peaks. Furthermore, we see that the coordinate A oscillates with the same frequency as the firing rate, exhibiting however a constant delay equal to $\Delta T \approx 14\,ms$ for our set of parameters. This is due to the effect of the exponential decay adaptive effect that we took into account according to Eq. (3.3.0.1).

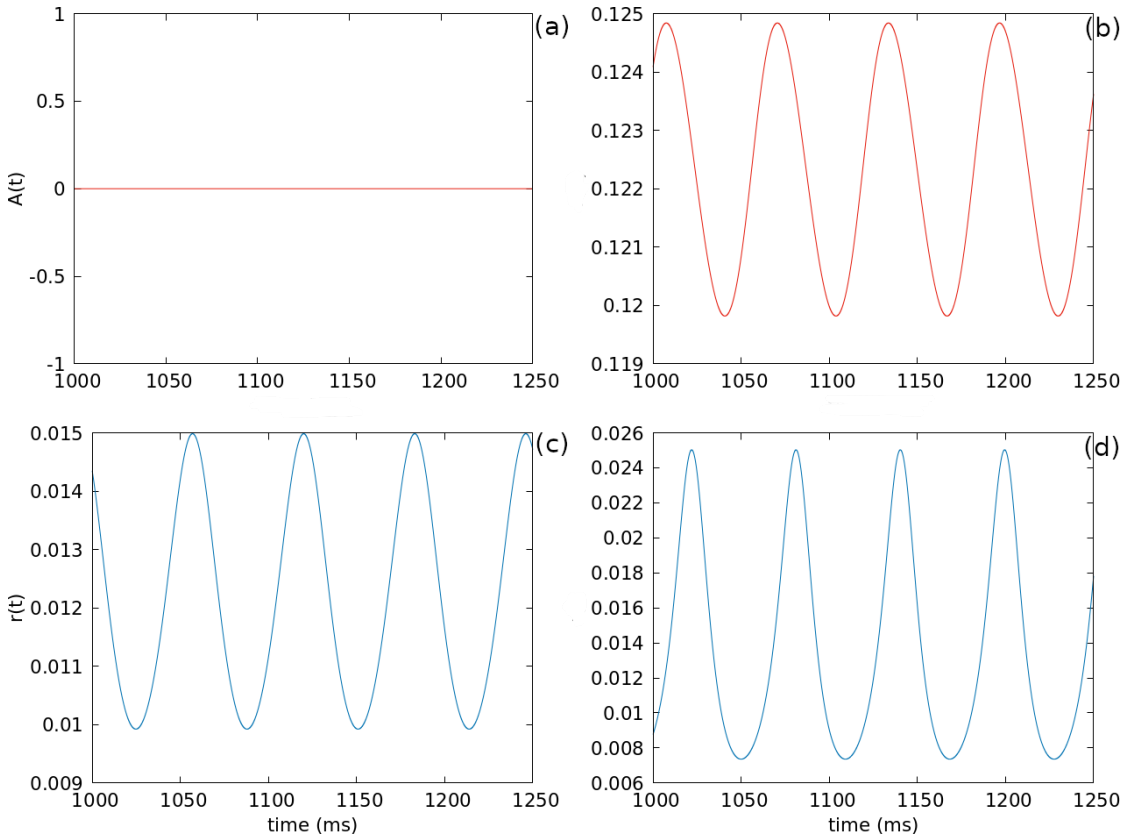

Figure 3.3.4: Simulations of the dynamics for a neural mass QIF model with adaptation. Chosen parameters are $\eta = 1; \Delta = 0.12; \tau = 10ms; \tau_a = 100ms$. (a) A(t) for $\alpha = 0$; (b) A(t) for $\alpha = 10$; (c) r(t) for $\alpha = 0$; (d) r(t) for $\alpha = 10$

In short, we have found that a moderate adaptation effects does not inhibit self-sustained oscillations in a neural mass model of QIF neurons and that, as expected, the adaptation process increases the period between two subsequent spikes.

Chapter 4

Two coupled Populations with exponentially decaying synapses

In this chapter we use the approach explained in the previous sections to study a dynamical system made up by two inhibitory populations of QIF neurons with exponentially decaying synapses. In Section 4.1 we briefly present the model we are going to study, while in Section 4.2 we specifically focus our attention on the network circuit shown Fig. 4.2.1, which describes two vIRT sub-populations, vIRTp and vIRTr, firing respectively in occurrence of vibrissae protraction and retraction. We report the results we have obtained by showing the main dynamical features of the system.

Finally, in Section 4.3 we apply a sinusoidal forcing to one of the two populations in order to explore the induced effect on both populations. The forcing represents the unidirectional inhibitory connection of the *Pre-Botzinger Complex* (as shown in Fig. 4.3.1) applied only to the vIRTr sub-population.

4.1. Two populations reduced model

We denote with 1 and 2 two populations made up by, respectively, N_1 and N_2 QIF neurons. Population 1 is therefore described by the single neurons' membrane potentials $V_i^{(1)}$ and by the mean synaptic activation field S_1 while analogously population 2 is described the membrane potentials $V_j^{(2)}$ and by the mean synaptic activation field S_2. Being $t_1^{(1)}, ..., t_{M_1^{(1)}}$ and $t_1^{(2)}, ..., t_{M_1}^{(2)}$ the times at which any neuron of population 1 or population 2 fires a pulse, then we can describe

the evolution of two QIF networks, coupled with exponentially decaying synapses, with the following system of $N_1 + N_2 + 2$ differential equations.

$$\begin{aligned}
&\dot{V}_i^{(1)}(t) = [V_i^{(1)}(t)]^2 + \eta_i^{(1)} + J_{11}S_1(t) + J_{21}S_2(t), \quad i = 1, ..., N_1; \\
&\tau_d^{(1)}\dot{S}_1(t) + S_1(t) = \frac{1}{N_1}\sum_{k=1}^{M_1}\delta(t - t_k^{(1)}); \\
&\dot{V}_j^{(2)}(t) = [V_j^{(1)}(t)]^2 + \eta_j^{(2)} + J_{22}S_2(t) + J_{12}S_1(t), \quad j = 1, ..., N_2; \\
&\tau_d^{(2)}\dot{S}_2(t) + S_2(t) = \frac{1}{N_2}\sum_{k=1}^{M_2}\delta(t - t_k^{(2)});
\end{aligned} \tag{4.1.0.1}$$

Along with the usual reset rule, $\forall\, i \in 1, ...N_j$ if at a fixed time t_f we have that $V_i^j(t_f^-) = +\infty$, then $V_{i,j}^{(l)}(t_f^+) = -\infty$, $l \in 1, 2$, $i, j \in 1, ..., N_{(l)}$

Following the procedure for the model reduction reported in Chapter 2, we can obtain the reduced model in the thermodynamic limit. Assuming the excitability parameters to be distributed according to the following Lorentzian distributions

$$g_1(\eta) = \frac{1}{\pi}\frac{\Delta_1}{(\eta - \bar{\eta}_1)^2 - \Delta_1^2}, \qquad g_2(\eta) = \frac{1}{\pi}\frac{\Delta_2}{(\eta - \bar{\eta}_2)^2 - \Delta_2^2} \tag{4.1.0.2}$$

where $\bar{\eta}_1$, $\bar{\eta}_2$ and Δ_1, Δ_2 are, respectively, the median excitability parameters and the heterogeneity parameters of population 1 and 2.

This dynamical system can be exactly described at a macroscopic level in the limit of infinite neurons with the six following ordinary differential equations:

$$\begin{aligned}
\tau_1\dot{r}_1 &= \frac{\Delta_1}{\tau_1\pi} + 2r_1v_1 \\
\tau_1\dot{v}_1 &= v_1^2 + \eta_1 - (\pi\tau_1 r_1)^2 + J_{11}s_1\tau_1 + J_{21}s_2\tau_1 \\
\tau_{d_1}\dot{s}_1 &= -s_1 + r_1 \\
\tau_2\dot{r}_2 &= \frac{\Delta_2}{\tau_2\pi} + 2r_2v_2 \\
\tau_2\dot{v}_2 &= v_2^2 + \eta_2 - (\pi\tau_2 r_2)^2 + J_{22}s_2\tau_2 + J_{12}s_1\tau_2 \\
\tau_{d_2}\dot{s}_2 &= -s_2 + r_2
\end{aligned} \tag{4.1.0.3}$$

We observe that the coupling between the two populations is entirely represented by the additive terms $J_{12}s_1$ and $J_{21}s_2$ so that it directly affects the time evolution of the membrane potential. However, since the membrane potentials appear in the firing rate evolution, all the coordinates of both populations are affected.

In conditions of regular firing regime, since the coupling term depends on the synaptic activation field, the inhibitory or excitatory regulation gets stronger when the influencing population has a higher activity (with a delay induced by the exponentially decaying synapses).

Since there is good agreement between the time evolution of the system described in Eq. (4.1.0.1) and the reduced model defined in Eq. (4.1.0.3) [11], we can proceed with our subsequent study by focusing on the reduced system, which is easier to approach from a computational and analytical point of view.
We start with a general analysis of fixed points for our system.

Fixed points

We know that for a fixed point $\dot{s}_1 = \dot{s}_2 = \dot{r}_1 = \dot{r}_2 = 0$. This immediately leaves us with:

$$\begin{aligned} s_1 = r_1 &= -\frac{\Delta_1}{2\pi v_1} \\ s_2 = r_2 &= -\frac{\Delta_2}{2\pi v_2}, \end{aligned} \tag{4.1.0.4}$$

which, substituted into Eq. (4.1.0.3), provide us with the following non-linear system in the variable v_1, v_2:

$$v_1^2 + \bar{\eta}_1 - \frac{\Delta_1 J_{11}}{2\pi}\frac{1}{v_1} - \frac{\Delta_1^2}{4}\frac{1}{v_1^2} - \frac{\Delta_2 J_{21}}{2\pi}\frac{1}{v_2} = 0, \tag{4.1.0.5}$$

$$v_2^2 + \bar{\eta}_2 - \frac{\Delta_2 J_{22}}{2\pi}\frac{1}{v_2} - \frac{\Delta_2^2}{4}\frac{1}{v_2^2} - \frac{\Delta_1 J_{12}}{2\pi}\frac{1}{v_1} = 0. \tag{4.1.0.6}$$

The solutions of this algebraic system are the projections of fixed points on the space defined by v_1 and v_2. Having these two coordinates allows us to obtain the values of the firing rate and of the synaptic activation field through Eq. (4.1.0.4). We should now study the linear stability of fixed points P*=$(r_1^*, v_1^*, s_1^*, r_2^*, v_2^*, s_2^*)$ by explicit calculation of the linearized spectrum of the system around the fixed point. The characteristic polynomial obtained from the linearized system, however, is too complicated to be treated analytically. Therefore, as we already did for the single population network with adaptability, we proceed by exploring the system dynamics and features through MATCONT and through numerical simulations. Before doing so, however, we introduce some additional conditions on the system parameters, in agreement with biological features of the neuron populations we wish to study in this thesis.

4.2. Identical interacting inhibitory populations

As we introduced in Section 1.10, our goal is to investigate the mechanism underlying whisking rhythm generation and to explain how the whisking rhythm is shaped by the breathing rhythm, according to the full circuit model represented in Fig. 1.10.1. As a first step towards this goal, we study a network made up by two identical populations of inhibitory neurons, which represents the two interacting sub-populations of the vIRt synaptic architecture, responsible for the premotor whisking activity.

The circuit we analyze is shown on Fig. 4.2.1. In Section 4.3 we introduce an external forcing representing the PreBötc input on the vIRt [17] while in Chapter 5 we include adaptation processes on the vIRt subpopulations as well. Having two identical populations means that $\eta = \bar{\eta_1} = \bar{\eta_2}$, $\Delta = \Delta_1 = \Delta_2$, $J_{self} = J_{11} = J_{22}$, $\tau = \tau_1 = \tau_2$ $\tau_d = \tau_d^1 = \tau_d^2$. It also implies that both populations influence each other with the same inhibitory synaptic weight J_{cross}. These assumptions make our analysis easier as there are fewer parameters that we have to vary which could induce bifurcation phenomena. Both populations have inhibitory feedback as well, thus $J_{self} < 0$.

With these assumptions the system now becomes

$$
\begin{aligned}
\tau \dot{r}_1 &= \frac{\Delta}{\tau\pi} + 2r_1v_1 \\
\tau \dot{v}_1 &= v_1^2 + \eta - (\pi\tau r_1)^2 + J_{self}s_1 + J_{cross}s_2 \\
\tau_d \dot{s}_1 &= -s_1 + r_1 \\
\tau \dot{r}_2 &= \frac{\Delta}{\tau\pi} + 2r_2v_2 \\
\tau \dot{v}_2 &= v_2^2 + \eta - (\pi\tau r_2)^2 + J_{self}s_2 + J_{cross}s_1 \\
\tau_d \dot{s}_2 &= -s_2 + r_2
\end{aligned}
\tag{4.2.0.1}
$$

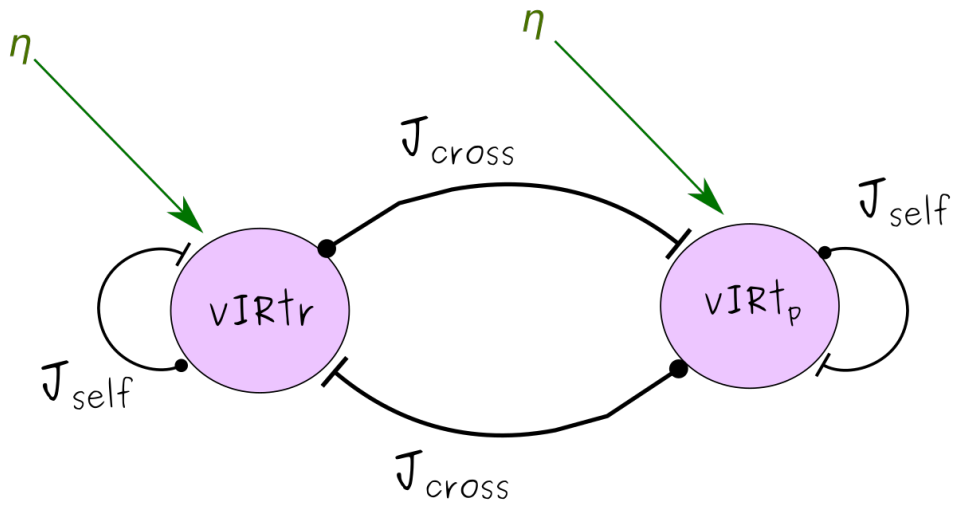

Figure 4.2.1: Circuit model of the system described in Eq. (4.2.0.1). The two vIRt sub-populations will be represented by two identical interacting and inhibitory networks of QIF neurons. vIRTr and vIRTp respectively spike in correspondence of vibrissae retraction and protraction. J_{self} represents the self-interaction of both populations, J_{cross} is the mutual interaction between the two populations and η is a parameter which takes into account both the internal excitability of the network and the average value of the external current.

In this configuration our system of differential equations has six distinct parameters. An exhaustive study of all the possible dynamical behaviours is beyond the scope of this thesis, thus we keep some of our parameters constant at biologically reasonable values and we vary the other ones. In particular, we assume that

$$\Delta = 0.5 \qquad \tau = 10\,ms \qquad \tau_d = 20\,ms \tag{4.2.0.2}$$

and we analyze the macroscopic network evolution in the planes (J_{cross}, J_{self}), (η, J_{self}) and (η, J_{cross}).

Since our goal is to discover which dynamical behaviour the system can express, we are interested in discovering which bifurcation processes the system can go through. We will use two different approaches:

- The first one is an explorative procedure through MATCONT. We can start by simulating the time evolution of the system for a chosen set of parameters which guarantees a fixed point evolution. Then, given this stable fixed point, we vary a single parameter and we calculate the eigenvalues, checking if some of the bifurcations conditions are met. A

bifurcation found in this way is known as *codim* 1 bifurcation. Then, starting from the bifurcation value, MATCONT allows us to calculate how this bifurcation point changes while simultaneously varying two parameters. This process can lead us to find a *codim* 2 bifurcations, i.e. a qualitative change of the dynamical behaviour which occurs through variation of two distinct parameters.

- The second approach is suggested by [58]. We observe that the macroscopic system defined in Eq. (4.2.0.1) possesses permutational symmetry: it is invariant under the change of variables $(r_1, v_1, r_2\, v_2) \longrightarrow (r_2, v_2, r_1, v_1)$. This symmetry admits the existence of the symmetric solutions $(r_1, v_1) = (r_2, v_2)$. As explained in detail in Appendix B, we can analyze the stability of such solutions by numerically computing the eigenvalues related to transverse symmetry and longitudinal symmetry. Transverse symmetry is present when both populations are synchronized. When transverse symmetry is broken (i.e. the stability is lost) the two populations express different dynamical behaviour. Instead, longitudinal symmetry is present when the solution is a fixed point, and it is broken when the fixed point solution loses stability (i.e. oscillatory behaviour). We will see that the two procedures will lead us to the same results as far as the dynamical behaviour of the system is concerned.

In general, our system exhibits a notable range of different dynamics, even though we are studying the inhibitory case. In each of the three planes there is at least one region with a regular oscillation regime outlined by a Hopf bifurcation. We will also find codim 2 bifurcations thus leading to interesting phenomena such as symmetry breaking and hysteresis.

4.2.1. Phase plane (η, J_{cross})

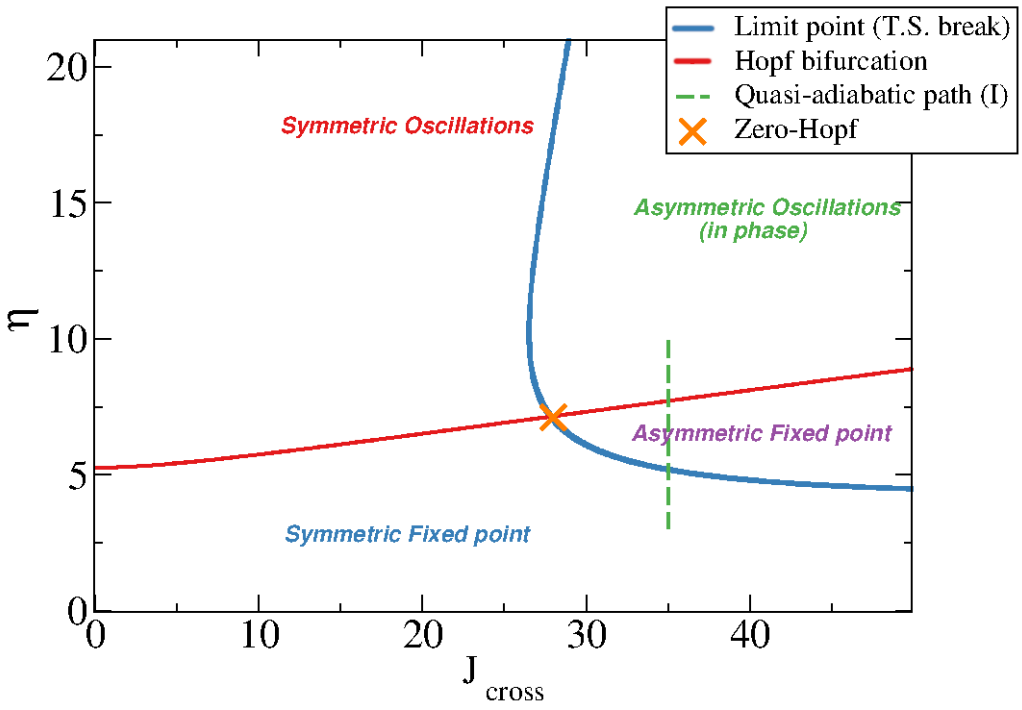

Figure 4.2.2: Parameter plane (η, J_{cross}) for the system described in Eq. (4.2.0.1). Red curve: Hopf bifurcation/longitudinal symmetry broken. Blue curve: Limit point curve/transverse symmetry broken. Green dashed line: adiabatic path followed in Fig. 4.2.4. Orange cross: Zero-hopf point as the intersection between the two bifurcation curves. $J_{self} = 21$ is held constant throughout this analysis.

In Fig. 4.2.2 we see the parameters' plane (η, J_{cross}). As discussed before, in order to study the behaviour of the system we studied the transverse and the longitudinal stability of fixed points and we found two different codim 1 bifurcations: a Hopf bifurcation and a limit point bifurcation. We followed the stability of these two bifurcations, thus obtaining the red and the blue curve represented in the plot. These two curves have a very important dynamical meaning as they divide the parameter plane according to the dynamical behaviour: The Hopf bifurcation separates oscillating solutions from non-oscillating ones (which implies a breaking of

the longitudinal symmetry). In practice, when we cross the red curve while increasing η, we pass from a fixed point solution (identical for both populations) to a synchronous, identical oscillating regime. We see an example of this in Fig. 4.2.3 (a) and (c).

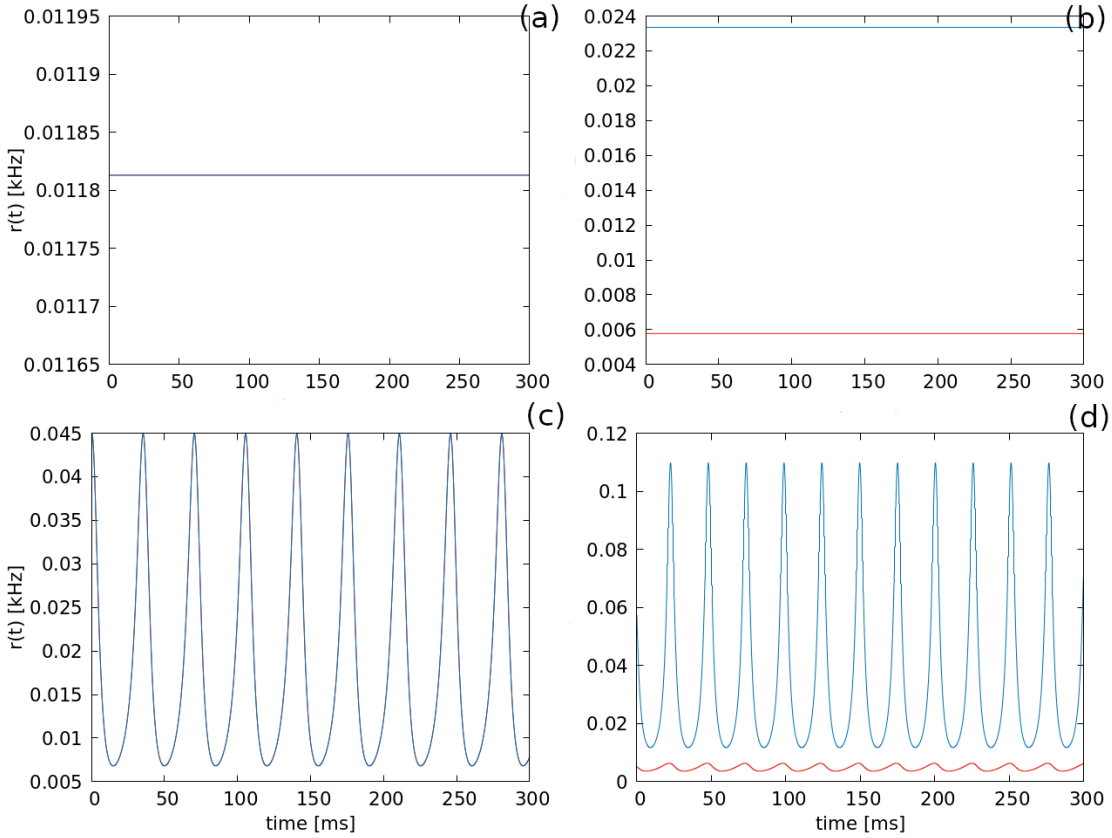

Figure 4.2.3: Simulation of the system presented in Eq. (4.2.0.1). Blue line and red line respectively represent the dynamical behaviour of populations 1 and 2. (a) symmetric fixed point, $J_{cross} = 25, \eta = 5, J_{self} = 20$. (b) asymmetric fixed point, $J_{cross} = 33, \eta = 7, J_{self} = 20$. (c) symmetric collective oscillations, $J_{cross} = 25, \eta = 10, J_{self} = 20$. (d) asymmetric collective oscillations, $J_{cross} = 33, \eta = 10, J_{self} = 20$.

The limit point curve, instead, represents the boundary of the region inside which the two populations have a different time evolution. This behaviour is quite remarkable as we observe that two identical interacting systems can have different regime solutions despite the permutational symmetry. Furthermore, this phenomenon happens even with identical initial conditions, after a transient period of time. In our system we observe two different ways in which this may happen. When we are inside the limit point curve but we are outside of the oscillating Hopf region (i.e.

we haven't crossed the red line) the dynamics is characterized by an asymmetric fixed point. This means that both populations converge to constant values of their coordinates, however $(r_1, v_1, s_1) \neq (r_2, v_2, s_2)$. This is shown in Fig. 4.2.3 (b).

From a mathematical point of view, the Hopf bifurcation curve marks the point in which the real part of two eigenvalues change sign simultaneously. When this happens and the real parts are positive, then the solution is no longer stable and the system starts oscillating. At the same time, one of the three eigenvalues related to longitudinal stability crosses the imaginary axis, this means that the real part of one of the eigenvalues changes sign. The limit point curve has an analogous meaning, but it is related to the transverse symmetry, which is broken when the line is crossed.

In this specific plane we observe yet another interesting behaviour. For high enough values of η and J_{cross}, we find that the time evolution is both oscillating and asymmetrical. In particular, we find that both populations oscillate in phase but the amplitudes, the shapes and the mean values are different. A time trace of this behaviour is shown in Fig. 4.2.3 (d).

The bifurcations we have found effectively represent dynamical transitions. We want to investigate whether these transitions can exhibit hysteretic behaviour.

In general, hysteresis is the dependence of the state of a system on its history (e.g. dependance on initial conditions). In our case, since the transition sets apart two distinct dynamical regimes, having hysteresis would imply the existence of a bistability region near the bifurcation curve.

We have two ways to look into this phenomenon. As explained in Appendix A a Hopf bifurcation can be sub-critical (or super-critical) if it expresses (or if it does not) hysteresis. Given a certain Hopf bifurcation point, MATCONT is capable of detecting this feature by computing the so-called first Lyapunov coefficient. Should this parameter be positive (negative), then the bifurcation would be sub-critical (super-critical). This implies the existence of an unstable limit cycle before the bifurcation occurs, thus giving raise to hysteretical dynamical transition.

However, in the range of parameters that we have explored, the first Lyapunov coefficient is negative at every point on the Hopf bifurcation reported in Fig. 4.2.2. This suggests that we have no hope of finding hysteretic behaviour in this case.

As a further proof of this we can directly study the time evolution of the system near the transition. Starting from a certain point of the parameter plane not too close to the bifurcation with a certain set of initial condition, we simulate the time evolution of the system for a certain time period (which includes a transient time for the system convergence to an equilibrium state plus an observation time period). Afterwards, we slightly increase the bifurcation parameter

λ by a small amount $d\lambda$ such that $\lambda^{new} = \lambda^{old} + d\lambda$. We start a new simulation setting the final values of the previous simulation as the initial conditions. Then, for each value of the parameter, we compute the maxima and the minima of the coordinates so that we can clearly understand where the dynamical transition occur, since each dynamical behaviours exhibits its own amplitude (defined as difference between the maxima and the minima of the dynamics). As an example, for a fixed point, maximum and minimum is the same for a fixed parameter value, while for an oscillating behaviour we observe $maximum \neq minimum$. After crossing the transition, we repeat this process along the opposite direction (by decreasing the bifurcation parameter) to see wether or not there is a hysteretic region near the transition, i.e. a region in which two distinct dynamical behaviours can be obtained by means of different initial conditions.

An example of this process can be seen in Fig. 4.2.4

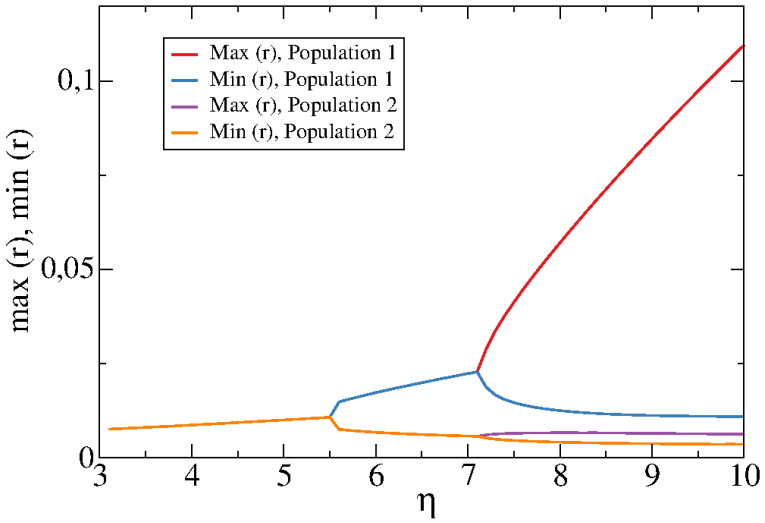

Figure 4.2.4: Quasi-adiabatic path obtained for $J_{cross} = 25, J_{self} = 21$. For each value of η (abscissa) we explicitly report the maxima and the minima of the time trace of the firing rate (ordinate). The path is then followed on both directions (increasing η and decreasing η) to investigate the hysteretic processes.

In figure Fig. 4.2.4 we see the plot of the maxima and the minima of the firing rate as measured for different values of η. The path followed is shown in Fig. 4.2.2 as a dashed line. For $\eta \lesssim 5.5$ we see that max(r) and min(r) are identical and equal for both population. By increasing

η we cross the limit point curve, thus triggering the asymmetric fixed point. Here, max(r) and min(r) are the same but they differ for the two populations. For $\eta \gtrsim 7$, passing through the Hopf bifurcation implies that the symmetric fixed point loses its stability and each population starts oscillating. In this case there are no evident signs of hysteresis, thus confirming the negative value of the first Lyapunov coefficient of the Hopf bifurcation.

4.2.2. Phase plane (J_{self}, J_{cross})

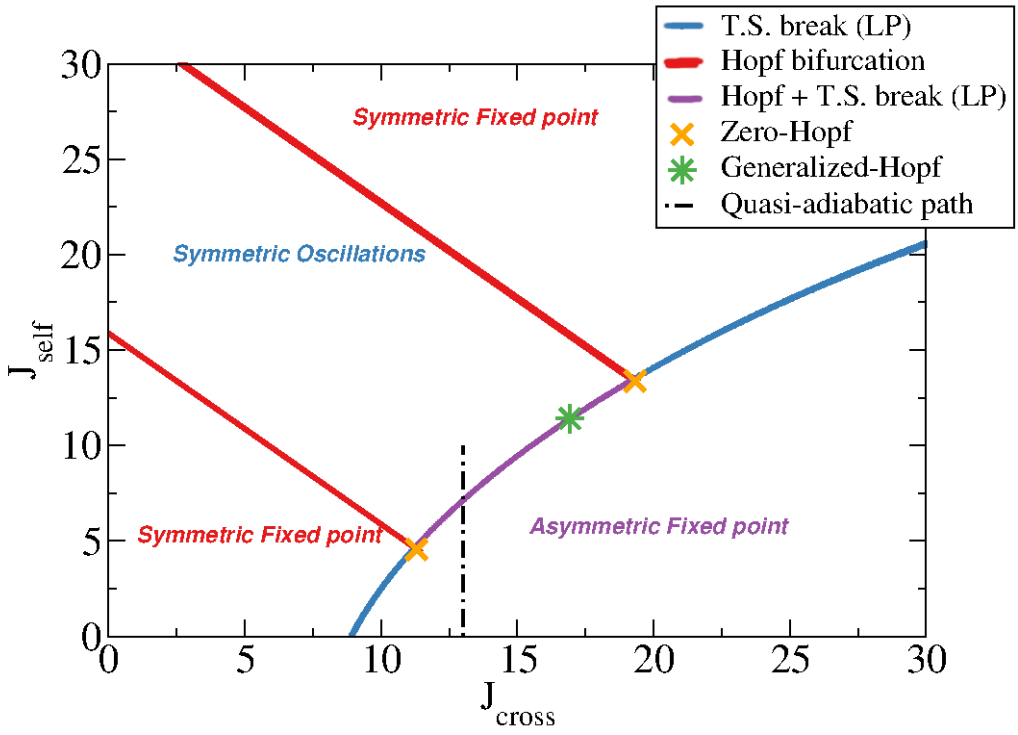

Figure 4.2.5: Parameters plane (J_{cross}, J_{self}) for the system described in Eq. (4.2.0.1). Red curve: Hopf bifurcation/longitudinal symmetry broken. Blue curve: Limit point curve/transverse symmetry broken. Black dashed line: adiabatic path followed in Fig. 4.2.6. Purple curve: overlapping of Hopf bifurcation and transverse symmetry broken. Orange cross: Zero-hopf point as the intersection between the two bifurcation curves. Green star: Generalized Hopf point separating hysteretical and non-hysteretical transition between asymmetric fixed point and collective oscillations. $\eta = 5.87$ is held constant throughout this analysis.

In this parameter plane we have slightly different phenomena from the previously studied cases. Once again we find a region inside which the system symmetrically oscillates (with a time-trace similar to Fig. 4.2.3 (c)), however such region is contoured by two different Hopf bifurcations instead of just one. Both of them are super-critical, meaning that no hysteresis is observed. Outside of this region, on the upper and on the lower side of the plane we have a single stable fixed point. Moving to higher J_{cross} on the right we see a transverse symmetry breaking curve, which limits the area where the two populations have a different time evolution. The peculiar feature lies at the boundary between the oscillating region and the asymmetric fixed point region, where we observe a hopf bifurcation overlapped with a limit point curve.

Along the Hopf curve we also find a new codim 2 bifurcation point, known as *Generalized Hopf* point. This point occurs when the first Lyapunov coefficient related to the Hopf bifurcation changes sign. In our specific case, this means that for lower values of J_{self} the transition is hysteretical. In order to prove this, we follow the dynamics along the quasi-adiabatic path shown in Fig. 4.2.5: The results are reported in Fig. 4.2.6.

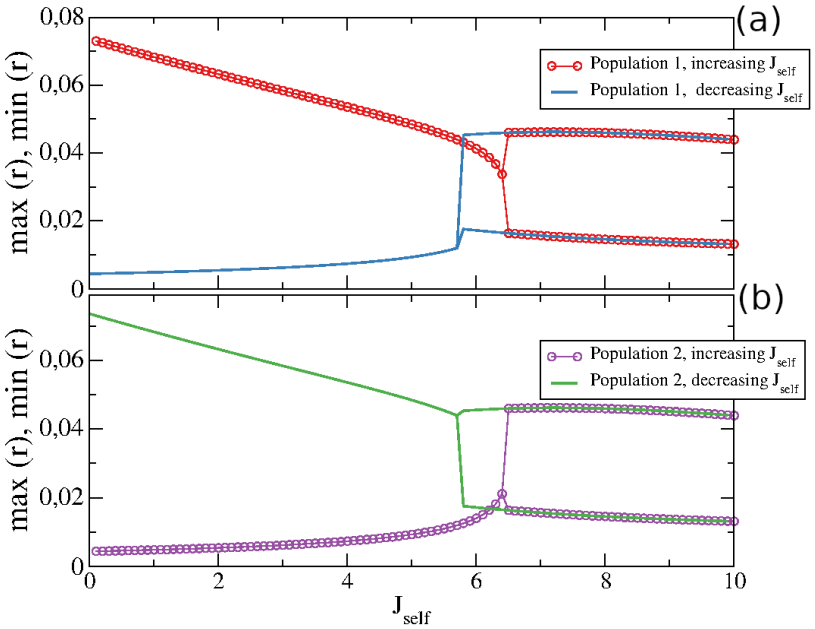

Figure 4.2.6: Quasi-adiabatic path obtained for $J_{cross} = 12.5, \eta = 5.87$. For each value of J_{self} (abscissa) we explicitly report the maxima and the minima of the time trace of the firing rate (ordinate) for population 1 (a) and population 2 (b). The path is followed on both directions (increasing J_{self} and decreasing J_{self}) to investigate hysteretic processes.

In Fig. 4.2.6 we see that there exists a bistability region where, with proper initial conditions, the system can exhibit two different dynamical behaviours.

In addition to that, the two populations "exchange" the fixed point to which they evolve to, according to the direction of the path. Since the permutational symmetry still holds, we can conclude that this happens due to the different initial conditions which may result in a different, yet equivalent, fixed point configuration.

4.2.3. Phase plane (η, J_{self})

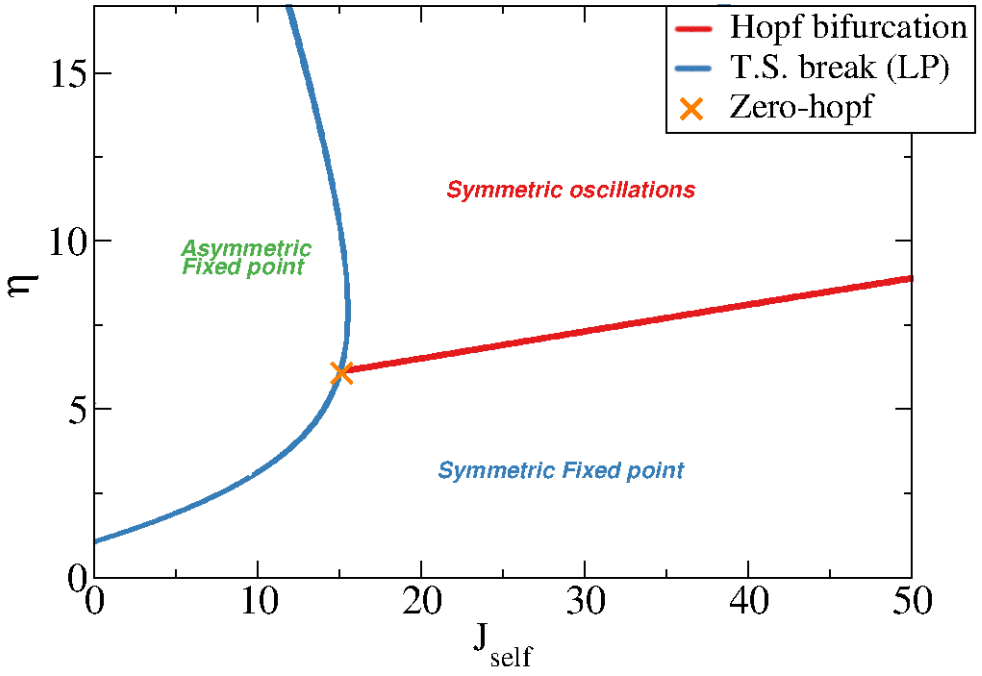

Figure 4.2.7: Parameters plane (η, J_{cross}) for the system described in Eq. (4.2.0.1). Red curve: Hopf bifurcation/longitudinal symmetry broken. Blue curve: Limit point curve/transverse symmetry broken. Purple cross: Zero-Hopf point as the intersection between the two bifurcation curves. $J_{cross} = 21$ is held constant throughout this plane analysis.

In the (η, J_{self}) plane we find once again a Hopf bifurcation which defines the boundaries of the region where the system oscillates and a limit point curve inside which the fixed point splits

for the two populations. The time evolution for the various regimes is similar to those shown in Fig. 4.2.3, but we see an interesting difference; the Hopf bifurcation ends abruptly in the Zero-Hopf point. Actually, through MATCONT we are able to extend the curve even inside the region with broken transverse symmetry, however in this case we are following a symmetric fixed point which is no longer stable, thus we have no way of explicitly observing oscillating dynamics.

It is important to remark that all asymmetric behaviours we have observed so far have been obtained with $J_{cross} > J_{self}$. This means that, when considering a real biological system, such as the two vIRt sub-populations, the cross-interaction (i.e. the effect of one population on the other one) needs to be greater than the self-interaction (i.e. the effect of one population on itself). This is not a commonly encountered situation that could be easily justified. This particular condition could occur due to some secondary effects which should be explored in deeper detail.

In conclusion, we have seen that a system with two identical interacting inhibitory populations can show various different dynamical regimes. Despite the fact that both populations are inhibitory, the assumption of tonic neurons still allows the system to show collective oscillations.

Furthermore, we stress that even though we are dealing with two identical populations, we have found asymmetric solutions, as shown in Fig. 4.2.3(b) and (d). However we also note that, although the two populations can have two different spiking regimes, they are still synchronous, such that both populations emit pulses at the same time.

In the next section we will see that, by introducing an asymmetric element (in the form of a forcing inhibitory coupling) the two populations will behave differently, while maintaining a strong interdependence.

4.3. Effects of external current

In this last section we analyze the role played by *pre-Bötzinger complex* (pre-BötC) on the dynamics of our system of two identical interacting inhibitory neuron populations. As discussed in Section 1.10 we aim to investigate the role of the pre-BötC inhibitory input on the whisking rhythm generation. Therefore, with this idea in mind, we study the circuit model represented in Fig. 4.3.1

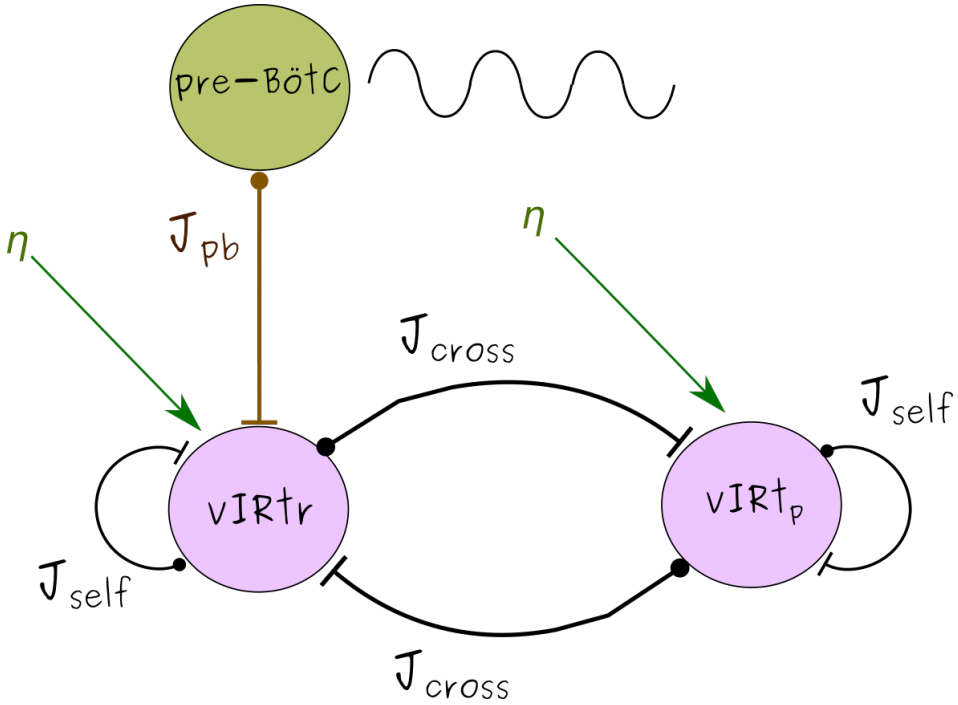

Figure 4.3.1: Circuit model of the system described in Eq. (4.3.0.2). The two vIRt sub-populations will be represented by two identical interacting and inhibitory networks of QIF neurons. Pre-BötC effects on the population related to whiskers retraction are included through a sinusoidal $I_f(t)$. J_{self} represents the self-interaction of both populations, J_{cross} is the mutual interaction between the two populations and J_{PB} is the strength of the inhibition of Pre-BötC on vIRTr. η is a parameter which takes into account both the internal excitability of the network and the average value of the external current and is identical for both populations.

The Pre-BötC is known to have an inhibitory effect on the vIRT [1]. We assume that it acts on the membrane potential time evolution through an additive negative term given by the following time-dependant sinusoidal function

$$I_f(t) = J_{PB}(1 + \sin \omega t) \tag{4.3.0.1}$$

This specific form has the advantage of being quite a simple function and yet it is a good approximation of a coupling term with another inhibitory neuronal population with a constant spiking frequency ω and a coupling strength J_{PB}.

In the following, we study the two inhibitory populations response to this forcing by varying

J_{PB} and ω. However, in order to have a biologically reasonable set of parameters, we must choose the range of variability in an appropriate way. Since the main Pre-BötC activities we are interested into are breathing cycle during basal respiration (characterized by a frequency $<$ 4 Hz) and during sniffing associated with whisking (frequency $>$ 4 Hz until $\approx 12Hz$), we take $\omega \in [1Hz, 12Hz]$. J_{PB} will have approximately the same magnitude of J_{cross} and J_{self}.

With the introduction of forcing terms the system now becomes

$$\begin{aligned}
\tau\dot{r}_1 &= \frac{\Delta}{\tau\pi} + 2r_1v_1 \\
\tau\dot{v}_1 &= v_1^2 + \eta - (\pi\tau r_1)^2 + J_{self}s_1\tau + J_{cross}s_2\tau + I_f(t) \\
\tau_d\dot{s}_1 &= -s_1 + r_1 \\
\tau\dot{r}_2 &= \frac{\Delta}{\tau\pi} + 2r_2v_2 \\
\tau\dot{v}_2 &= v_2^2 + \eta - (\pi\tau r_2)^2 + J_{self}s_2\tau + J_{cross}s_1\tau \\
\tau_d\dot{s}_2 &= -s_2 + r_2
\end{aligned} \tag{4.3.0.2}$$

Thus breaking the permutational symmetry of the system.

Due to this relatively high amplitude oscillating term, we expect to find that the forced population will be entrained by the external forcing, producing dynamics with the same external frequency ω, at least in some cases.

Furthermore, we are interested in the forcing effects on the vIRT sub-population which is not directly subject to the forcing itself. In order to do this, we can compare the firing activity of the two populations, looking for situations in which one population of neurons is synchronized to the other one in a specific way (for example, when there is a fixed ratio between the average firing frequency of the two populations). We refer to this phenomenon as $phase - locking$.

In general terms, phase-locking between two (or more) dynamical system components occurs when there is a fixed statistical phase difference distribution between the components of the aforementioned system. In neuroscience, Phase locking usually refers to the tendency of a neuron (or a population of neurons) to fire action potentials at particular phases of another ongoing signal. In our case, we will explore both the phase locking between the two population and the phase locking between one of the populations and the forcing current.

As a first example of forced dynamics and phase-locking, a time simulation for a set of parameters such that the unforced dynamics is collectively oscillating is shown in Fig. 4.3.2.

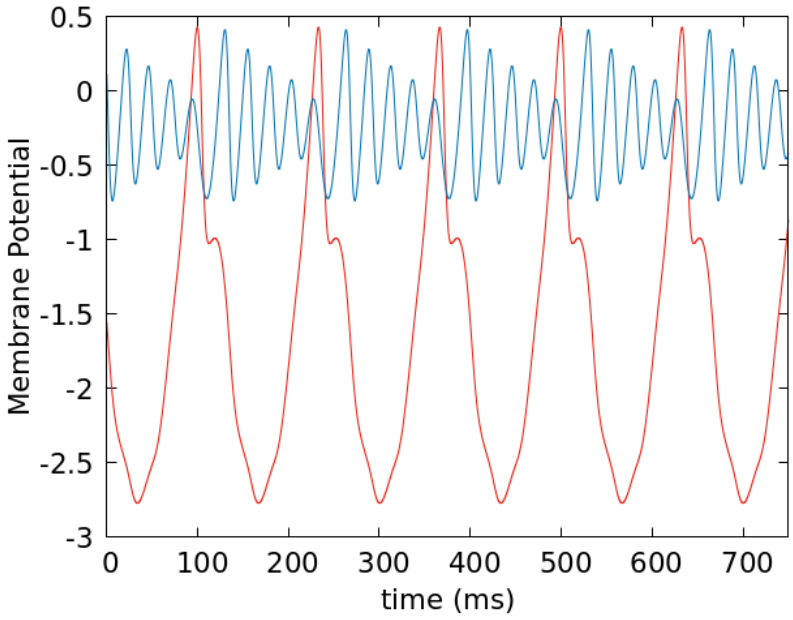

Figure 4.3.2: Simulation of the system presented in Eq. (4.2.0.1). The parameters are $\eta = 5.87, J_{cross} = 10, J_{self} = 10, J_{PB} = 4.5\omega = 7.5Hz$. Red line: forced population. Blue line: unforced population

We see that the two populations have a significantly different behaviour, resulting from the interaction of the "natural" oscillation frequency and amplitude with the forcing parameters J_{PB} and ω. Since we have a wide range of reasonable J_{PB} and ω values, we want to develop a general method that allows us to describe the relative activity of the two sub-populations over a large range of parameters (that is, if there is some fixed relation between the spiking frequency of the two populations).

As a practical example, in the time trace previously presented (Fig. 4.3.2), we see that the evolution of the two populations is periodic, and in particular the period is the same for both populations. However, we observe that for a single period the forced population fires twice while non-forced one fires five times. Since this relation does not change in time, we say that the $phase - locking$ between the two population is $5 : 2$

As a way to detect the phase locking for a given state, we will proceed as follows: first of all, we note that the natural frequency of our system is always greater than the range of frequency of the forcing current. Furthermore, except in the case of asymmetric collective oscillations, the trajectories of both populations have the same period T of the forcing current. Knowing this we

explicitly count the number of maxima of the time trace for both populations over a long period of time Δt and then we divide these two number by the total number of periods elapsed $\Delta t/T$. If Δt is long enough and if the two populations are actually phase locked, we should obtain the phase locking ratio that we are looking for.

In the case of Fig. 4.3.2, for example, this procedure confirms that the phase locking is $5:2$. We stress once again that this means that, for every full oscillation of the forcing current, the forced population fires twice and the non-forced population fires five times.

An equivalent way of doing this is computing the Hilbert Transform of the two signals supposed to be phase locked (see Appendix B for more details.)

Since we previously identified four distinct dynamical behaviour (Fig. 4.2.3) for the unforced system, we proceed by examining how the dynamics change under the forcing term for each one of those regimes. We start by looking explicitly at the time evolution of the coordinates for some values of J_{PB} and ω.

Symmetric fixed point:

The dynamics of a forced fixed point is shown in Fig. 4.3.3

This is the most simple dynamics we can observe: the forced populations oscillates with the same frequency of the forcing current and fires only once per period, thus it is almost entirely driven by $I_f(t)$. However, it's interesting to observe the induced effects on the other population; despite having the same full period of the forcing current, it fires a higher number of times for each forcing oscillations, depending mostly on the forcing frequency ω.

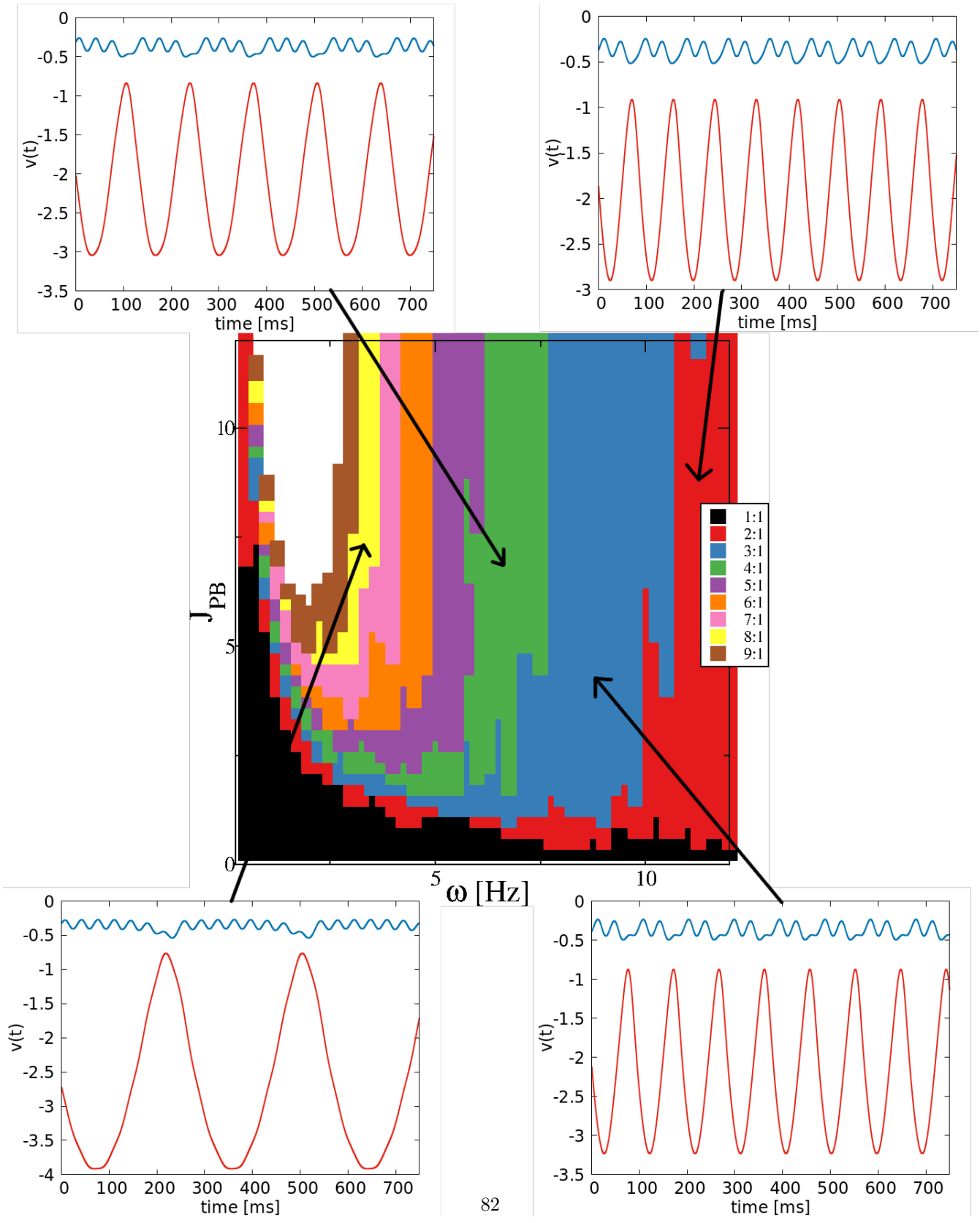

Figure 4.3.3: Phase-locking between forced and non forced population in the parameter plane ($J_{PB,\omega}$). Other parameters are: $\eta = 5.87, J_{cross} = 25, J_{self} = 21$. The white region represent higher or inaccurate values of the phase locking. The four panels are examples of the dynamics in various phase locking regions

in Fig. 4.3.3 we see the parameter plane (ω, J_{PB}) where we represented the phase locking region using the procedure explained before. This plot confirms that the forced population fires only once per forcing oscillation, while the other population has a faster oscillating regime. This is quite remarkable as it means that this population is not directly forced and yet due to the interaction with the forced population it has global spiking events more frequently than the other one. This can be understood in light of the fact that the forcing is inhibitory, thus one can expect that the forced population will tend to be less active than the other one. Moreover, we note that for low J_{PB} values we only observe $1:1$ locking, while for high J_{PB} we can obtain various different lockings such as 2:1 and 3:1. The locking tends to be higher for increasingly lower frequency ω, as we can see in the four panels in Fig. 4.3.3.

Asymmetric fixed point:

When the dynamics is such that the two populations tend to the asymmetric fixed points, we see that the forced population is always the one with lower values of the coordinate. This implies that the effect of the forced population on the other one are smaller than those we have seen in Fig. 4.3.3. In particular, while the frequency of the nested oscillations has the same order of magnitude, their amplitude is far lower, as we can see in Fig. 4.3.4.

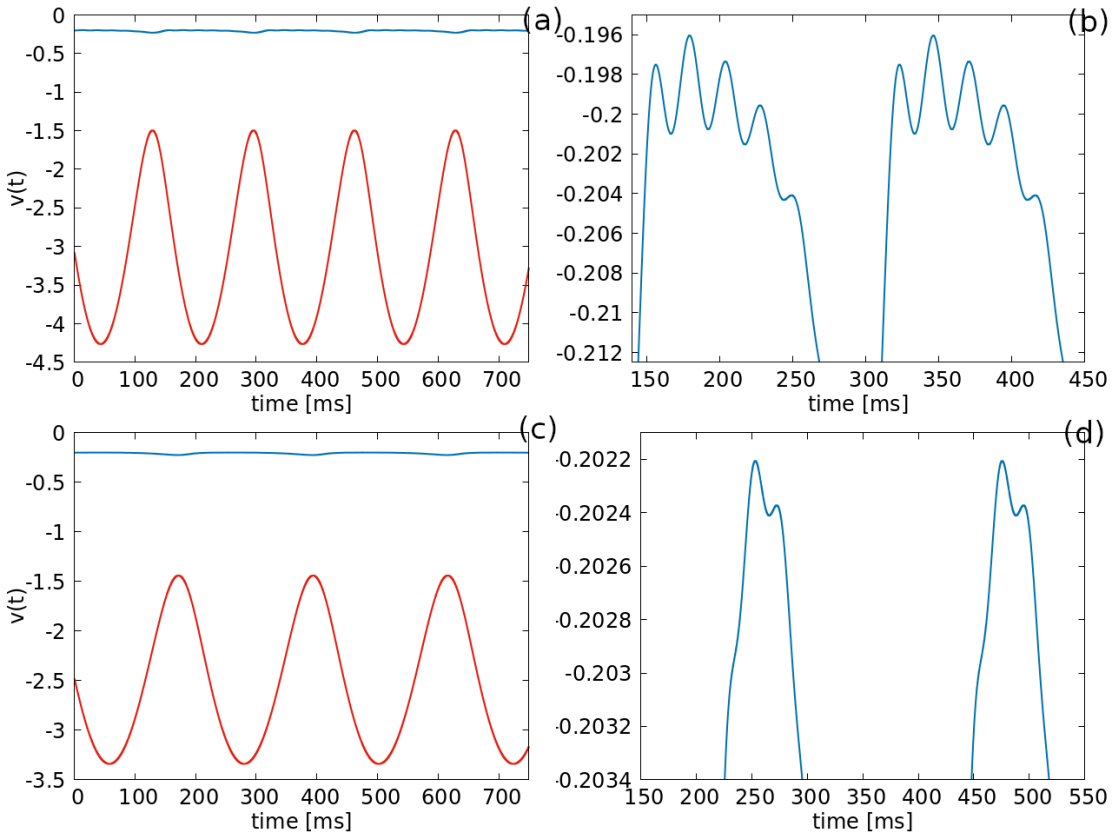

Figure 4.3.4: Simulations of the system presented in Eq. (4.2.0.1). Red line: forced population. Blue line: unforced population. (a) $\eta = 5.87, J_{cross} = 20, J_{self} = 10, J_{PB} = 8\omega = 6Hz$. (b) zoom on the unforced population dynamics shown on panel (a). (c) $\eta = 5.87, J_{cross} = 20, J_{self} = 10, J_{PB} = 4.5\omega = 4.5Hz$. (d) zoom on the non-forced population dynamics shown on panel.

Upon closer inspection, in fact, we see that there are very low-amplitude global activity phenomena induced in the non forced populations. However, these are not always easily detected as local maxima, thus making our analysis more inaccurate than the previously studied regime. However, except in extreme cases, we get a reasonably clear idea of the locking between the two populations, as shown in Fig. 4.3.5.

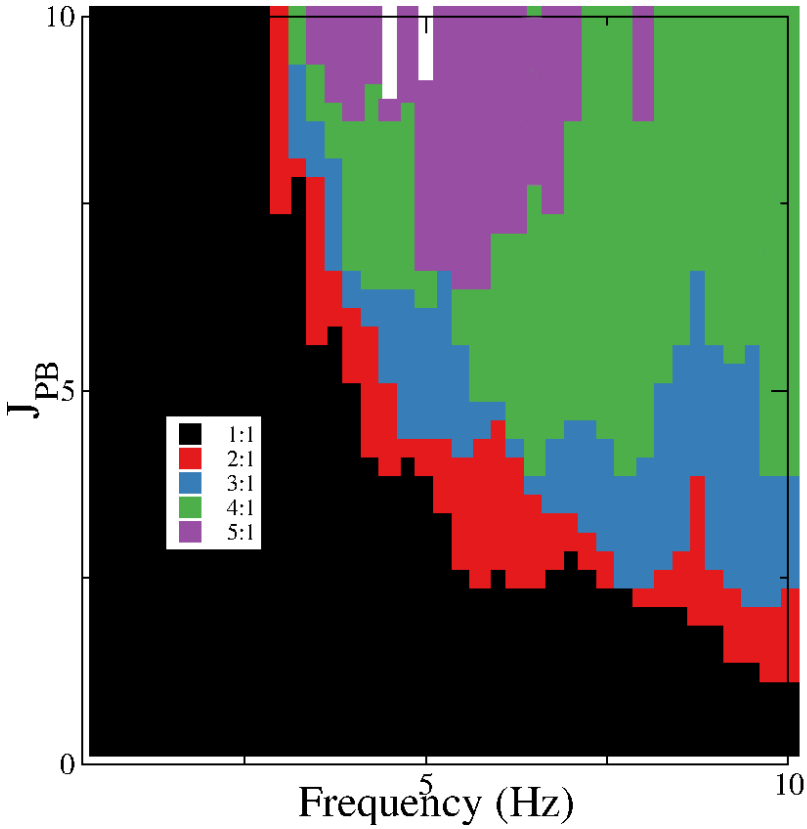

Figure 4.3.5: Phase-locking between forced and non forced population in the parameter plane ($J_{PB,\omega}$). Other parameters are: $\eta = 5.87, J_{cross} = 20, J_{self} = 10$. The white region represents higher or inaccurate values of the phase locking.

Symmetric collective oscillations:

In the case of symmetric collective oscillation, the phase locking obtained is shown in Fig. 4.3.6

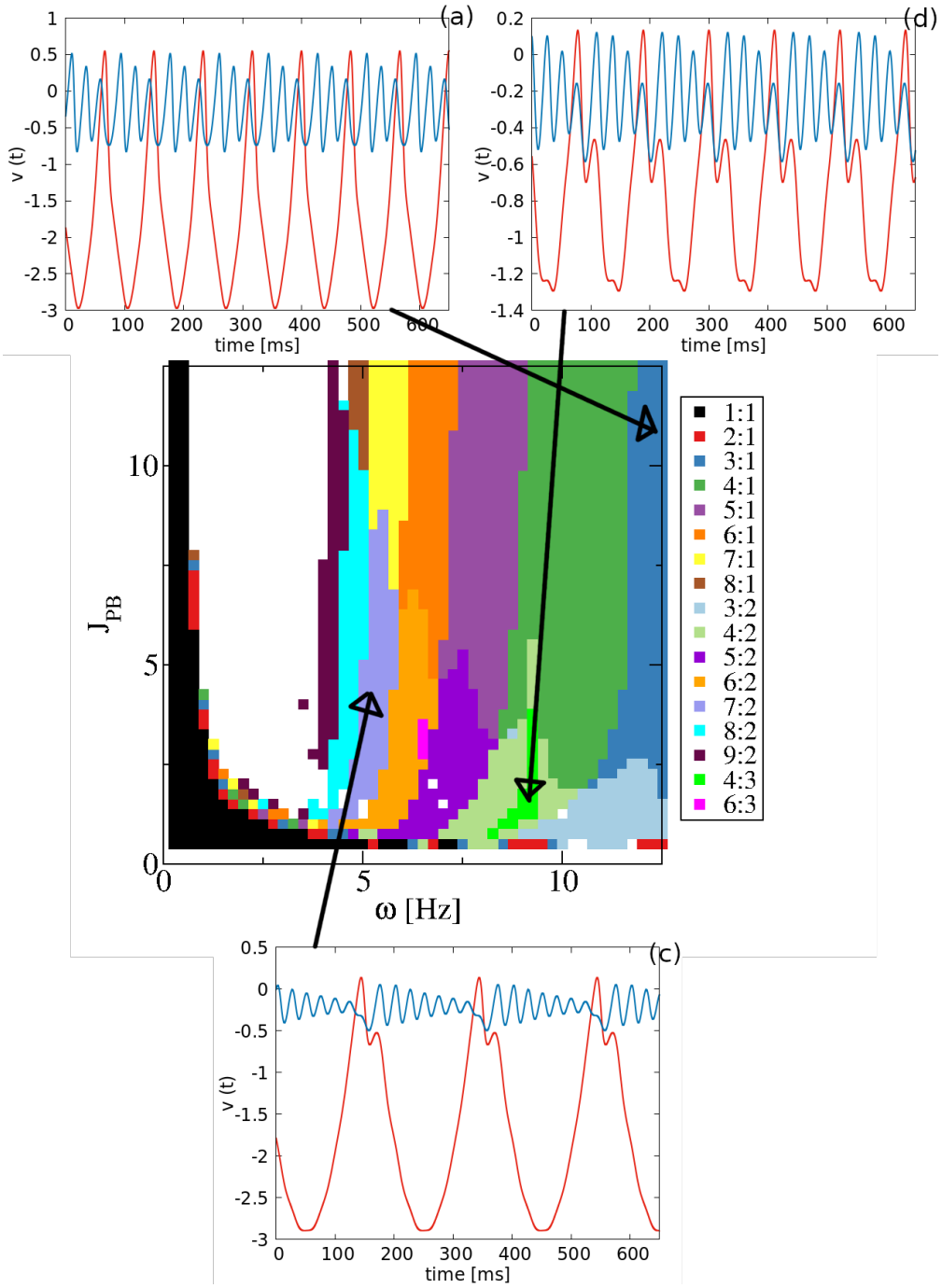

Figure 4.3.6: Phase-locking between forced and non forced population in the parameter plane (J_{PB}, ω). Other parameters are: $\eta = 5.87, J_{cross} = 10, J_{self} = 10$. The white region represent higher values of the phase locking. In the legend, the first and the second number, respectively corresponding to the non forced and to the forced population, refer to how many maxima are detected for an entire period of the forcing. The three panels are examples of the dynamics in various regions

In the previous cases, we have always seen that the forced population is fully entrained with the forcing, thus globally spiking at its same frequency. This might be because in absence of forcing, the dynamics is entirely stable. In this case however, we see that the forced population can fire multiple times for every cycle of the forcing current. This provides us with a regime where the output of the forced population is phase locked with the forcing current itself with a ratio different from 1:1, which could be useful in describing multiple whisking for a single breathing (or even sighing) cycle [17]

Asymmetric collective oscillations:

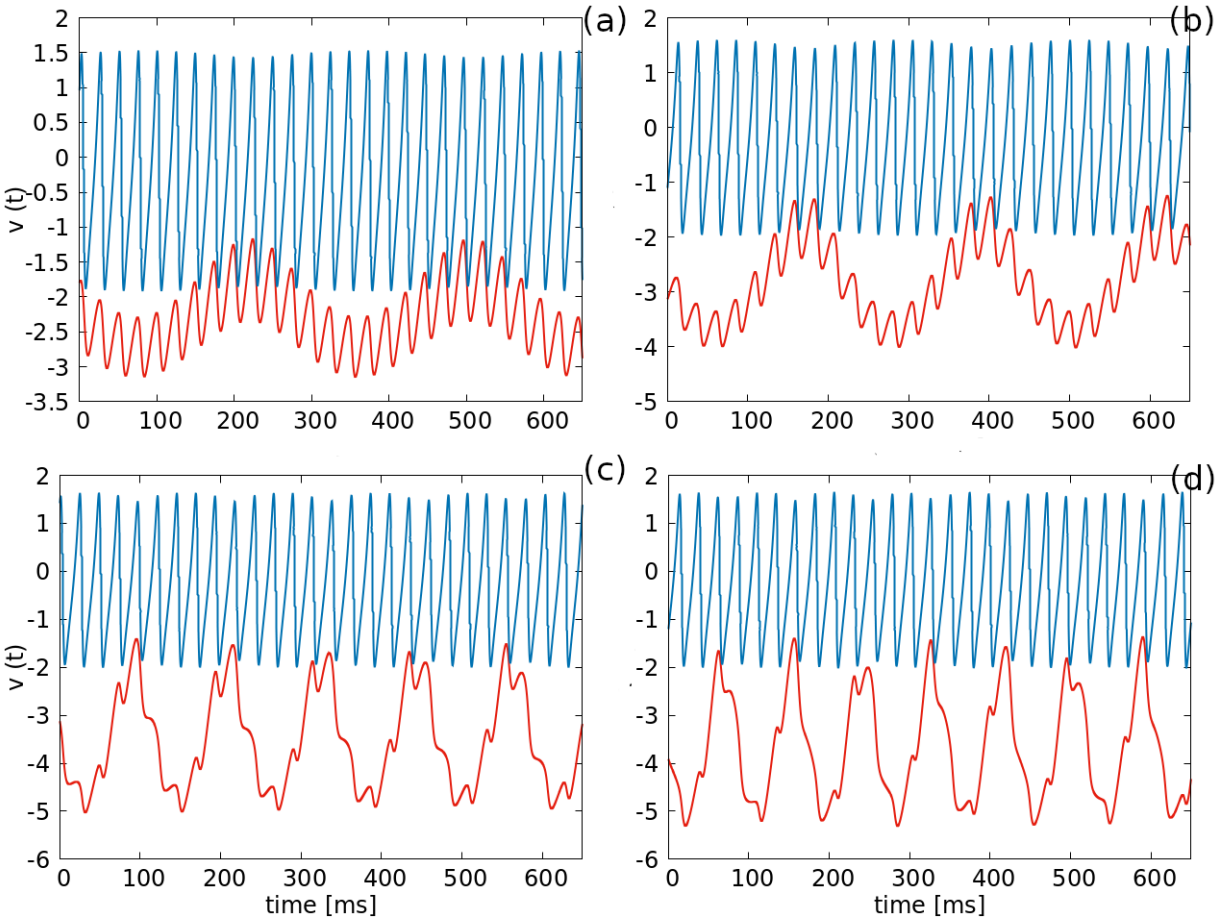

Figure 4.3.7: Simulation of the system presented in Eq. (4.2.0.1). Red line: forced population. Blue line: non-forced population. Parameters are $J_{cross} =, \eta =, J_{self} =$. (a) $J_{PB} = 2, \omega = 3.5$. (b) $J_{PB} = 5, \omega = 4.5$. (c) $J_{PB} = 9.5, \omega = 8.5$. (d) $J_{PB} = 11, \omega = 11.5$.

When the unforced dynamics is given by asymmetric collective oscillations, the effect of the forcing is quite weak on the non-forced population, in which it induces just an amplitude modulation but has no effect on the frequency at all.
The forced population however shows two different behaviours: For low forcing frequencies and coupling, the spiking frequency is the same as the non-forced dynamics (Fig. 4.2.3(d)), while for high coupling (Fig. 4.3.7) some of the nested spikes fail to effectively become local maxima, thus making it impossible for our algorithm to detect them.

In conclusion, we see that the determination of the phase locking has the advantage of giving us an idea about the relation between the global spiking activity of the two populations for a wide range of the parameters J_{PB} and ω. Moreover, being the signals not noisy at all, the maxima detection algorithm works well in most cases. However, the boundaries between two phase locking regions are usually not well defined and there are occasionally some points (J_{PB}, ω) where the computed phase locking is a bit off. As a consequence we have a coarsely-grained parameter plane, especially for low frequencies. This is mostly due to bulges in the time trace of the two populations that cannot be detected as maximum points.

Chapter 5

Two coupled populations with exponentially decaying synapses and adaptation

5.1. System description

In this last chapter we will study a dynamical system made up by two interacting inhibitory populations with exponentially decaying synapses and adaptation.

According to the one population model shown in Chapter 3 and to the prescription for describing interacting neural mass networks already applied in Chapter 4, the system is defined

as follows

$$
\begin{aligned}
\tau \dot{r}_1 &= \frac{\Delta}{\tau\pi} + 2 r_1 v_1 \\
\tau \dot{v}_1 &= v_1^2 + \eta - (\pi \tau r_1)^2 + J_{self} s_1 \tau + J_{cross} s_2 \tau - A_1 \\
\tau_d \dot{s}_1 &= -s_1 + r_1 \\
\tau_a \dot{A}_1 &= -A_1 + \alpha \tau r_1 \\
\tau \dot{r}_2 &= \frac{\Delta}{\tau\pi} + 2 r_2 v_2 \\
\tau \dot{v}_2 &= v_2^2 + \eta - (\pi \tau r_2)^2 + J_{self} s_2 \tau + J_{cross} s_1 \tau - A_2 \\
\tau_d \dot{s}_2 &= -s_2 + r_2 \\
\tau_a \dot{A}_2 &= -A_2 + \alpha \tau r_2
\end{aligned}
\tag{5.1.0.1}
$$

Overall, the system is described by eight first-order differential equations describing the evolution of the eight coordinates of the system. We have four variables for each sub-population, representing the firing rate r_i, the mean membrane potential v_i, the synaptic activation field s_i and adaptation A_i, with $(i = 1, 2)$.

The two populations are formally identical, thus having the same parameters. Being the two populations inhibitory, we will assume $J_{self} < 0$ and $J_{cross} < 0$ (for simplicity, in plots and parameter planes we will use the absolute value of these quantities) while the parameter η, which takes into account both the mean excitability and the mean external current, is positive, meaning that the neurons are tonic.

Overall, with the assumption of identical populations, there are eight distinct parameters. We are going to keep the three time scales and the heterogeneity parameter Δ fixed to the following values

$$
\Delta = 0.5; \quad \tau = 10 \ ms; \quad \tau_d = 20 \ ms; \quad \tau_a = 100 \ ms \tag{5.1.0.2}
$$

as we have already seen that these are biologically reasonable values. In this way we will see how three different physical processes with three distinct time scales interact.

We will vary the other parameters $(\alpha, J_{cross}, J_{self}, \eta)$ to investigate how the dynamical behaviours, that we explored in Chapter 4, change due to the effect of the adaptation.

When considering the macroscopic model for one population (e.g. Section 3.3) we have seen that the main dynamical effect of the adaptation is to reduce the region in the parameter space where collective oscillations appear and increase the time period between two subsequent global

spikes in a constant firing regime. With two populations, adaptive effects will bring forth new stable dynamical regimes.

We are going to explore the system dynamics through MATCONT and, due to the permutational symmetry of the two populations, we can once again study the longitudinal and transverse stability of the identical solutions, as we did in Chapter 4.

We first study the parameter planes (J_{cross}, J_{self}) and (J_{cross}, η), keeping fixed $\alpha = 5$, in order to see the main differences between the two systems. Afterwards, we analyze the dynamics by varying α. In both cases, we will look for the occurring bifurcations in order to clearly define the dynamical transitions that our system undergoes.

5.2. Constant α

5.2.1. Case i: (J_{cross}, J_{self}) plane

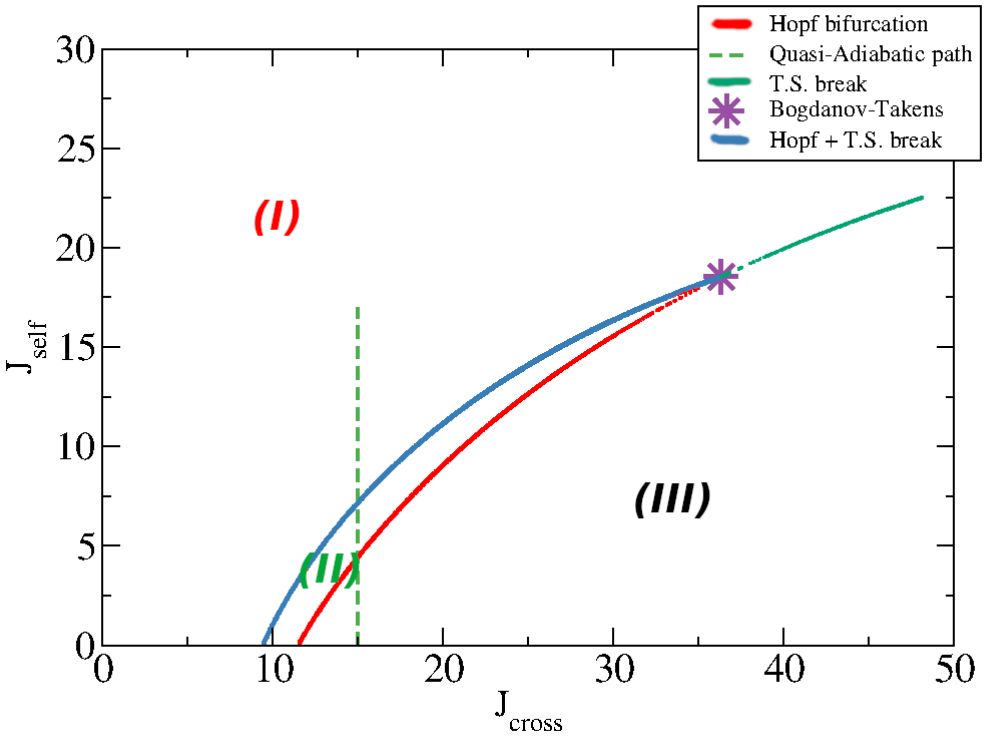

Figure 5.2.1: Phase diagram for the parameter plane (J_{cross}, J_{self}). Light-green curve: T.S. break. Red curve: Hopf bifurcations marking the passage from asymmetric fixed point to asynchronous oscillations. Blue curve: Hopf bifurcation overlapped with a T.S. break curve. Crossing of this curve means passing from symmetric fixed point (where both population have identical evolution and neither of them oscillates) to antiphase oscillations. The observed dynamical regimes are (I): Symmetric fixed point; (II): Antiphase oscillations; (III): Asymmetric Fixed point. Time trace examples are shown in Fig. 5.2.2. Other parameters are $\eta = 5.87$, $\alpha = 5$.

We immediately see some differences with respect to the system without adaptation (Fig. 4.2.5):

- The two Hopf bifurcations have disappeared for the specific value of $\eta = 5.87$ for which we are studying the parameter plane. This makes sense as adaptation reduces the overall

current passing through the neurons, therefore we need a higher excitability η to compensate the newly introduced inhibition. Natural collective oscillations, however, are not completely shut down, as we will soon discover by varying η.

- We observe the emergence of different bifurcations. For high enough J_{cross} we see a similar situation as in the case with no adaptation, i.e. a transverse symmetry break which separates the region with a stable symmetric fixed point from the one with a stable asymmetric fixed point. Following the stability of the T.S. curve until we reach a critical J_{cross} we see that a *Bogdanov Takens* codim 2 bifurcation occurs. This is a peculiar bifurcation which, in this case, marks the parameter plane point where the T.S. breaking curve splits into two distinct Hopf bifurcation curves. Outside of these two curves, the behaviour previously discussed (stable fixed points) holds, while inside the fixed points become unstable, giving birth to a stable limit cycle where the two populations exhibit antiphase oscillations (i.e. one population's maxima are synchronized with the other population's minima). An example of this dynamics is shown in Fig. 5.2.2 (a).

The introduction of the adaptation, characterized by a timescale $\tau_a \gg \tau$, allows us to find asymmetric dynamical solutions, despite the symmetry of the initial system, composed by two identical populations. The asymmetric solution is characterized by antiphase oscillations of the two populations. This antiphase state can be interpreted by saying that when one population is at its peak activity, the other one tends to be silent and viceversa.

Furthermore, we stress once again that the former behaviour only occurs for $J_{cross} > J_{self}$. This means that, according to what we have seen until now, the only observable dynamical regimes for the system presented in Eq. (5.1.0.1), with the additional condition $J_{self} > J_{cross}$, are symmetric collective oscillations and symmetric fixed point.

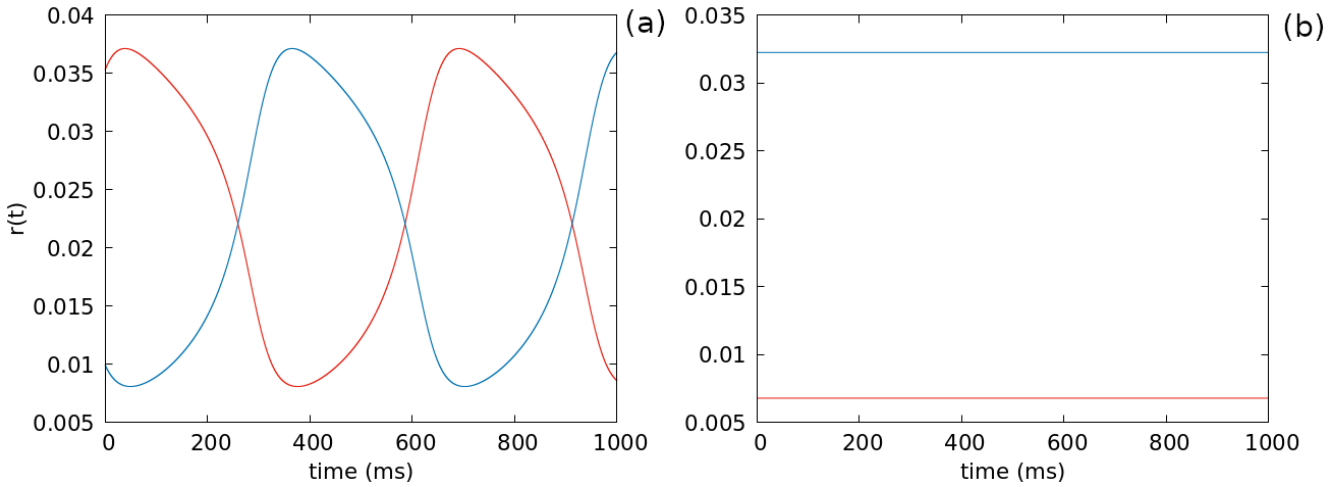

Figure 5.2.2: Time simulation of the system described in Eq. (5.1.0.1). Panel (a) and (b) respectively referred to region (II, asynchronous oscillations) and (III, asymmetric fixed point) in Fig. 5.2.1. Panel (a) parameters: $J_{cross} = 15$, $J_{self} = 5$. Panel (b) parameters: $J_{20} = 15$, $J_{self} = 10$

Through MATCONT we have determined that the first Lyapunov coefficient is negative along the two Hopf curves in Fig. 5.2.1. On a side note, we have found a Generalized Hopf point for low positive J_{self} values, suggesting that, even for weakly excitatory populations, this transition might be hysteretical. Since we are interested in inhibitory populations, the consequence of such bifurcation which occurs for $J_{self} > 0$ is that we are on the non-hysteretic side of the Hopf bifurcations.

To furtherly confirm what we have found with MATCONT, we have studied the dynamics along a quasi-adiabatic path crossing the three previously described regions. The results are shown in Fig. 5.2.3

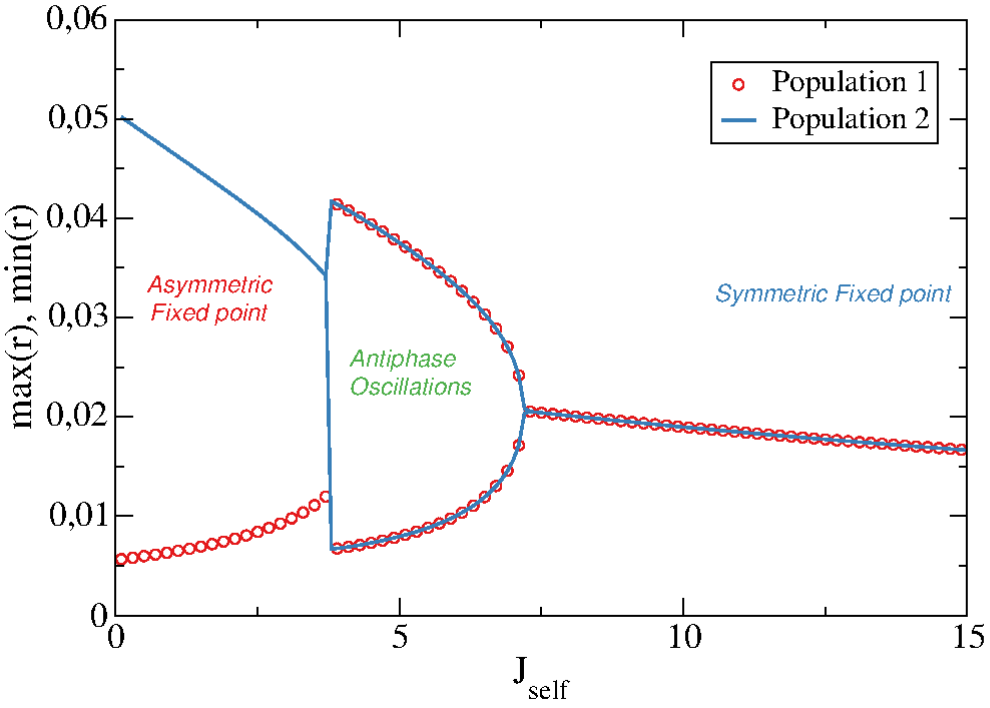

Figure 5.2.3: Plot of max(r), min(r) versus J_{self} along the path shown in Fig. 5.2.1. In red: population 1 data, in blue: population 2 data. Starting from low J_{self} we observe asymmetric fixed point (III), asynchronous oscillations (II) and symmetric fixed point (I). Time simulation examples are shown in Fig. 5.2.2. Other parameters are $\alpha = 5, \eta = 5.87, J_{cross} = 15$.

We note that inside the antiphase oscillations region, maxima and minima are identical for both populations, thus the only difference between the two populations in this regime is the relative phase which, however, is constant. The asymmetric fixed point and the symmetric fixed point show the usual behaviour as shown in Fig. 4.2.3

5.2.2. Case ii: (J_{cross}, η) plane

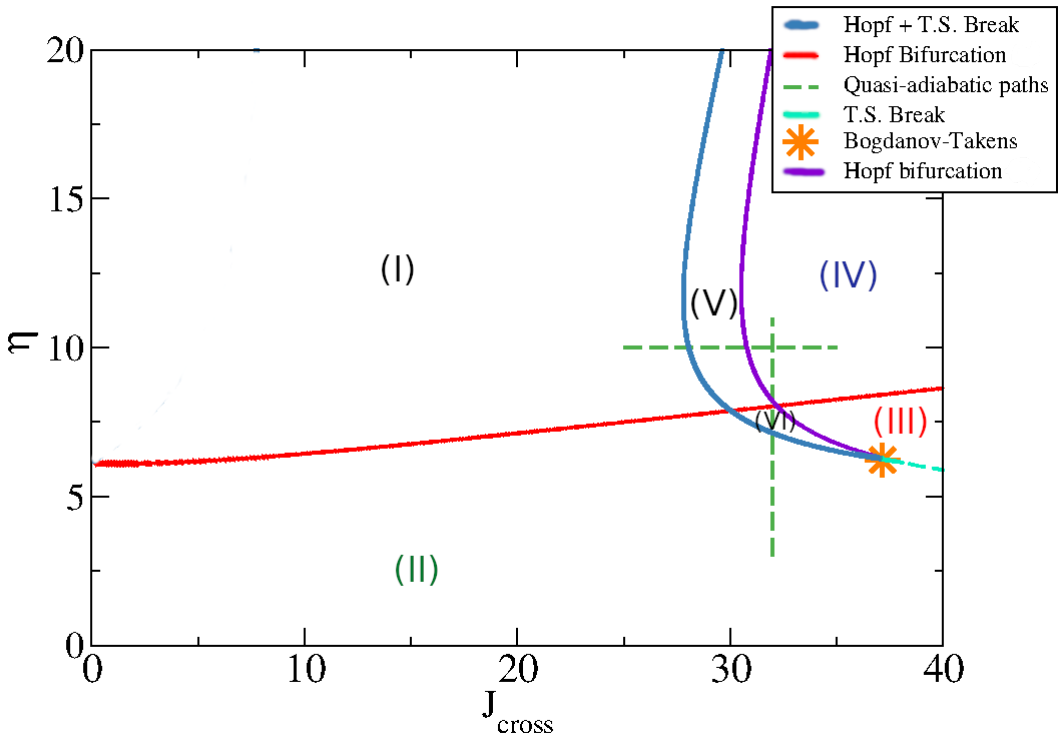

Figure 5.2.4: Phase diagram in the Parameter plane J_{cross}, η. Red curve: Hopf bifurcation related to the emergence of fast oscillations. Blue curve: Hopf bifurcation overlapped with a T.S. break curve. Violet curve: Hopf bifurcation related to slow asynchronous oscillations. Light blue: T.S. break. Green dashed lines: quasi-adiabatic paths studied in Fig. 5.2.5 and Fig. 5.2.6. Orange star: Bogdanov-Takens marking the split of the T.S. break into two hopf. Observed stable regimes are: (I) symmetric collective oscillations; (II) symmetric fixed point; (III) asymmetric fixed point; (IV) symmetric collective oscillations; (V) Slow oscillations with fast nested oscillations; (VI) Asynchronous oscillations; Relevant time simulations are shown in Fig. 5.2.7. Other parameters are $J_{self} = 20, \alpha = 5$.

In this parameter plane, by varying the neuron excitability η, we can confirm what we previously stated about collective oscillations: stronger adaptation effects require higher η values for the emergence of symmetric collective oscillations. As a consequence, the Hopf bifurcation (red curve)

can be found for slightly higher J_{cross} values than in the previous case with no adaptation, shown in Fig. 4.2.2. In addition to this, we once again observe the occurence of a Bogdanov-Takens bifurcation along the T.S. break curve. This brings to the emergence of two Hopf bifurcation curves such as those described in Fig. 5.2.1.
Below the horizontal Hopf bifurcation, the two new Hopf curves define the region where both the longitudinal and the transverse symmetry are broken, thus giving rise to a limit cycle along which the two populations are ynchronously globally active. (Fig. 5.2.7 (c)). Defining as η_H the excitability η value at which the Hopf bifurcation (red curve) occurs, we observe that, for $\eta > \eta_H$, where the system shows collective oscillations (reported in panel (b) and (d) of Fig. 5.2.7), the two Hopf enclose a region with a peculiar behaviour where high frequency oscillations are nested into a low frequency oscillation. An example of this regime is shown in panel (a) of Fig. 5.2.7.

In order to better investigate which scenarios arise when undergoing these new bifurcations, we study the dynamics along the two quasi-adiabatic paths shown in Fig. 5.2.4.

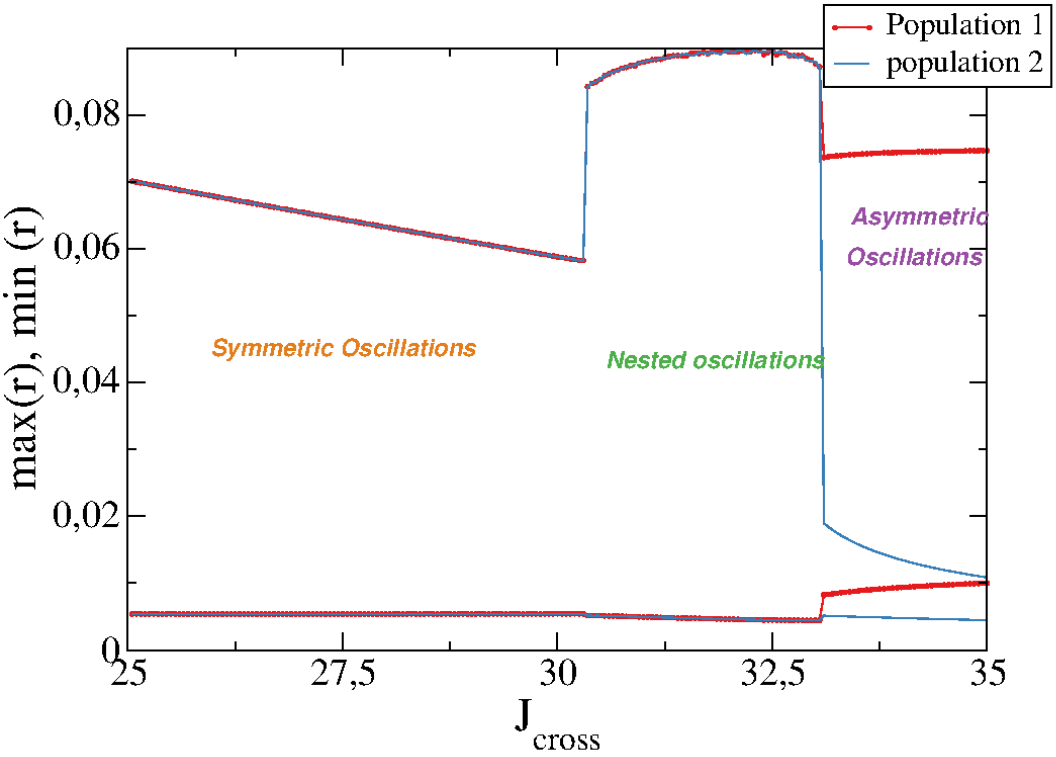

Figure 5.2.5: Plot of max(r), min(r) versus J_{cross} along the horizontal path shown in Fig. 5.2.4. red circled line: population 1 data, blue line: population 2 data. From left to right: symmetrical collective oscillations, nested oscillations, asymmetric collective oscillations. Time simulation examples are shown in Fig. 5.2.7. Other parameters are $\eta = 10$, $\alpha = 5$, $J_{self} = 20$.

Starting from low J_{cross}, in Fig. 5.2.5 we observe a regime of symmetric oscillations (identical evolution for both populations). After crossing the Hopf+T.S. break shown in Fig. 5.2.4 we see that the dynamics of both population is described by asynchronous slow oscillations ($freq \approx 1\,Hz$) with significantly faster nested oscillations ($freq \approx 30\,Hz$). Note that the overall amplitude (i.e. difference between maximum and minimum) is greater for this dynamics than for any other regime we have observed. For even greater J_{cross} we cross another Hopf bifurcation which shuts down the slow oscillations and we move towards the asymmetric collective oscillations regime.

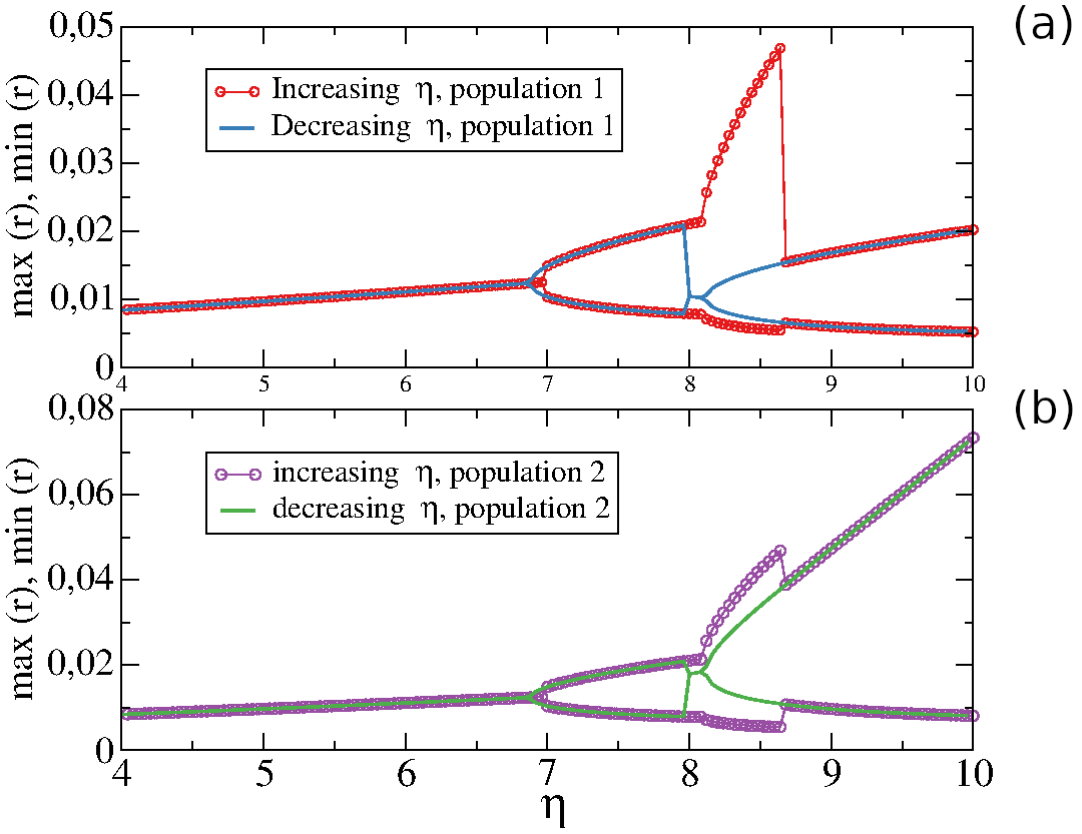

Figure 5.2.6: Plot of max(r), min(r) versus η along the vertical path shown in Fig. 5.2.4. Panel (a): population 1 data, panel (b): population 2 data. From left to right: symmetrical fixed point, asynchronous oscillations , nested oscillations, asymmetric collective oscillations. The difference between the results for increasing and decreasing η suggests a hysteretic transition from nested oscillations to asymmetric collective oscillations. Time simulation examples are shown in Fig. 5.2.7. Other parameters are $J_{cross} = 32$, $\alpha = 5$, $J_{self} = 20$.

In Fig. 5.2.6 we reported the analysis results of the dynamics simulation along a quasi-adiabatic path at fixed J_{cross} (shown as a vertical dashed line in Fig. 5.2.4). Starting at low η values we observe a fixed point. After crossing $\eta \approx 7$ we encounter a dynamical transition into an oscillatory state (antiphase oscillations). After $\eta \approx 8$ we observe another oscillatory state with a higher amplitude, corresponding to nested oscillations. Afterwards, the two populations exhibit another transition into an asymmetric collective oscillations state. By repeating the process for decreasing η, we observe a hysteresis region for the entire range of the nested oscillations. By this we can conclude that there is a small bistability region between asymmetric collective oscillations

and nested oscillations. Examples of the dynamics at different regimes are shown in Fig. 5.2.7

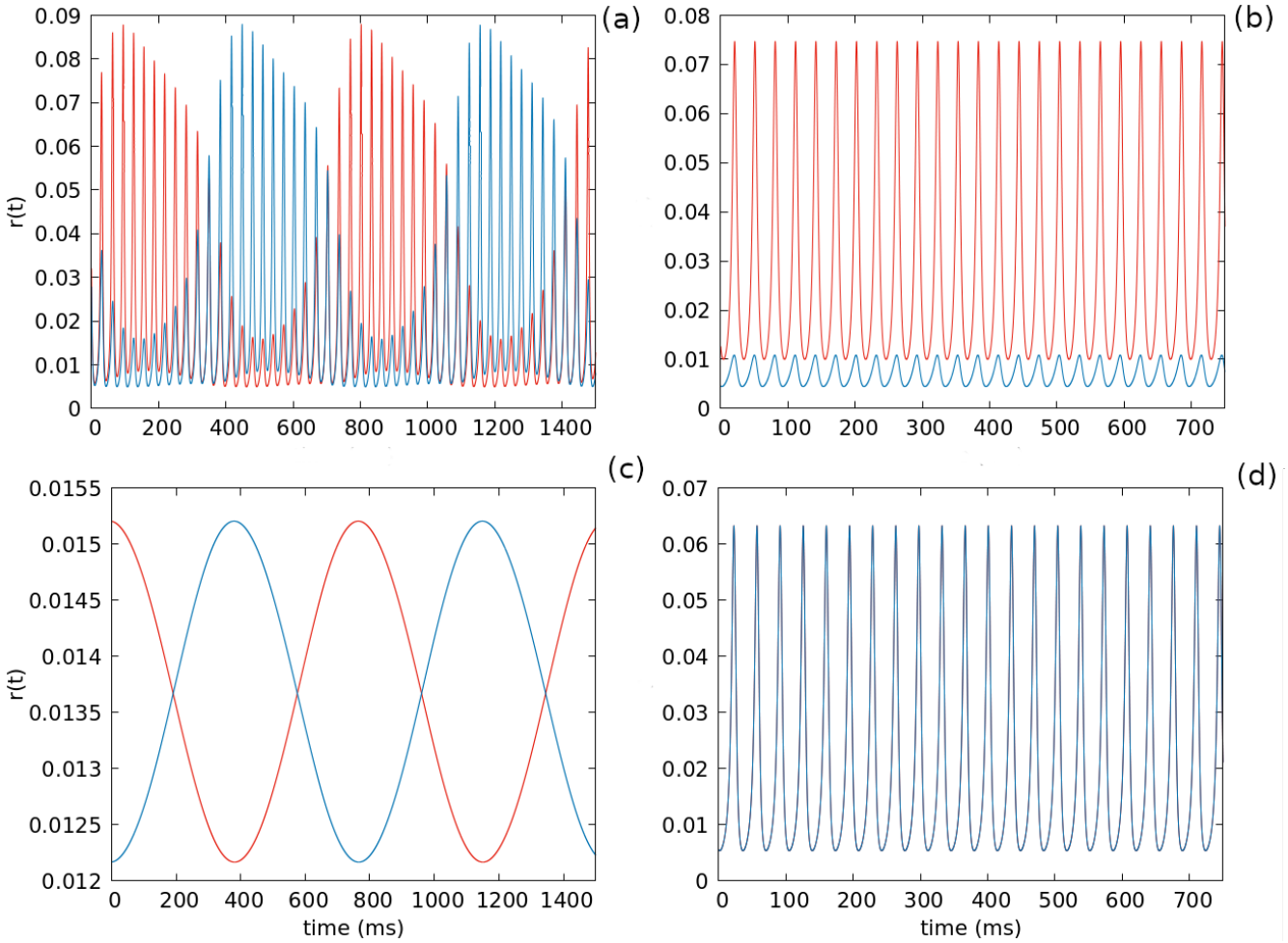

Figure 5.2.7: Time simulation of the system described in Eq. (5.1.0.1). Dynamical regimes observed in Fig. 5.2.4.(a) region (V). (b) region (IV). (c) region (VI). (d) region (I). Panel (a) parameters: $J_{cross} = 32$ $\eta = 10$. Panel (b) parameters: $J_{cross} = 35$ $\eta = 10$. Panel (c) parameters: $J_{cross} = 32$ $\eta = 7.5$. Panel (d) parameters: $J_{cross} = 27$ $\eta = 10$.

As a last significant characterization of our system dynamics in this plane, we want to investigate the power spectrum of the solutions with multiple frequency components . This allows us to inspect the various spectral components of our signal in order to better understand the coupling between the two different oscillations that we observe in the time traces. Results are shown in Fig. 5.2.8

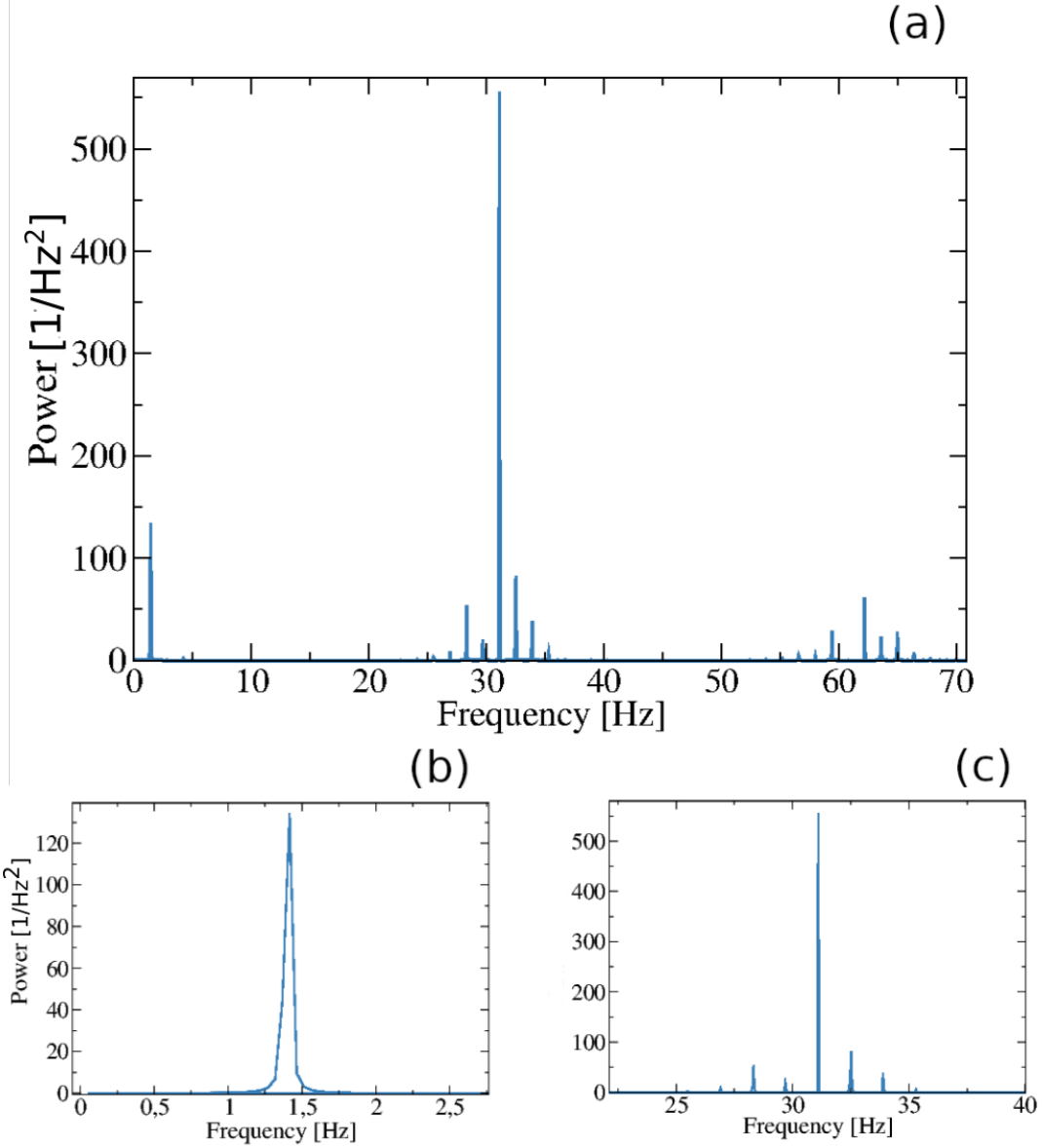

Figure 5.2.8: (a) Full power spectrum related to the signal given by the time evolution of the firing rate for a nested oscillations regime. System parameters are: $\alpha = 5$, $J_{self} = 20$, $J_{cross} = 32$, $\eta = 10$. (b) low frequency region; (c) high frequency region. Computed frequencies are compatible with the periods observed in Fig. 5.2.7(a).

The power spectrum shows two major peaks at $freq \approx 30Hz$ and $freq \approx 1.5Hz$. The low frequency peak corresponds to the slow, high period oscillations while the high frequency peaks

are the main spectral components of the nested, low period oscillations. The phenomenon of interaction between oscillations at different frequency bands is particularly significant in neuroscience [10] [69] because it has been widely observed in human and animal brain (especially in cortical regions) in various tasks such as perception, memory and attention [7]. In our specific case, phase coupling between breathing and whisking in rodents has been directly observed [17]. For these reasons, we will devote Section 5.4 to furtherly explore these solutions which exhibit cross-frequency coupling.

5.3. $\alpha - \eta$ parameter plane

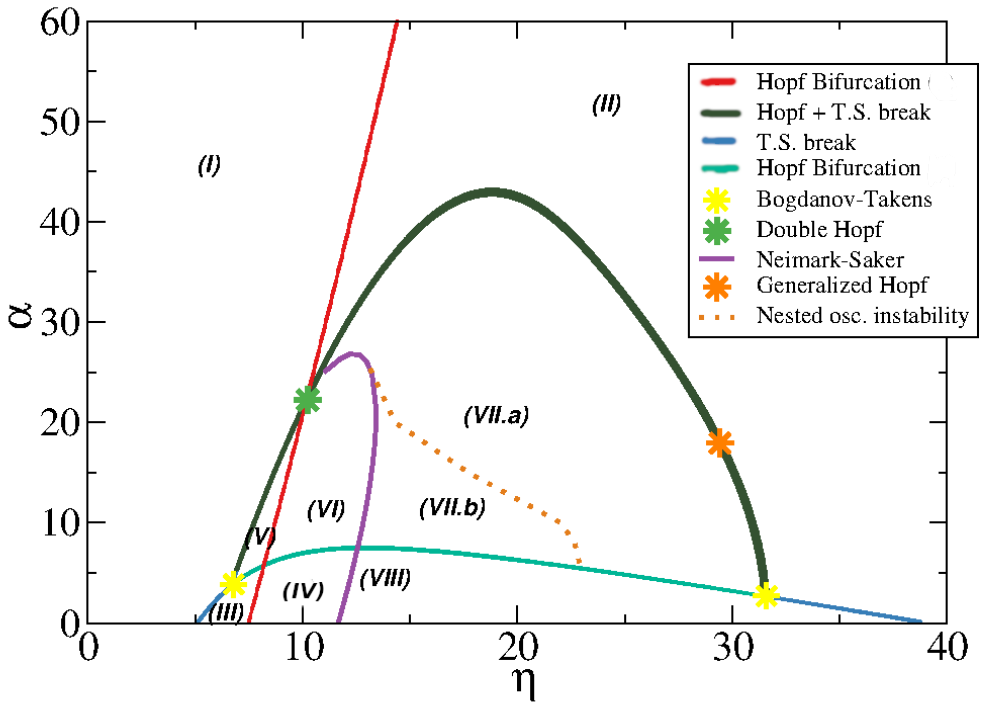

Figure 5.3.1: (α, η) parameter plane. Observed stable regimes are: (I) symmetric fixed point; (II) symmetric collective oscillations; (III) asymmetric fixed point; (IV) asymmetric collective oscillations; (V) antiphase oscillations; (VI) nested oscillations; (VII.a) symmetric collective oscillations; (VII.b) bistability between symmetric COs and nested oscillations; (VIII) bistability between symmetric COs and asymmetric COs. Time evolutions examples in Fig. 5.2.7 and Fig. 5.4.1. Other parameters: $J_{cross} = 33, J_{self} = 20$.

Here we have chosen $J_{self} = 20$ and $J_{cross} = 33$ in order to obtain non-trivial, asymmetric solutions, in accordance with previous findings.

There are various interesting things we can learn about our system by studying this parameter plane.

- The red curve represents a supercritical (positive first Lyapunov coefficient) Hopf bifur-

cation. In the upper side of the plane, it marks the boundary between region (I) and region (II), where we respectively find a stable symmetric fixed point and stable collective oscillations. It's important to stress the fact that, even for extremely high adaptive effects ($\alpha \approx 60$), the collective oscillations are not completely shut down. Specifically, this is similar to what we have seen for the one-population system (Fig. 3.3.1), where increasing α brought the collective oscillations region to shrink until it eventually disappears. However, in this case, we see that the inhibition due to the adaptation can be compensated by increasing the neuron excitability η. The positive slope of the curve is consistent with this interpretation.

- For low α values we see a transverse symmetry breaking curve, which defines the passage from a symmetric fixed point (I) to an asymmetric fixed point (III). Starting from this region and crossing the aforementioned Hopf bifurcation (red curve) will bring the asymmetric fixed point to lose its longitudinal stability, thus giving rise to asymmetric collective oscillations (IV). An example of this dynamical regime is shown in Fig. 5.2.7 (b). Furthermore, we note that taking $\alpha = 0$ (vanishing adaptive effects after a transient time period) and varying η would give us the exact response as in *Fig.* 4.2.4.

- At a critical α value ($\alpha_c \approx 4$) the T.S. breaking curve splits into two Hopf bifurcations via a Bogdanov-Takens (BT) codim 2 bifurcation, similarly to what we have seen in Fig. 5.2.4. This bifurcation is one of the key effects of the adaptation on our system. With low enough η (i.e. on the left of the Hopf bifurcation, region (V)) we see stable antiphase oscillations, such as those shown in Fig. 5.2.2 (a). Crossing the Hopf bifurcation (red curve) towards region (VI), the previously mentioned antiphase limit cycle becomes unstable, as confirmed both by simulating the system evolution and by performing a Floquet multipliers analysis via MATCONT (see Appendix A for details). In this region the system exhibits a cross-frequency coupling between slow and fast oscillations (as shown in Fig. 5.2.7, (a)), which we will furtherly analyze in Section 5.4. The two Hopf bifurcations, enclosing this region, form a closed curve as they starts from a BT bifurcation and reunite at another BT bifurcation for $\eta \approx 30$. This will produce another T.S. breaking curve with a similar dynamical meaning as the one discussed above. Moreover, this means that, for high enough α values, keeping J_{self} and J_{cross} at constant values, the nested oscillations region vanishes, leaving room only for symmetric collective oscillations.

- Along the upper Hopf bifurcation (Hopf + T.S. break curve), at $\eta \approx 28$, we find a General-

ized Hopf (GH) codim 2 bifurcation. According to what we have already seen in Chapter 4, this allows us to make a distinction between a super-critical (higher values of η) and a sub-critical transition (lower values of η). Unfortunately we had no way to confirm the presence of an hysteretic region in the neighbourhood of the bifurcation through direct simulation. This is because, while crossing the Hopf near the GH, the system dynamics always converge to a collectively oscillating regime for any parameter value.

To furtherly investigate this, we looked for bistable regimes. Through MATCONT we were able to study the stability of collective oscillations across the entire region of the parameter plane bordered by the two Hopf bifurcations. Through the application of Floquet multipliers we discovered that collective oscillations are stable through the entire extension of regions (VII.a), (VII.b) and (VIII). This is confirmed by the Neimark-saker bifurcation curve that we have found and shown in Fig. 5.3.1 in violet. This curve represents the boundary of the stability region of collective oscillations, so that, on the left of the curve, the COs are unstable. Now, in order to obtain proof of bistability, we need to check if the other solutions are stable as well. We start in the region (VIII). Here both MATCONT and explicit simulations show that the asymmetric collective oscillations are stable, thus providing us with a large bistability region. We can see the extent of this phenomenon in Fig. 5.3.2

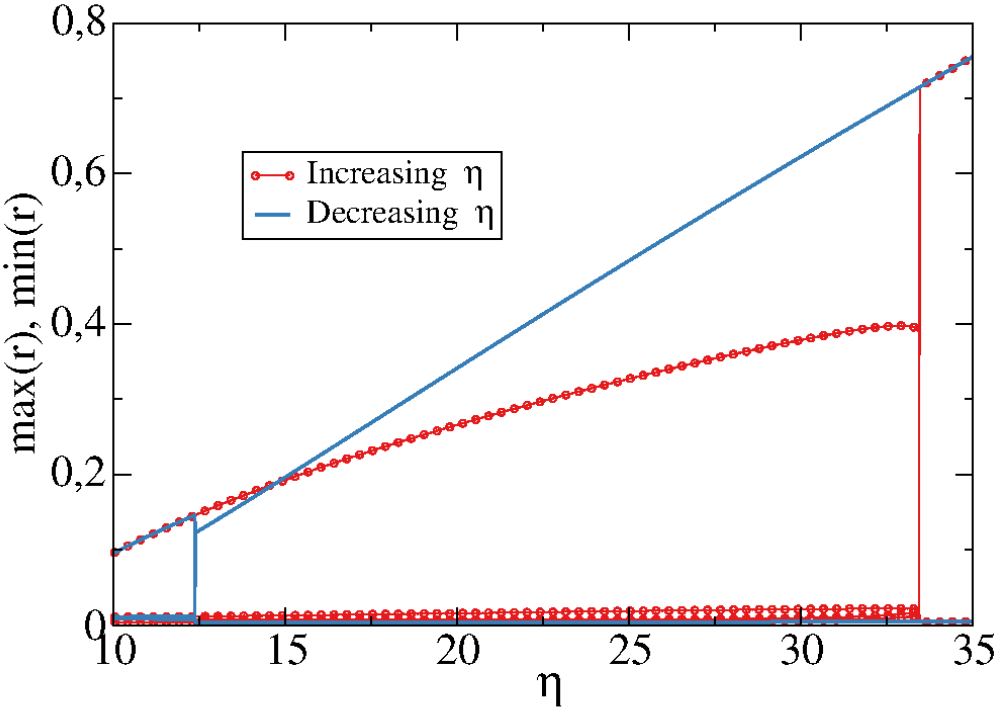

Figure 5.3.2: Plot of max(r), min(r) versus η along a horizontal path at $\alpha = 2$ in Fig. 5.3.1. In red: population 1, in blue: population 2. Low η values: asymmetric collective oscillations. High η values: symmetric collective oscillations. central region: bistability between the two behaviours. Other parameters are $J_{cross} = 33$, $\alpha = 2$, $J_{self} = 20$.

Through a quasi adiabatic path at constant α and by varying η we see that the asymmetric collective oscillations are stable until the T.S. breaking. At the same time symmetric collective oscillations are stable on the right of the Neimark-saker bifurcation. Therefore we conclude that, in region (VIII), we have bistability between the two aforementioned regimes.

- Following the same course of action for region (VII) is not as easy because MATCONT does not allow us to study in detail the stability of nested oscillations, thus we can only rely on simulations of the system. Therefore, we start by studying the dynamics along quasi-adiabatic paths at constant α. Some examples are shown in Fig. 5.3.3

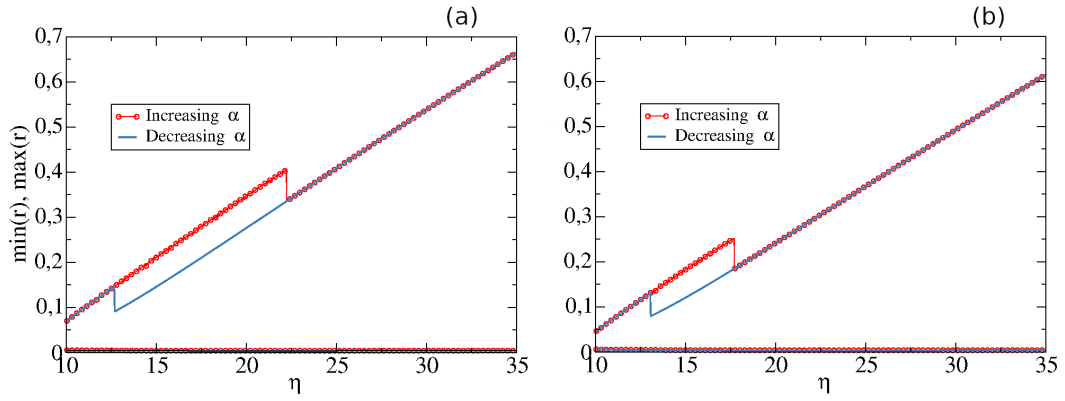

Figure 5.3.3: Plot of max(r), min(r) versus η along two horizontal paths at $\alpha = 10$ (panel (a)) and at $\alpha = 15$ (panel (b)) in Fig. 5.3.1. In red: population 1, in blue: population 2. Low η values: nested oscillations. High η values: symmetric collective oscillations. central region: bistability between the two behaviours. As underlined in Fig. 5.2.5, nested oscillations tend to have higher amplitude than collective oscillations for equal values of η. Other parameters are $J_{cross} = 33$, $J_{self} = 20$.

First of all we observe that nested oscillations apparently lose their stability at some value of η which depends on α. Specifically we see that, for higher α, the stability is lost for increasingly lower values of η. Moreover, that collective oscillations turn out to be stable everywhere on the right of the Neimark-Saker curve. By repeating this process for various values of α, we can build up an approximate curve (brown dotted curve) which defines the region where nested oscillations are stable, thus providing us with a reasonably accurate description of the dynamics in that region (VII.a). Overall, this procedure suggests that inside (VII.b) the only stable solution are collective oscillations, while in (VII.a) we can observe both collective oscillations and nested oscillation, with appropriate initial conditions. The precise meaning of the Generalized Hopf remains unclear as it does the upper right boundary of the (VII) region. Further work will be done in the future to clarify the behaviour of the system. For now, we note that the unclear region occurs for high values of η and α and that we have already found a wide variety of interesting dynamics.

5.4. Cross-frequency coupling and nested oscillations

While studying our system we have encountered a dynamical regime where, for both populations, we observe an interaction between oscillations at different frequency levels. This particular behaviour is known as Cross-frequency coupling (CFC) and it has been observed in several species such as rats, monkeys, humans and in several brain regions like the hippocampus and the cortex. We know that CFC has been associated with cognitive events, sensory perception and working memory [9]. Furthermore, cross-frequency coupling has been proposed to coordinate neural dynamics across spatial and temporal scales [2], which is connected to what we are looking for. Due to this large interest in neuroscience and since we have a relatively large region in this parameter plane where this dynamics occur, we can study in more detail the frequency range of these oscillations. Besides, we notice a relevant detail: in order to attain the cross-frequency coupling, we need to have sufficiently high α and η.

In order to see the effects of the adaptation on the frequencies, we observe the dynamics by keeping a fixed value of η and increasing α. The results of this are shown in Fig. 5.4.1.

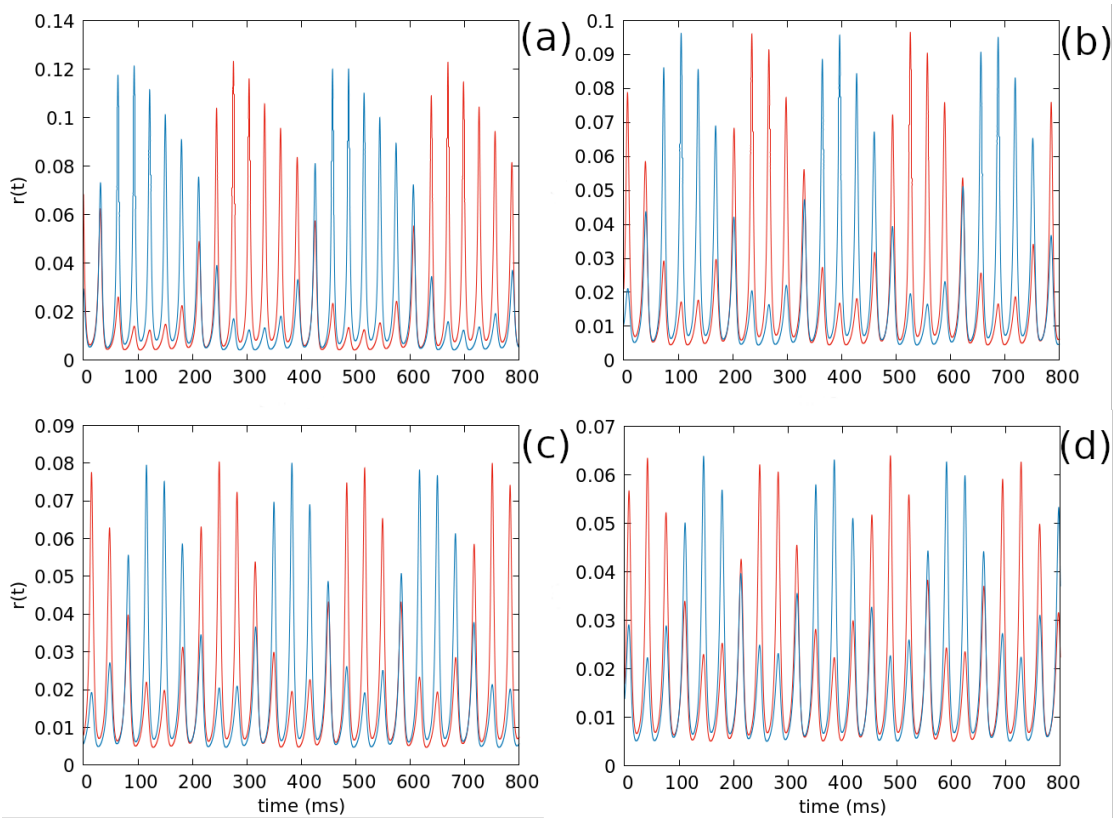

Figure 5.4.1: Time simulation of the system described in Eq. (5.1.0.1) for various values of α. (a) $\alpha = 11$; (b) $\alpha = 16$; (c) $\alpha = 19$; (d) $\alpha = 22$. Other parameters are $J_{self} = 20, J_{cross} = 33, \eta = 12$. The time period of the slow oscillaton decreases, while the time period of nested oscillaitons slightly becomes larger.

We note that the effect of increasing α is to decrease the overall amplitude and sligthly reducing the frequency of the fast oscillations, while at the same time the frequency of the slow oscillations increases. We can explicitly determine the frequencies by looking at the power spectrum of the time trace of the coordinates evolutions. Results are shown in Fig. 5.4.2

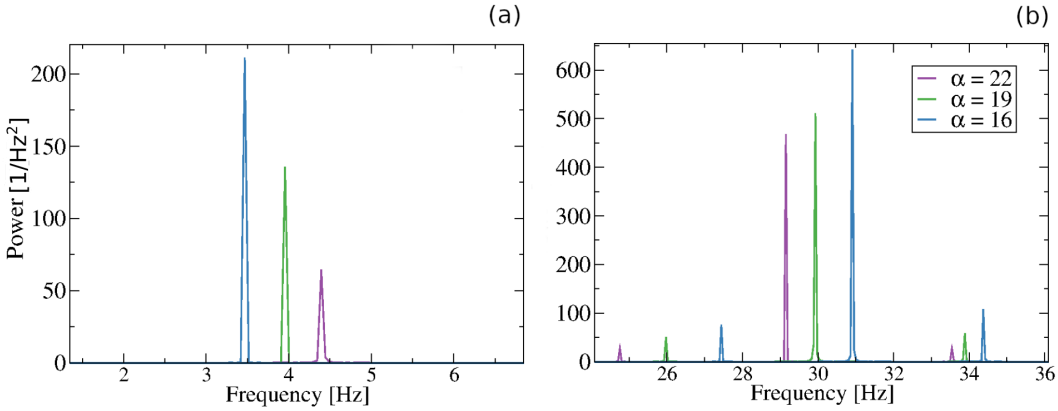

Figure 5.4.2: Power spectra of the firing rate time evolution in nested oscillations regime for three different values of α. Purple curve: $\alpha = 22$. Green curve: $\alpha = 19$. Blue curve: $\alpha = 16$. Panel (a): low frequency region. Panel (b): high frequency region. Other parameters are: $\eta = 12$, $J_{cross} = 33$, $J_{self} = 20$

The spectrum shown for $\alpha = 22$ is particularly interesting because we see that the low frequencies are in the θ-range (4 - 10 Hz) while the higher frequencies lie in the γ-range (25 - 140 Hz). We underline that hippocampal θ waves appear when a rat is engaged in active motor behavior such as walking or exploratory sniffing [65]. This is relevant as we can find these frequencies in our system both as the enveloping frequency for nested oscillations and as the actual spiking frequency in antiphase oscillations, where the two populations fire in an alternating pattern at θ frequencies, suggesting the possibility to obtain a stable regime in which protraction and retraction follow one another.

Therefore, we can conclude that, with an adequate set of parameters (i.e. $J_{cross} > J_{self}$), a model made up by two identical inhibitory populations of tonic neurons with exponentially decaying synapses and adaptation is capable of giving rise to θ-nested γ oscillations, which are believed to represent a fundamental mechanism to transfer information across spatial and temporal scales [60].

Finally, we explore the effects of increasing η while maintaining constant α. The power spectra for three distinct examples are shown in Fig. 5.4.3

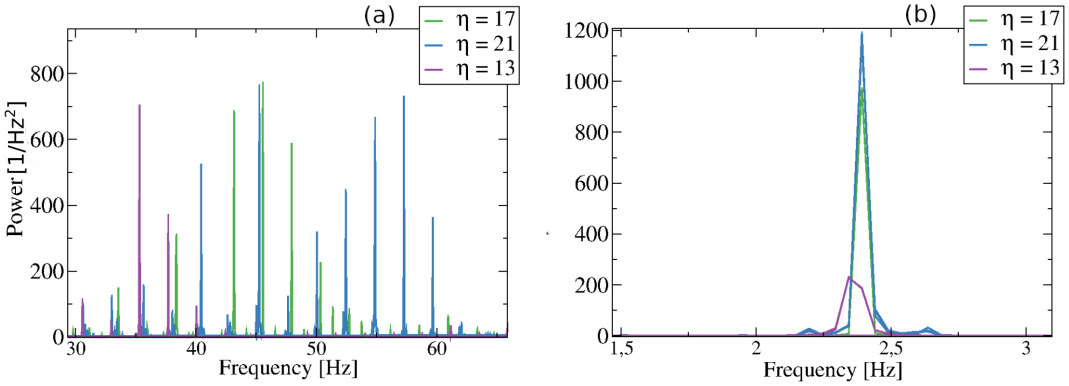

Figure 5.4.3: Power spectra of the firing rate time evolution in the nested oscillation regime for three different values of η. Purple curve: $\eta = 13$. Green curve: $\eta = 17$. Blue curve: $\eta = 21$. Panel (a): low frequency region. Panel (b): high frequency region. Other parameters are: $\alpha = 10$, $J_{cross} = 33$, $J_{self} = 20$

Here we see that, as expected, increasing the mean excitability/external current of the network increases the activity, thus resulting in a higher frequency of fast oscillations. Still, the slow oscillations keep roughly the same frequency, thus suggesting that the emergence of such oscillations is mostly connected to adaptation.

Conclusions

The goal of the original research activity of this thesis was to find a model that could describe the whisking rhythmogenesis in rats. The work has been inspired by the seminar *theory and modeling of whisking rhythm generation* proposed by Prof. D. Golomb [31], who presented the circuit model (Fig. 1.10.1) that we used as a starting point for our work. His model describes a circuit of a neuronal network that could explain whisking rhythmogenesis in rodents. The main physical object of study is the vibrissae intermediate reticular formation (vIRt) nucleus in the medulla, which is necessary for whisking rhythm generation [17]. The vIRt innervates neurons in the facial nucleus (FN) that project to intrinsic vibrissae muscles. Knowing this, Golomb assumed a circuit composed by two hypotetical vIRt groups, vIRt_r and vIRt_p, respectively related to vibrissae retraction and protraction. The two populations were made up by bursting inhibitory neurons with spike-frequency adaptation currents and constant external inputs. In this thesis we decided to adopt a Quadratic Integrate and Fire (QIF) model to describe the dynamics of single neurons and we followed the analytical method proposed by E. Montbrió, D. Pazó, A. Roxin [46] to derive an exact mean-field description of a neural network with N degrees of freedom, through a system of few differential equations which define the macroscopic evolution of the network. This was possibile since single QIF neurons can be seen as phase oscillators with instantaneous impulsive coupling, allowing us to apply the approach developed by Ott and Antonsen [54] for a heterogeneous network of phase oscillators. The original mean-field model [46] was derived for a single QIF population with instantanenous synapses, in this thesis we have extended such model by including important physiological aspects. In particular, we have implemented in such model both synaptic transmission characterized by a finite time and frequency adaptation due to neuronal fatigue. Furthermore, inspired by the model proposed by D. Golomb we considered the evolution of two coupled inhibitory QIF networks with the additional physiological aspects mentioned above. By doing this, we have characterized various

dynamical regimes that spontaneously emerge in systems of two coupled inhibitory populations of identical QIF neurons which, to our knowledge, have not been investigated before.
In particular, we have found that, in the case of inhibitory coupling with exponentially decaying synapses, we can observe a spontaneous symmetry breaking in the dynamical evolution, despite the permutational symmetry brought by the fact that the two populations are formally identical. Moreover, collective oscillations are not shut down due to the inhibitory cross coupling, if the neurons are tonic.

Subsequently, following Golomb's model, we introduced the PreBötzinger Complex (PreBötC) into our circuit model. PreBötC is a cluster of interneurons in the ventral respiratory group of the medulla of the brainstem and it is the neural network responsible for inspiration during respiratory activity [48]. Since we know that PreBötC has an important role in whisking rhythmogenesis because it projects inputs to the vIRt nucleus, thus contributing to the synchronization of vIRt neurons [1], we wanted to investigate how the inhibitory forcing affected the two vIRt populations. We have discovered that phase locked states between the two populations (and with the forcing oscillations as well) are possibile. In addition to that, we have found that there are cases in which the forced population is not fully entrained with the external input.
Having found that the two vIRt sub-populations exhibit collective oscillations with and without PreBötC coordination confirms the hypotesis according to which the PreBötC is not needed for rhythmic whisking activity [31, 17].

After that, we have introduced adaptation on both populations of our system, through a new variable for each population. This specific setup, which we have extensively studied, has not been analyzed in the literature before. We confirmed that an additional inhibitory effect does not prevent collective oscillations. Instead, adaptation leads to the emergence of antiphase oscillations, a dynamical regime in which the two populations have an alternating activity pattern (i.e. when one population is silent, the other one is at its peak activity and viceversa). This is quite peculiar and it could be useful in explaining the whisking activity, since the two sub-populations vIRt_r and vIRt_p are expected to have synchronous activity, respectively, in occurrence of vibrissae retraction and protraction.
Finally, a dynamical regime in which Cross-Frequency Coupling (CFC) occurs has been observed. In particular, we discovered a range of parameters where $\theta-\gamma$ nested oscillations, which are quite important in neuroscience [10, 69] show up. These results, which have not been found until now, might represent a first step in defining a new way in which these commonly observed oscillations emerge as a collective behaviour.

The results we have found represent a starting point for subsequent research activity. The next step will be the introduction of the PreBötzinger Complex inhibitory effect on the vIRT$_r$ subpopulation for the system in which we have included adaptation effects, in order to obtain a more realistic model of the whisking rhythm generation system. Furthermore, as shown in Fig. 1.10.1, a third neuron population, representing the Facial Nucleus, should be included in our model. This would be a relevant point because the Facial Nucleus contains the motor neurons for whisking [1], therefore it is directly connected to the muscular activity of the vibrissae retraction and protraction. In addition to that, studying the full circuit model will make it easier to compare the computational results with the extensive biological data available [17]. Aside from the specific purpose of modeling the rat whisking system, further research should be made into the phenomenon of Cross-Frequency Coupling due to adaptation, as $\theta-\gamma$ CFC, reported for Hodgkin-Huxley networks in [71], is not commonly observed at the level of exact neural mass models [11]. These mixed oscillations with frequency modulation are thought to have a fundamental role in perception and memory formation [35].

Appendix A

Bifurcation theory

In this appendix we give a short description of bifurcation theory. We start in Appendix A.1 by introducing the fundamental definitions and the most common *codim 1* bifurcations, while in Appendix A.2 we give some extra details on the codim 2 bifurcations that we have found on Chapter 4 and Chapter 5 and we discuss in general the stability of periodic trajectories in the phase space.

A.1. Introduction and basic concepts

In dynamical system, a *bifurcation* occurs when a small smooth change made to the values of some parameters (which take the name of *bifurcation parameters*) of a system causes a sudden "qualitative" or topological change in its dynamical behaviour. Generally, at a bifurcation, the local stability properties of equilibria, periodic orbits or other invariant sets change.

Moreover, in bifurcation theory, we say that a given dynamical transition is hysteretical when it occurs at different critical parameter values, hence we have a clearer procedure to identify this particular phenomenon.
Bifurcations can be classified in different ways:

- According to the *dimension* of the system, that is the number of dynamical variables through which our system is defined. Some bifurcations occur only when the dimension of the system is greater than a minimum critical value. Usually, one can study this kind of bifurcations in the minimum dimension at which it occurs;

- According to the *codimension* of the bifurcation, which is defined as the number of parameter whose variation leads to the bifurcation;
- *Local and global* bifurcations: in the first category stable fixed points disappear and change stability or new ones appear. Global bifurcations instead often occur when larger invariant sets of the system 'collide' with each other, or with the equilibria of the system.
- *sub-critical* and *super-critical* bifurcations, which we now explore in further detail.

We will study the bifurcations that we have found during this thesis, characterizing them according to this categories.

Under general conditions, the local behaviour of codim 1 bifurcation of a fixed point can be reduced to few fundamental characteristics. More precisely, it can be shown that there exist series expansions and variable changes such that, near a fixed point, the evolution of the system is described by a low number of differential equations which depend on a single bifurcation parameter μ [24]. After performing adequate variable transformations which take the fixed point to the origin $x = 0$ and the bifurcation point to $\mu = 0$, the dynamical equations take a particular form known as the *normal form* with the following structure

$$\dot{x} = f(x, \mu) \tag{A.1.0.1}$$

where the function $f(x, \mu)$ respresents the system evolution in the phase space. Through series expansion, f can be expressed as a polynomial in x with μ as a parameter.

A.1.1. Super-critical bifurcations

We now present the most common codim 1 bifurcation, up to the third order in the polynomial.

1. Fold or saddle-node bifurcation: $\dot{x} = \mu - x^2$

   If $\mu < 0$, the equation $f(x, \mu)$ has no real solutions, hence we do not find any fixed point. If $\mu = 0$, one solution exists at $x = 0$, which is unstable. At $\mu > 0$, two solutions emerge. One being a stable solution $x = \sqrt{\mu}$ and one being an unstable solution, $x = -\sqrt{\mu}$, as shown in Fig. A.1.1 (A).

2. Transcritical bifurcation: $\dot{x} = \mu x - x^2$

   In this case we have two fixed points $x = (0, \mu =$, whose stability are exchanged when the bifurcation parameter crosses the critical value $\mu = 0$: Therefore, for $\mu < 0$, we have that

$x = 0$ is stable and $x = \mu$ is unstable. The stability is inverted when $\mu > 0$. The bifurcation scheme is represented in Fig. A.1.1 (B).

3. Pitchfork bifurcation: $\dot{x} = \mu x - x^3$.

   For $\mu < 0$ we only have a stable fixed point in $x = 0$ which becomes unstable at $\mu = 0$. At the same time, two stable equilibria $x = \pm\sqrt{\mu}$ appear as $\mu > 0$ (see Fig. A.1.1 (C)).

4. Hopf bifurcation: $\dot{z} = (\mu + i\gamma)z - z|z|^2$.

   In this normal form z is a complex variable while γ is a constant unrelated to the bifurcation process. As a consequence, this particular bifurcation cannot occur for one-dimension systems. Furthermore, this normal form is equivalent to the pitchfork bifurcation with complex variables. In order to find a solution, it is convenient to transform the complex variable to two real cartesian coordinates. Through the substitution $z = x + iy$ the normal form becomes:

$$\begin{aligned} \dot{x} &= [\mu - (x^2 + y^2)]x - \gamma y \\ \dot{y} &= \gamma y + [\mu - (x^2 + y^2)]y. \end{aligned} \tag{A.1.1.1}$$

   In addition to $z = 0$ (that is, $x = y = 0$) solution, there exist one more solution:

$$|z|^2 = (x^2 + y^2) = \mu \tag{A.1.1.2}$$

   which defines a circumference with radius equal to $\sqrt{\mu}$ in the (x, y) plane.

   Therefore, if $\mu < 0$ we have a single stable fixed point for $x = y = 0$, while for $\mu > 0$ it becomes unstable, but we see that a stable limit cycle appears (Fig. A.1.1(D)).

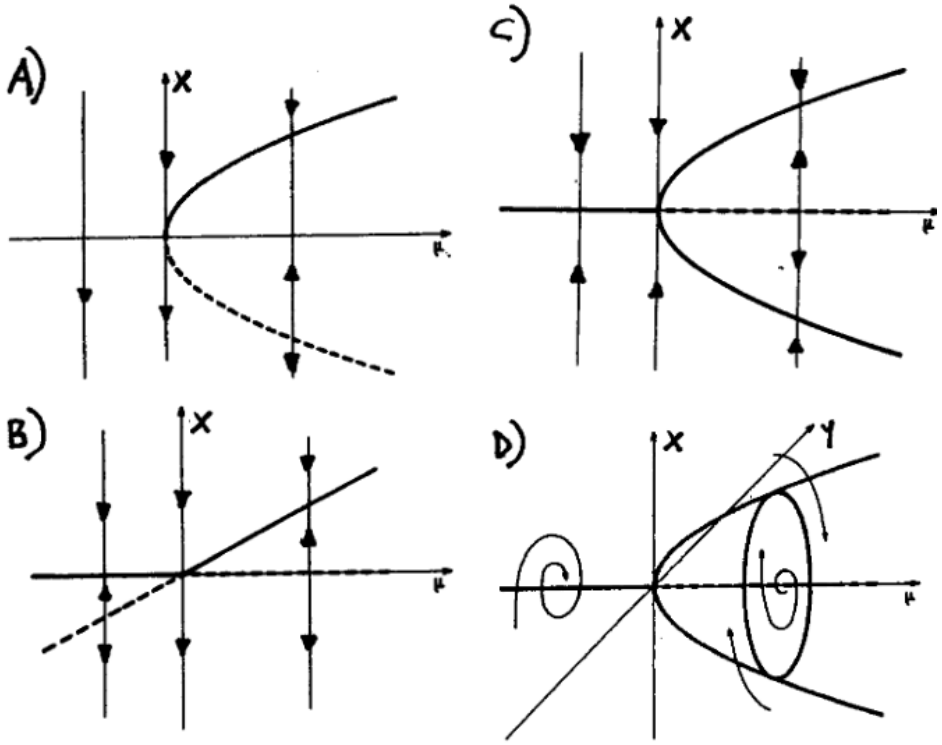

Figure A.1.1: Bifurcation diagrams for super-critical bifurcations: (A) saddle-node; (B) Transcritical; (C) Pitchfork; (D) Hopf. The continuous line stands for stable points while the dashed lines represent unstable points. The arrows describe the direction of the of the force lines related to the flux f(x, μ)[5].

A.1.2. Sub-critical bifurcations

The normal forms that we discussed until now, are usually referred to as $super - critical$ (or normal). With this definition we want to underline that the non-linear term in x^2 and x^3 have an opposite effect to the instability brought by the lowest-order term. As an example, consider the normal form $\dot{x} = \mu x - x^3$. For low x values we can consider only the linear term. Therefore, the solution that we obtain is $x = \exp \mu t$, which tends to diverge when μ is positive. However, the actual solution to the equation does not exponentially diverge because the linear term is counterbalanced by $(-x^3)$ which cannot be neglected. Evaluating the equation in the following form:

$$\dot{x} = \mu x \left[1 - \frac{x^2}{\mu}\right] \tag{A.1.2.1}$$

we clearly see that the non-linear term balances the effect of the linear instability when $x^2 = \mu$. However, there exist cases in which the non-linear term has a destabilizing effect on the solution. In these situations, the bifurcation is called $sub - critical$ or $inverse$.

All the normal forms that we examined in the previous setion can be transformed into their sub-critical counterpart simply by changing the sign of the non-linear term. Thus we get the bifurcation diagrams shown in Fig. A.1.2

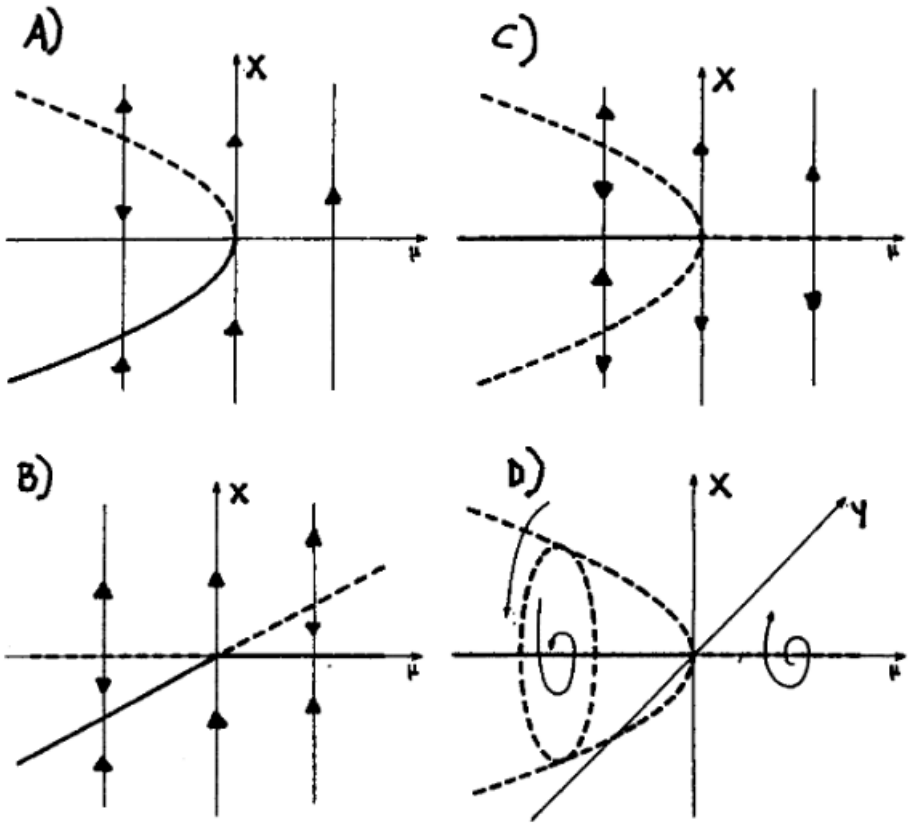

Figure A.1.2: Bifurcation diagrams for sub-critical bifurcations: (A) saddle-node; (B) Transcritical; (C) Pitchfork; (D) Hopf. The continuous line stands for stable points while the dashed lines represent unstable points. The arrows describe the direction of the of the force lines related to the flux $f(x, \mu)$ [5].

A.2. Codim 2 bifurcations

This section is devoted to bifurcations of equilibria in generic two-parameter systems of differential equations. We will focus on the bifurcations that we have found while studying the network

of two inhibitory identical populations of QIF neurons. In order to study such phenomena, we consider an autonomous system of ordinary differential equations

$$\dot{x} = f(x, \alpha), \quad x \in \mathbb{R}^n \tag{A.2.0.1}$$

depending on two parameters $\alpha = (\alpha_1, \alpha_2) \in \mathbb{R}^2$, where f is continuously differentiable smooth function $f : \mathbb{R}^n \longrightarrow \mathbb{R}^n$.
In addition to that, we define the set of linear stability eigenvalues ($\lambda = (\lambda_1, ...\lambda_n) \in \mathbb{R}^n$) at a certain phase space point x_0 as the eigenvalues of the *jacobian matix* associated to f at x_0, $J_{x_0}(f)$. We say that a fixed point x_0 is asymptotically stable (i.e. a stable fixed point) if and only if for all eigenvalues λ of J, $Re(\lambda) < 0$ [41]. The eigenvalues can be computed as the roots of the characteristic polynomial of the Jacobian associated to the smooth function f.

We assume that the variation of the two parameters α is responsibile for the codim 2 bifurcation occurrence. One way to classify these bifurcations is by studying the conditions on the system's linear stability (through its eigenvalues) under which it occurs. Therefore, we can vary the two parameters (α_1, α_2) to track a $codim1$ bifurcation curve in the (α_1, α_2) parameter plane. During this process, extra eigenvalues can approach the imaginary axis, thus triggering additional bifurcation processes. Additionally, some of the genericity conditions for the codim 1 can be violated. When this happens, we can expect the appearance of new phase portraits (i.e. new dynamics) for nearby parameter values, implying that a codim 2 bifurcation has occurred. The new phase diagram will depend on the kind of transition taking place while varying the parameters (as shown in the various examples for codim 1 bifurcations).

1. As a first step, let us follow a fold bifuration curve, which is a curve in the two parameters plane where an equilibrium with a simple zero eigenvalue $\lambda_1 = 0$ exists. While the curve is being tracked, an additional real eigenvalue λ_2 may approach the imaginary axis, so that

   $$\lambda_{1,2} = 0. \tag{A.2.0.2}$$

   These are the conditions for the $Bogdanov - Takens$ (or double-zero) bifurcation. To have this bifurcation we need $n \geq 2$.

2. Let us now follow a Hopf bifurcation curve. At a typical point in this curve, the system has an equilibrium with a simple pair of purely imaginary eigenvalues $\lambda_{1,2} = \pm i\omega_0$ and no other eigenvalues with $Re(\lambda) = 0$. Besides, at a non-degenerate Hopf point, the first Lyapunov coefficient (which characterizes whether the Hopf bifurcation is subcritical $l_1 > 0$

or supercritical $l_1 < 0$) is not equal to zero, $l_1 \neq 0$. For a definition of the Lyapunov coefficient, the reader is referred to [64]. While moving along this curve, two extra complex conjugate eigenvalues $\lambda_{3,4}$ can approach the imaginary axis, so that

$$\lambda_{1,2} = \pm i\omega_0, \quad \lambda_{3,4} = \pm i\omega_1. \tag{A.2.0.3}$$

These conditions define the *Hopf-Hopf* or *double-Hopf* bifurcation.

3. In addition to that, along a Hopf curve the first Lyapunov coefficient l_1 might vanish while $\lambda_{1,2} = \pm i\omega_0$, therefore:

$$\lambda_{1,2} = \pm i\omega_0, \quad l_1 = 0. \tag{A.2.0.4}$$

We call this event *Generalized Hopf* (or *Bautin*) bifurcation

We note that the Bogdanov-Takens can also be located along a Hopf bifurcation curve, as ω_0 approaches zero. At this point, two purely imaginary eigenvalues collide and we have a double zero eigenvalue.

A.2.1. Neimark-Sacker bifurcation and Floquet multipliers

In Chapter 5 we have used a Floquet multipliers analysis to study the stability of oscillatory regimes over a given range of the system's parameters. For mathematically based applications, the stability of non-linear oscillatory behaviors is determined by the Floquet multipliers [61]. In this section we will shortly present the basic ideas behind the computation of Floquet multipliers and describe the occurence of the Neimark-Sacker bifurcation.

Suppose that our system can be described by a system of differential equations like those that we previously considered:

$$\dot{x} = f(x, t, \lambda), \quad x \in \mathbb{R}^n \tag{A.2.1.1}$$

where λ is a generic set of real parameters. A generic trajectory of this system can be defined as $x = \phi(t, x_0)$, where $x_0 = (x_0^{(1)}, x_0^{(2)}, ...x_0^{(n)})$ are the initial conditions. If Eq. (A.2.1.1) allows for periodic solutions (such as limit cycles) then, for those trajectories, there exist a time period $T \in \mathbb{R}$, $T > 0$ such that $\phi(t + T, x_0) = \phi(t, x_0)$. The trajectory progresses to the regular orbit $x^* = \phi(t, x_0^*)$. Now we consider a weak perturbation d_0 to the initial condition set x_0^*, producing the orbit $\phi(t, x_0^* + d_0)$. The distance between the perturbed trajectory and the periodic orbit is

$$d(t) = \phi(t, x_0^* + d_0) - \phi(t, x_0^*) \tag{A.2.1.2}$$

The distance after one full period T can be calculated as $d(T)$. The linear representation through Taylor expansion becomes

$$d(T) = \frac{\partial \phi(T, x_0^*)}{\partial x} d_0. \tag{A.2.1.3}$$

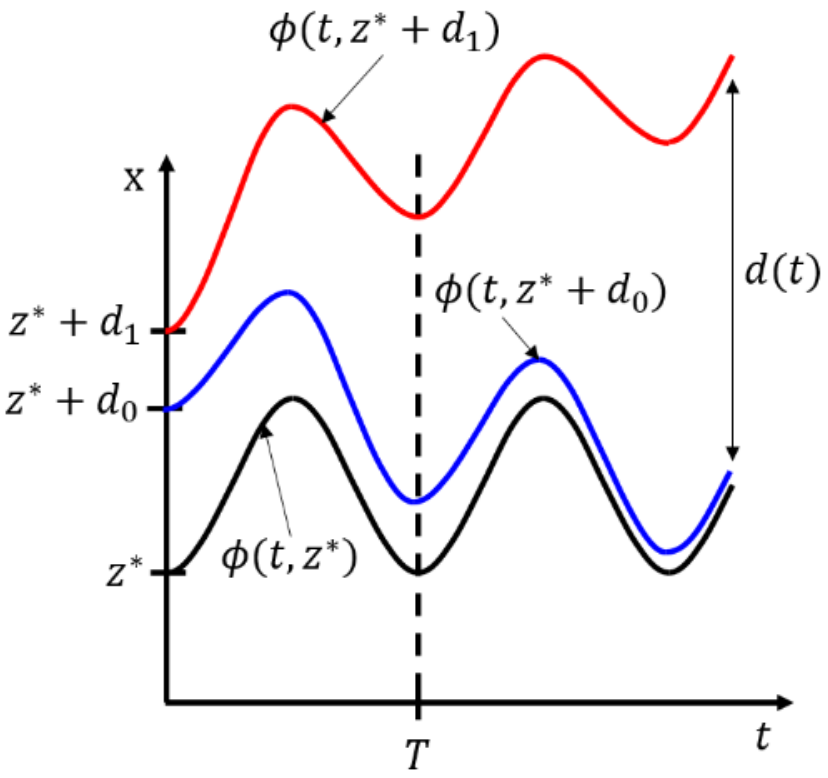

Figure A.2.1: A periodic trajectory of a system with initial condition z^* and an example of stable and unstable solutions for two different disturbances d_0 and d_1. T is the periodicity of the stable orbit. [13]

Keeping in mind that this approximation is valid only for small disturbances (as shown in Fig. A.2.1), we can extract the *Monodromy matrix* from the Taylor expansion as

$$M = \frac{\partial \phi(T, x_0^*)}{\partial x_0^*}. \tag{A.2.1.4}$$

The Monodromy matrix describes the growth or decay of the perturbation after one period, thus it helps us to define the stability of periodic solutions. The characteristics of the Monodromy matrix are directly related to the behavior of the specific periodic solution and determined by its n eigenvalues, $\mu_1(\lambda), ..., \mu_n(\lambda)$. These eigenvalues are known as Floquet multipliers. The

magnitude of one of them is always equal to unity, i.e. $|\mu_n = 1|$. The other $n-1$ eigenvalues determine the (local) stability of the periodic trajectory $x^*(t)$ according to the following rule:

- $x^*(t)$ is stable if $|\mu_j| < 1$ for $j = 1, ..., n-1$.
- $x^*(t)$ is unstable if $|\mu_j > 1$ for some j.

In other words, for a stable periodic trajectory, the $n-1$ multipliers should always be inside the unit circle in the complex plane. It's important to note that these eigenvalues are functions of the system parameters, therefore the stability of a given trajectory can change upon the variation of the parameters. The multiplier crossing the unit circle during a transition from stable to unstable trajectory is referred to as the *critical multiplier* and a graphic representation of a multiplier crossing the unit circle, while a parameter is varied, is shown in Fig. A.2.2.

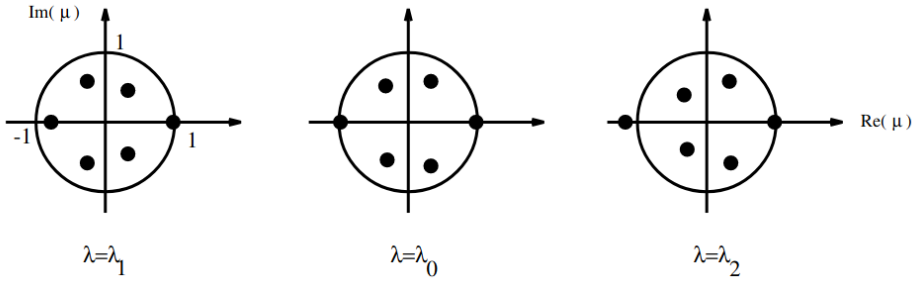

Figure A.2.2: Multipliers (eigenvalues of the monodromy matrix) for three values of *lambda*. λ_0 is the critical parameter value at which the transition from stability to instability of a periodic orbit occurs.

Depending on where the critical multiplier or pair of complex conjugate multipliers crosses the unit circle, different types of bifurcation occur. One distinguishes three ways in which this phenomenon may occur, with three associated types of bifurcation.

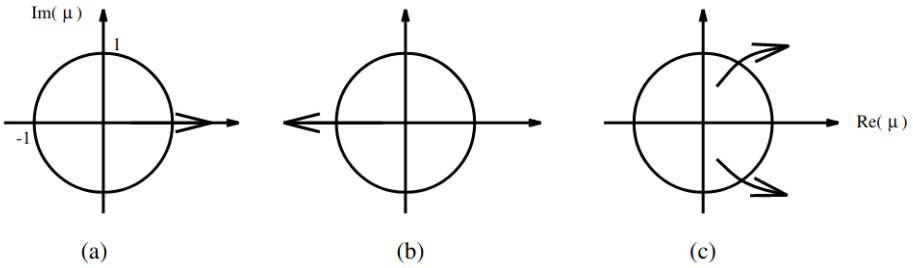

Figure A.2.3: Three different ways multipliers can leave the unit circle. (a) $\mu_j(\lambda) = 1$ for a j. (b) $\mu_j(\lambda) = -1$ for a j. (c) A pair of complex conjugate multipliers cross the unit circle.

In Chapter 5 we encountered the bifurcation related to panel (c) of Fig. A.2.3. This type of stability losing is characterized by a pair of complex-conjugate multipliers crossing the unit circle at

$$\mu(\lambda_0) = \exp \pm i\theta \quad \text{for} \quad \theta \neq 0, \theta \neq \pi \tag{A.2.1.5}$$

This kind of bifurcation is often called *Neimark-Sacker bifurcation (NS)*. By making use of Poincarè maps, it can be shown [61] that this bifurcation is associated with periodic orbits losing their stability to torus dynamics. This means that after the bifurcation occurs, the trajectory spirals around a torus-like manifold. Because this scenario requires complex multipliers in addition to the eigenvalue that is always equal to unity, a NS bifurcation can take place only for $n \geq 3$.

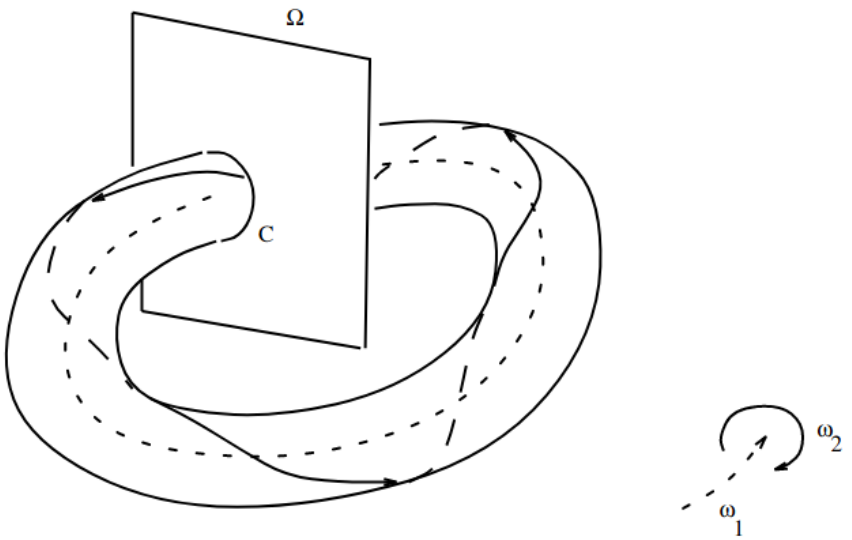

Figure A.2.4: Dynamics example on a 2-dimensional torus with two distinct frequencies $\omega_1(\lambda), \omega_2(\lambda)$, after a NS bifurcation. Ω is a Poincarè section and C is an invariant curve defined in Ω. For λ tending to λ_0, the diameter of the torus shrinks to zero and eventually reduces to the periodic orbit (that is, at λ_0 a bifurcation from a periodic orbit to a torus takes place) [61]

After the bifurcation from periodic orbit occurs, (with frequency $\omega_1(\lambda)$), there are two frequencies $\omega_1(\lambda), \omega_2(\lambda)$. One frequency describes the component of motion along the axis within the torus (longitudinal motion), the other frequency is measured along the cross section (latitudinal motion) (see Fig. A.2.4). The related flow is called *quasi-periodic* if the ratio ω_1/ω_2 is irrational. Furthermore, for some λ this ratio may be rational. In this specific case, we talk about *locked state*, the trajectory on the torus is closed and it is also periodic.

Appendix B

Symmetry breaking in two identical populations of QIF neurons

B.1. Transverse and Longitudinal symmetry

In this chapter we describe the method we used in order to study the longitudinal and transverse symmetry in Chapter 4 and Chapter 5. We follow the procedure presented in [58]

In the following, we refer to the system made up by two identical populations with exponentially decaying synapses and no adaptation. However, the same procedure can be easily extendend to the case where adaptation effects are taken into account.

We start from the system of differential equations which defines our neural network model

$$
\begin{aligned}
\tau \dot{r}_1 &= \frac{\Delta}{\tau\pi} + 2 r_1 v_1 \\
\tau \dot{v}_1 &= v_1^2 + \eta - (\pi \tau r_1)^2 + J_{self} s_1 + J_{cross} s_2 \\
\tau_d \dot{s}_1 &= -s_1 + r_1 \\
\tau \dot{r}_2 &= \frac{\Delta}{\tau\pi} + 2 r_2 v_2 \\
\tau \dot{v}_2 &= v_2^2 + \eta - (\pi \tau r_2)^2 + J_{self} s_2 + J_{cross} s_1 \\
\tau_d \dot{s}_2 &= -s_2 + r_2
\end{aligned}
\tag{B.1.0.1}
$$

Being the two populations identical, these equations possess permutational symmetry: this means they are invariant under the change of the variables $(r_2, v_2, s_2, r_1, v_1, s_1) \longrightarrow (r_1, v_1, s_1, r_2, v_2, s_2)$. This symmetry admits the existence of entirely symmetric solutions $(r_1, v_1, s_1) = (r_2, v_2, s_2)$ In order to analyze the stability of such solutions, we introduce new variables

$$\begin{aligned} R_t &= (r_2 - r_1), \\ V_t &= (v_2 - v_1), \\ S_t &= (s_2 - s_1) \end{aligned} \tag{B.1.0.2}$$

$$\begin{aligned} R_l &= (r_0 + r_1), \\ V_l &= (v_0 + v_1), \\ S_l &= (s_0 + s_1) \end{aligned} \tag{B.1.0.3}$$

We refer to (R_t, V_t, S_t) and (R_l, V_l, S_l) as the transverse and longitudinal coordinates, respectively. In these new coordinates, the trajectories of the symmetric solutions are placed in the invariant subspace (0, 0, 0, R_l, V_l, S_l), with the variables satistfying the following differential equations

$$\begin{aligned} \tau \dot{R}_l &= 2\frac{\Delta}{\tau\pi} + 2R_l V_l \\ \tau \dot{V}_l &= V_1^2 + V_2^2 + 2\eta - (\tau\pi r_1)^2 - (\tau\pi r_2)^2 + (J_{self} + J_{cross})S_l \\ \tau_d \dot{S}_l &= S_l - R_l \end{aligned} \tag{B.1.0.4}$$

These equations are identical to those that descrive the dynamics of a single population of QIF neurons with a modified self-coupling strength $J = J_{cross} + J_{self}$. The solution of this kind of system has been analytically explored in Chapter 3, where we have shown that a system like the one described in Eq. (B.1.0.4) has two different types of asymptotically stable solutions: fixed point and limit cycles. These stable solutions constitute longitudinally stable solutions of our system Eq. (B.1.0.1) in the invariant subspace (0, 0, 0, R_l, V_l, S_l). In other words, this means that when the longitudinal symmetry is broken, then fixed points are no longer stable for the system with two identical populations.

The transverse stability of the symmetric solutions is defined by the variational equations of the (R_t, V_t, S_t) variables. We now suppose a complete synchronization $r_1 = r_2 = r$, $v_1 = v_2 = v$, $s_1 = s_2 = s$.

$$\begin{pmatrix} \delta\dot{R}_t \\ \delta\dot{V}_t \\ \delta\dot{S}_t \end{pmatrix} = \mathbf{A} \begin{pmatrix} \delta R_t \\ \delta V_t \\ \delta S_t \end{pmatrix} \tag{B.1.0.5}$$

with the matrix

$$\mathbf{A} = \begin{pmatrix} \frac{2}{\tau}v & \frac{2}{\tau}r & 0 \\ -2\tau\pi^2 r & \frac{2}{\tau}v & J_{self} - J_{cross} \\ +\frac{1}{\tau_d} & 0 & -\frac{1}{\tau_d} \end{pmatrix} \tag{B.1.0.6}$$

The eigenvalues of this matrix have an important meaning, because when the real part of at least one of the eigenvalues cross the imaginary axis (thus becoming positive), the transverse symmetry is broken. As a consequence, the time evolution of the two populations is different. This gives raise to the various types of asymmetric behaviours that we have seen in Chapter 4 and Chapter 5, where we have used this criterion to define the Transverse symmetry breaking curves.

In order to explicitly compute the eigenvalues of Eq. (B.1.0.6), we need the values of the fully synchronized fixed point coordinates r and v. We can find these by solving the system shown in Eq. (B.1.0.1), after setting the complete synchronization condition $r_1 = r_2 = r$, $v_1 = v_2 = v$, $s_1 = s_2 = s$ and the fixed point condition $\dot{r} = 0$, $\dot{v} = 0$, $\dot{s} = 0$. Doing this leaves us with the following algebric system

$$\begin{aligned} v &= -\frac{\Delta}{2\pi}\frac{1}{\tilde{r}} \\ \tilde{r}^4\pi^2 &- (J_{self} + J_{cross})\tilde{r}^3 - \eta\tilde{r}^2 - \left(\frac{\Delta}{2\pi}\right) = 0 \end{aligned} \tag{B.1.0.7}$$

where $\tilde{r} = \tau r$. Furthermore, we need to take only the real positive solution of the fourth order polynomial so that we are left with a physically valid solution.

If we include adaptation in our model, the fixed points change, even though the algebric system is quite similar:

$$\begin{aligned} v &= -\frac{\Delta}{2\pi}\frac{1}{\tilde{r}} \\ \tilde{r}^4\pi^2 &- (J_{self} + J_{cross} - \alpha)\tilde{r}^3 - \eta\tilde{r}^2 - \left(\frac{\Delta}{2\pi}\right) = 0 \end{aligned} \tag{B.1.0.8}$$

It is important to underline that this analysis follows the stability of a symmetric fixed point. Therefore, the analysis can produce inaccurate results inside the regions where the fixed point has lost its stability. We can look at Fig. 4.2.5 for a practical example. In the region where

the transverse symmetry is broken, the symmetric fixed point is unstable. Hence, a longitudinal symmetry analysis cannot be considered reliable and, in fact, it would detect longitudinal symmetry breaking regions even though we find no dynamical transition at all. Therefore, such curves were not considered during this thesis.

Lastly, we report the matrices related to longitudinal and tranverse symmetry for a system of identical inhibitory QIF neuron populations with exponentially decaying synapses, with Chapter 5 and without adaptation Chapter 4.

Longitudinal symmetry, no adaptation (Eq. (B.1.0.1)):

$$\mathbf{A} = \begin{pmatrix} \frac{2}{\tau}v & \frac{2}{\tau}r & 0 \\ -2\tau\pi^2 r & \frac{2}{\tau}v & J_{self} + J_{cross} \\ \frac{1}{\tau_d} & 0 & -\frac{1}{\tau_d} \end{pmatrix} \tag{B.1.0.9}$$

Longitudinal symmetry, with adaptation Eq. (5.1.0.1):

$$\mathbf{A} = \begin{pmatrix} \frac{2}{\tau}v & \frac{2}{\tau}r & 0 & 0 \\ -2\tau\pi^2 r & \frac{2}{\tau}v & J_{self} + J_{cross} & -\frac{1}{\tau_a} \\ \frac{1}{\tau_d} & 0 & -\frac{1}{\tau_d} & 0 \\ \frac{\alpha\tau}{\tau_a} & 0 & 0 & -\frac{1}{\tau_a} \end{pmatrix} \tag{B.1.0.10}$$

Transverse symmetry, with adaptation Eq. (5.1.0.1):

$$\mathbf{A} = \begin{pmatrix} \frac{2}{\tau}v & \frac{2}{\tau}r & 0 & 0 \\ -2\tau\pi^2 r & \frac{2}{\tau}v & J_{self} - J_{cross} & -\frac{1}{\tau_a} \\ \frac{1}{\tau_d} & 0 & -\frac{1}{\tau_d} & 0 \\ \frac{\alpha\tau}{\tau_a} & 0 & 0 & -\frac{1}{\tau_a} \end{pmatrix} \tag{B.1.0.11}$$

The eigenvalues where computed numerically, by adapting numerical codes taken from [56].

Appendix C

Numerical methods

C.1. Hilbert transform and instantaneous phase of a signal

In Section 4.3 we studied the effects of external forcing in our system made up by two identical QIF neuron populations. We did so by computing the phase locking through explicit counting of the maxima in the time traces of the firing rate. We now illustrate another method for computing the phase locking between two different signals, which makes use of the Hilbert transform.

In general, The Hilbert transform $\mathcal{H}[f(t)] = \tilde{f}(t)$ is a tool to determine the amplitude and instantaneous phase of a given signal $f(t)$.

We define the *analytic signal* as

$$f_a(t) = f(t) + j\tilde{f}(t). \tag{C.1.0.1}$$

From this quantity we can derive the amplitude A and the instantaneous phase $\phi(t)$ as:

$$\begin{aligned} A &= \sqrt{[f(t)]^2 + [\tilde{f}(t)]^2}, \\ \phi(t) &= \arctan \frac{\tilde{f}(t)}{f(t)}. \end{aligned} \tag{C.1.0.2}$$

From a mathematical point of view, the Hilbert transform of a signal is given by the following integral operation

$$\mathcal{H}[f(t)] = \tilde{f}(t) = f(t) * h_H(t) = \frac{1}{\pi} P.V. \int_{-\infty}^{+\infty} \frac{f(\tau)}{t-\tau} d\tau, \qquad \tau \in (-1, +1), \tag{C.1.0.3}$$

where $(*)$ is the convolution operation Therefore the Hilbert transform is a linear operator which is given by the convolution with the function $h_H(t) = \frac{1}{\pi t}$, known as the Cauchy Kernel. Since $\frac{1}{t}$ is not integrable across $t = 0$, the integral defining the convolution does not always converge. Instead, the Hilbert transform is defined using the Cauchy principal value (denoted here by P.V.).

We can use the analytical signals derived from two different real signals to evaluate if there is some kind of phase-locking between the two signals. In our particular case, we can compute the Hilbert transform of the time traces of the firing rate of both populations for a given set of system parameters, thus obtaining $f_{a,1}(t)$ and $f_{a,2}(t)$. The evolution of the phase in time is then derived as $\phi^{(l)}(t) = \arg f_{a,l},\ l \in (1, 2)$. On average, the phase will increase by 1 (or 2π if we express it in radians) for every oscillation of the system (i.e. for every synchronous activity of the network). Therefore we can define a generalized phase difference of the $n : m$ phase locked mode as:

$$\Delta\phi_{nm}(t) = n\phi^{(1)}(t) - m\phi^{(2)}(t), \tag{C.1.0.4}$$

and the degree of synchronization in the phase locked regime can be quantified in terms of the Kuramoto order parameter for the phase difference, given by:

$$\rho = |\langle \exp j\Delta\phi_{nm}(t)\rangle| \tag{C.1.0.5}$$

where $|\cdot|$ represents the magnitude and $\langle\cdot\rangle$ the time average. If the two populations are actually phase locked with a $n : m$ ratio, then this parameter will get close to one [11].

This procedure is quite reliable when we do not have a lot of harmonic components in our signal, i.e. when we do not have interaction between many different frequencies. Therefore we can conclude that the Hilbert transform technique of using the analytic signal to find the instantaneous phase requires a signal composed of a narrow band of frequencies [6], which we could obtain by filtering time traces through a specific band-pass filter. This problem is particularly evident when we have a modulated signal, which is exactly our case. For this reason this method has been explored but non specifically used for the results shown in the thesis. However, Hilbert transforms and instantaneous phase value find extensive use in statistical and computational neuroscience.

C.2. Power spectra with Fourier transform

In Chapter 5 we performed Fourier spectral analysis in order to observe the various spectral components of the time traces of our system, with specific concern with the nested oscillations

solution, where we have seen that different frequencies range interact, producing Cross-Frequecy Coupling (CFC).

In this section we will explain in further details the spectral analysis and the procedure we followed to compute the spectra.

In general, the power spectrum $S[f](\omega)$ of a time series $f(t)$ describes the distribution of power into frequency components composing that signal. According to Fourier analysis, any physical signal can be decomposed into a number of discrete frequencies, or a spectrum of frequencies over a continuous range. The statistical average of a certain signal (including noise) as analyzed in terms of its frequency content, is called its spectrum.

We suppose that our function is sampled at N different time instants over a given period of time $T = (N-1)\Delta$, producing the N values $c_0, c_1, ..., c_N$. in our specific case, Δ is the time step of our simulation of the system evolution. Given these N values of the time trace we can use the Fast Fourier Transform (FFT) to compute the discrete Fourier Transform

$$C_k = \sum_{j=0}^{N-1} c_j \exp 2\pi i j k/N \qquad k = 0, ..., N-1 \tag{C.2.0.1}$$

where i is the imaginary unit. Then, the estimate of the power spectrum is defined at $N/2+1$ frequencies as

$$\begin{aligned} &S(0) = S(f_0) = |C_0|^2 \\ &S(f_k) = \left[|C_k|^2 + |C_{N-k}|^2\right] \qquad k = 1, 2, ..., (\frac{N}{2} - 1) \\ &S(f_c) = S(f_{N/2}) = |C_{N/2}|^2 \end{aligned} \tag{C.2.0.2}$$

Since we are not interested in explicit integration of our spectra, we do not need to focus on finding an adequate normalization constant, which would be a non-trivial problem.

According to the convention we are using, f_k is defined only for the zero and positive frequencies

$$f_k = \frac{k}{N\Delta} = 2 f_c \frac{k}{N} \qquad k = 0, 1, ..., \frac{N}{2} \tag{C.2.0.3}$$

f_c is known as the Nyquist frequency.

The Nyquist Frequency f_c is an important parameter of the sampling process, during which we convert a continuous function or a signal into a discrete sequence. In units of cycles per second (Hz), its value is one-half of the sampling rate (samples per second), thus $f_c = \frac{1}{2\Delta}$. When the highest frequency (bandwidth) of a signal is less than the Nyquist frequency of the sampler, the resulting discrete-time sequence is said to be free of the distortion known as aliasing, and the

corresponding sample-rate is said to be above the Nyquist rate for that particular signal[12]. In practice, when we use a finite data length, our selected frequency bins have also a finite length ($[0,\ f_c/2]$) which is the same for every bin. As a result, practically due to this finite nature of the frequency bins, the original frequency present in the signal might fall within two adjacent bins. This leads to biased estimate of the frequency, and might also result in biased amplitude estimate. Since we make use of the FFTW3 library to compute spectra [27], the size of the time traces representing the time evolution of our system affects the sampling frequency. Specifically, extremely long data sets would bring to a low sampling frequency, which can cause inaccuracies and biases in the power spectrum due to the reduced bin size. Therefore, instead of producing a single spectrum from a long time trace, we compute a high number ($\sim$500) of spectra. Afterwards, we evaluate the average of these spectra by taking their sum for each frequency bin and dividing by their total number, thus arriving at the final results shown in Chapter 5

Bibliography

[1] Mehdi Adibi. "Whisker-mediated touch system in rodents: from neuron to behavior". In: *Frontiers in systems neuroscience* 13 (2019), p. 40.

[2] Juhan Aru et al. "Untangling cross-frequency coupling in neuroscience". In: *Current opinion in neurobiology* 31 (2015), pp. 51–61.

[3] Jan Benda and Andreas VM Herz. "A universal model for spike-frequency adaptation". In: *Neural computation* 15.11 (2003), pp. 2523–2564.

[4] Rune W Berg and David Kleinfeld. "Rhythmic whisking by rat: retraction as well as protraction of the vibrissae is under active muscular control". In: *Journal of neurophysiology* 89.1 (2003), pp. 104–117.

[5] Pierre Bergé, Yves Pomeau, and Christian Vidal. "Order within chaos". In: (1987).

[6] Boualem Boashash. "Estimating and interpreting the instantaneous frequency of a signal. I. Fundamentals". In: *Proceedings of the IEEE* 80.4 (1992), pp. 520–538.

[7] György Buzsáki. "Neural syntax: cell assemblies, synapsembles, and readers". In: *Neuron* 68.3 (2010), pp. 362–385.

[8] Santiago Ramóny Cajal. *Histologie du système nerveux del'homme des vertébrés., volumev.1. Paris:Maloine,.* URL: http://www.bio%20diversitylibrary.org/bibliography/48637.

[9] Ryan T Canolty and Robert T Knight. "The functional role of cross-frequency coupling". In: *Trends in cognitive sciences* 14.11 (2010), pp. 506–515.

[10] Ryan T Canolty et al. "High gamma power is phase-locked to theta oscillations in human neocortex". In: *science* 313.5793 (2006), pp. 1626–1628.

[11] Andrea Ceni et al. "Cross frequency coupling in next generation inhibitory neural mass models". In: *Chaos: An Interdisciplinary Journal of Nonlinear Science* 30.5 (2020), p. 053121.

[12] Maurice Charbit. *Digital signal and image processing using MATLAB*. Vol. 666. John Wiley & Sons, 2010.

[13] Namki Choi, Hwanhee Cho, and Byongjun Lee. "Development of Floquet multiplier estimator to determine nonlinear oscillatory behavior in power system data measurement". In: *Energies* 12.10 (2019), p. 1824.

[14] Stephen Coombes. "Neural fields". In: *Scholarpedia* 1.6 (2006), p. 1373.

[15] SG Cull-Candy, R Miledi, and I Parker. "Single glutamate-activated channels recorded from locust muscle fibres with perfused patch-clamp electrodes". In: *The Journal of physiology* 321.1 (1981), pp. 195–210.

[16] Gustavo Deco et al. "The dynamic brain: from spiking neurons to neural masses and cortical fields". In: *PLoS computational biology* 4.8 (2008), e1000092.

[17] Martin Deschênes et al. "Inhibition, not excitation, drives rhythmic whisking". In: *Neuron* 90.2 (2016), pp. 374–387.

[18] Annick Dhooge, Willy Govaerts, and Yu A Kuznetsov. "MATCONT: a MATLAB package for numerical bifurcation analysis of ODEs". In: *ACM Transactions on Mathematical Software (TOMS)* 29.2 (2003), pp. 141–164.

[19] Mathew E Diamond et al. "'Where'and'what'in the whisker sensorimotor system". In: *Nature Reviews Neuroscience* 9.8 (2008), pp. 601–612.

[20] Mario Dipoppa and Boris S Gutkin. "Flexible frequency control of cortical oscillations enables computations required for working memory". In: *Proceedings of the National Academy of Sciences* 110.31 (2013), pp. 12828–12833.

[21] Josef Dörfl. "The musculature of the mystacial vibrissae of the white mouse." In: *Journal of anatomy* 135.Pt 1 (1982), p. 147.

[22] Bard Ermentrout. "Ermentrout-Kopell canonical model". In: *Scholarpedia* 3.3 (2008), p. 1398.

[23] G Bard Ermentrout and Nancy Kopell. "Parabolic bursting in an excitable system coupled with a slow oscillation". In: *SIAM Journal on Applied Mathematics* 46.2 (1986), pp. 233–253.

[24] James Doyne Farmer Jr. "Order Within Chaos." In: *Ph. D. Thesis* (1981).

[25] Julia Fernández-Montoya, Carlos Avendaño, and Pilar Negredo. "The glutamatergic system in primary somatosensory neurons and its involvement in sensory input-dependent plasticity". In: *International journal of molecular sciences* 19.1 (2018), p. 69.

[26] Gordon Fraser. *The New Physics: For the Twenty-First Century*. Cambridge University Press, 2006.

[27] Matteo Frigo and Steven G Johnson. "The design and implementation of FFTW3". In: *Proceedings of the IEEE* 93.2 (2005), pp. 216–231.

[28] Richard Gast, Helmut Schmidt, and Thomas R Knösche. "A mean-field description of bursting dynamics in spiking neural networks with short-term adaptation". In: *Neural Computation* 32.9 (2020), pp. 1615–1634.

[29] Wulfram Gerstner and Werner M Kistler. *Spiking neuron models: Single neurons, populations, plasticity*. Cambridge university press, 2002.

[30] Wulfram Gerstner and Werner M kistler. *Spiking neuron models: Single neurons, populations, plasticity*. Cambridge university press, 2002.

[31] D. Golomb. *theory and modeling of whisking rhythm generation in the brainstem*. Youtube. 2020. URL: https://www.youtube.com/watch?v=9o5JuWQJciI.

[32] Boris Gutkin and Fleur Zeldenrust. *Spike frequency adaptation*. URL: http://www.scholarpedia.org/article/Spike_frequency_adaptation.

[33] A L Hodgkin. "Chance and design in electrophysiology: and informal account of certain experiments on nerve carried out between 1934 and 1952." In: *The journal of Physiology* 263.1 (1976), pp. 1–21.

[34] Alan L Hodgkin and Andrew F Huxley. "A quantitative description of membrane current and its application to conduction and excitation in nerve". In: *The Journal of physiology* 117.4 (1952), pp. 500–544.

[35] Ole Jensen and Laura L Colgin. "Cross-frequency coupling between neuronal oscillations". In: *Trends in cognitive sciences* 11.7 (2007), pp. 267–269.

[36] and Robert A Martin. John G Nicholls Bruce G Wallace. *Dai neuroni al cervello*. Zanichelli, 1997.

[37] Daniel Johnston and Samuel Miao-Sin Wu. *Foundations of cellular neurophysiology*. MIT press, 1994.

[38] Eric R Kandel et al. *Principles of neural science*. Vol. 4. McGraw-hill New York, 2000.

[39] Christof Koch. *Biophysics of computation: information processing in single neurons*. Oxford university press, 2004.

[40] Martin Krupa, Stan Gielen, and Boris Gutkin. “Adaptation and shunting inhibition leads to pyramidal/interneuron gamma with sparse firing of pyramidal cells”. In: *Journal of computational neuroscience* 37.2 (2014), pp. 357–376.

[41] Yuri A Kuznetsov. *Elements of applied bifurcation theory*. Vol. 112. Springer Science & Business Media, 2013.

[42] Carlo R Laing. “Derivation of a neural field model from a network of theta neurons”. In: *Physical Review E* 90.1 (2014), p. 010901.

[43] Wolfgang Maass. “Networks of spiking neurons: the third generation of neural network models”. In: *Neural networks* 10.9 (1997), pp. 1659–1671.

[44] Paul C Matthews, Renato E Mirollo, and Steven H Strogatz. “Dynamics of a large system of coupled nonlinear oscillators”. In: *Physica D: Nonlinear Phenomena* 52.2-3 (1991), pp. 293–331.

[45] Jeff Moehlis. *Dynamical Systems in Neuroscience: The geometry of excitability and bursting*. 2008.

[46] Ernest Montbrió, Diego Pazó, and Alex Roxin. “Macroscopic description for networks of spiking neurons”. In: *Physical Review X* 5.2 (2015), p. 021028.

[47] Jeffrey D Moore et al. “Hierarchy of orofacial rhythms revealed through whisking and breathing”. In: *Nature* 497.7448 (2013), pp. 205–210.

[48] J Munoz-Ortiz et al. “The pre-Bötzinger complex: Generation and modulation of respiratory rhythm”. In: *Neurologıa (English Edition)* 34.7 (2019), pp. 461–468.

[49] Naoko Nakagawa and Yoshiki Kuramoto. “From collective oscillations to collective chaos in a globally coupled oscillator system”. In: *Physica D: Nonlinear Phenomena* 75.1-3 (1994), pp. 74–80.

[50] Mark Ed Newman, Albert-László Ed Barabási, and Duncan J Watts. *The structure and dynamics of networks*. Princeton university press, 2006.

[51] John G Nicholls, A Robert Martin, and Bruce G Wallace. *Dai neuroni al cervello*. Zanichelli, 1997.

[52] Simona Olmi, Antonio Politi, and Alessandro Torcini. “Collective chaos in pulse-coupled neural networks”. In: *EPL (Europhysics Letters)* 92.6 (2011), p. 60007.

[53] Simona Olmi et al. “Collective oscillations in disordered neural networks”. In: *Physical Review E* 81.4 (2010), p. 046119.

[54] Edward Ott and Thomas M Antonsen. "Low dimensional behavior of large systems of globally coupled oscillators". In: *Chaos: An Interdisciplinary Journal of Nonlinear Science* 18.3 (2008), p. 037113.

[55] Diego Pazó and Ernest Montbrió. "Low-dimensional dynamics of populations of pulse-coupled oscillators". In: *Physical Review X* 4.1 (2014), p. 011009.

[56] William H Press et al. *Numerical recipes in C*. 1988.

[57] Sachin Ranade, Balázs Hangya, and Adam Kepecs. "Multiple modes of phase locking between sniffing and whisking during active exploration". In: *Journal of Neuroscience* 33.19 (2013), pp. 8250–8256.

[58] Irmantas Ratas and Kestutis Pyragas. "Symmetry breaking in two interacting populations of quadratic integrate-and-fire neurons". In: *Physical Review E* 96.4 (2017), p. 042212.

[59] John Rinzel and G Bard Ermentrout. "Analysis of neural excitability and oscillations". In: *Methods in neuronal modeling* 2 (1998), pp. 251–292.

[60] Marco Segneri et al. "Theta-nested gamma oscillations in next generation neural mass models". In: *Frontiers in computational neuroscience* 14 (2020), p. 47.

[61] Rüdiger Seydel. *Practical bifurcation and stability analysis*. Vol. 5. Springer Science & Business Media, 2009.

[62] DK Smetters and SB Nelson. "Electrotonic structure and synaptic variability in cortical neurons". In: *The Neurobiology of Computation*. Springer, 1995, pp. 135–140.

[63] Paul So, Tanushree B Luke, and Ernest Barreto. "Networks of theta neurons with time-varying excitability: Macroscopic chaos, multistability, and final-state uncertainty". In: *Physica D: Nonlinear Phenomena* 267 (2014), pp. 16–26.

[64] Jorge Sotomayor, Luis Fernando Mello, and Denis de Carvalho Braga. "Lyapunov coefficients for degenerate Hopf bifurcations". In: *arXiv preprint arXiv:0709.3949* (2007).

[65] Larry Squire et al. *Fundamental neuroscience*. Academic press, 2012.

[66] Steven H Strogatz. "Exploring complex networks". In: *nature* 410.6825 (2001), pp. 268–276.

[67] Halgurd Taher, Alessandro Torcini, and Simona Olmi. "Exact neural mass model for synaptic-based working memory". In: *PLoS Computational Biology* 16.12 (2020), e1008533.

[68] PA Valdes et al. “Nonlinear EEG analysis based on a neural mass model”. In: *Biological cybernetics* 81.5 (1999), pp. 415–424.

[69] Bradley Voytek et al. “Shifts in gamma phase–amplitude coupling frequency from theta to alpha over posterior cortex during visual tasks”. In: *Frontiers in human neuroscience* 4 (2010), p. 191.

[70] WI Welker. “Analysis of sniffing of the albino rat 1”. In: *Behaviour* 22.3-4 (1964), pp. 223–244.

[71] John A White et al. “Networks of interneurons with fast and slow γ-aminobutyric acid type A (GABAA) kinetics provide substrate for mixed gamma-theta rhythm”. In: *Proceedings of the National Academy of Sciences* 97.14 (2000), pp. 8128–8133.

[72] Hugh R Wilson and Jack D Cowan. “A mathematical theory of the functional dynamics of cortical and thalamic nervous tissue”. In: *Kybernetik* 13.2 (1973), pp. 55–80.

[73] Hugh R Wilson and Jack D Cowan. “Excitatory and inhibitory interactions in localized populations of model neurons”. In: *Biophysical journal* 12.1 (1972), pp. 1–24.

[74] Gang Zheng and Arnaud Tonnelier. “Chaotic solutions in the quadratic integrate-and-fire neuron with adaptation”. In: *Cognitive neurodynamics* 3.3 (2009), pp. 197–204.